

**Propagation of Ultrashort Optical Pulses in Nonlinear Media and
Their Applications**

by

Xiang-Dong Cao

Submitted in Partial Fulfillment
of the
Requirements for the Degree
Doctor of Philosophy

Supervised by
Professor David D. Meyerhofer
and
Professor Colin J. McKinstrie

Department of Mechanical Engineering
The College
School of Engineering and Applied Sciences

University of Rochester
Rochester, New York

1994

Curriculum Vitae

The author was born in Huangshi City, Hubei Province, China on December 30, 1962. He attended Huazhong University of Science and Technology from 1980 to 1984, and graduated with a Bachelor of Science degree in solid state electronics in 1984. He attended the Graduate School of the Academy of Science, China from 1984 to 1987, and received a Master of Science degree in space physics. He came to the University of Rochester in the Fall of 1989 and began graduate study in the Department of Mechanical Engineering. He pursued his research in the nonlinear propagation of short optical pulses under the direction of Professor David D. Meyerhofer and Professor Colin J. McKinstrie.

List of Publications

"A novel method for the measurement of temporal walk-off in nonlinear crystal", X. D. Cao, L. Zheng, and D. D. Meyerhofer. to be published in Opt. Lett.

"Frequency-domain interferometer for measurements of polarization mode dispersion in single mode fibers", X. D. Cao and D. D. Meyerhofer. Opt. Lett., **19**, 1837 (1994).

"All-optical switching via collisions of spatial vector solitons", X. D. Cao and D. D. Meyerhofer. Opt. Lett., **19**, 1711(1994).

"Optimization of optical beam steering in nonlinear Kerr media via spatial phase modulation", X. D. Cao, D. D. Meyerhofer, and G. P. Agrawal. J. Opt. Soc. Am. **B11**, 2224 (1994).

"Self-focusing of chirped optical pulses in nonlinear dispersive media," X. D. Cao, G. P. Agrawal and C. J. McKinstrie, Phy. Rev. A **49**, 1085(1994).

"Nonlinear birefringence of optical fibers," X. D. Cao and D. D. Meyerhofer, Opt. Commun. **109**, 151 (1994).

"Soliton collisions in optical birefringent fibers," X. D. Cao and D. D. Meyerhofer, J. Opt. Soc. Am. **B10**, 380 (1994).

"Solitary-wave instability in birefringent optical fibers," X. D. Cao and C. J. McKinstrie, *J. Opt. Soc. Am.* **B10**, 1202 (1993).

"The nonlinear detuning of four-wave interactions," C. J. McKinstrie, X. D. Cao, and J. S. Li, *J. Opt. Soc. Am.* **B10**, 1856 (1993).

"The nonlinear detuning of three-wave interactions," C. J. McKinstrie and X. D. Cao, *J. Opt. Soc. Am.* **B10**, 898 (1993).

"Spatial-temporal instabilities in dispersive nonlinear media," L. W. Liou, X. D. Cao, C. J. McKinstrie, and G. P. Agrawal, *Phy. Rev.* **A46**, 4202 (1992).

Conference Presentations

"Optimization of optical beam steering in nonlinear Kerr media via spatial phase modulations," X. D. Cao, G. P. Agrawal, and D. D. Meyerhofer, CLEO/QELS, Anaheim, CA, May 8-13, 1994.

"Minimizing the phase mismatch for laser harmonic generation in an ionizing gas," D. D. Meyerhofer, J. P. Peatross, and X. D. Cao, 6TH INTERNATIONAL CONFERENCE ON MULTIPHOTON PROCESSES(ICOMP VI), Quebec City, Canada, June 26-30, 1993.

"Nonlinear birefringence of optical fibers," X. D. Cao and D. D. Meyerhofer, CLEO/QELS, Baltimore, Maryland, May 2-7, 1993.

"Efficient K_a emission in high-contrast, short-pulse laser-plasma interactions," B. Soom, X. D. Cao, H. Chen, S. Uchida, B. Yaakobi, and D. D. Meyerhofer, SPIE's International Symposia on Optoelectronic Packaging and interconnects, Los Angeles, CA, Jan. 16-23, 1992.

"Nonlinear detuning of multiwave interactions," C. J. McKinstrie, X. D. Cao, and J. Li, 22nd Annual Anomalous Absorption Conference, Lake Placid, New York, July 12-17, 1992.

"Spatial-temporal instabilities in dispersive nonlinear media," L. W. Liou, X. D. Cao, C. J. McKinstrie, and G. P. Agrawal, International Quantum-Electronics Conference, Viena, June 11-14, 1992.

"Novel aspects of the nonlinear focusing of light waves," X. D. Cao, C. J. McKinstrie, and D. A. Russell, 33rd Annual Meeting of the American Physical Society Division of Plasma Physics, Tampa, Florida, November 4-8, 1991.

"The optimization of sum-frequency generation," X. D. Cao and C. J. McKinstrie, 21st Annual Anomalous Absorption Conference, Banff, Alberta, April 14-19, 1991.

Acknowledgments

I would like to thank my parents and grandparents for their unconditional support of my pursuit of a scientific career. Especially, this thesis is for the memory of my grandpa, who was so proud of his grandson.

It is a pleasure to acknowledge my advisor David D. Meyerhofer for his remarkable instructions of how to perform experiments. His mastery of scientific questioning has played an important role in maintaining the quality of my research. Also his encouragement and criticism have been very helpful in my growth as a scientific researcher. I would also like to thank my advisor Colin J. McKinstrie, who introduced me to the wonderful field of nonlinear dispersive waves. His remarkable supervision in the beginning of my graduate studies has been very helpful through the years after. I would like to thank both of them for spending so much time reading this thesis and making corrections. It is also a pleasure to thank Professor Govind P. Agrawal for teaching me nonlinear fiber optics.

I would also like to thank all members of our group. I would like to thank Dr. J. Peatross for teaching me how to align the gas target, J. L. Chaloupka for his help in preparing and installing the gas target, Yoram Fisher for setting up the CCD camera, L. Zheng for setting up the frequency doubling crystals, and Marc Adams, Christopher Moore and Brian Buerke for useful discussions. I would like to thank Dr. D. A. Russell for his help about numerical methods.

This work was supported by the U. S. Department of Energy Office of Inertial Confinement Fusion under Cooperative Agreement No. DE-FC03-92SF19460, the University of Rochester, and the New York State Energy Research and Development

Authority. The support of DOE does not constitute an endorsement by DOE of the views expressed in this work.

Abstract

In this thesis, nonlinear birefringence in optical fibers has been investigated both experimentally and theoretically. Good agreement has been found between experiment and theory. Its applications in ultrafast optical pulse shaping has been discussed. A more efficient scheme of pulse shaping based on nonlinear birefringence has been proposed and analyzed. It was found that the ellipticity of incident beam can be used to optimize the efficiency of nonlinear transmission.

Soliton stability and soliton collisions in birefringent optical fibers were investigated analytically and numerically. A virial theorem for the dynamics of vector temporal solitons was obtained. The nonlinear dependence of the soliton-fusion threshold on the birefringence was obtained for the first time, and was confirmed by computer simulation. The collisions of vector temporal and spatial solitons was studied numerically. It was found that vector soliton collisions can be classified into three different regimes: (i) soliton fusion; (ii) resonant collision; (iii) perturbative regime. The application of collisions of vector solitons in all-optical switching has also been discussed.

Finally, the self-defocusing of 1 ps laser pulses in a thin gas target was investigated experimentally. It was found that self-defocusing depends strongly on the focal geometry of the optical system (or $f^\#$). It was found that the intensity profile of laser beam was strongly modified, double foci or cone formation was observed at a pressure of 2 torr. Both the saturation of effective focal shifts and the cone formation are in agreement with theoretical predictions.

Table of Contents

Curriculum Vitae.....	ii
List of Publications.....	iii
Acknowledgments.....	vi
Abstract.....	viii
Table of Contents.....	ix
List of Figures.....	xii
List of Tables.....	xviii
Chapter 1	
Introduction.....	1
1.1 Origins of optical nonlinearity.....	1
1.2 Significance of nonlinear propagation of ultrashort pulses.....	3
1.3 Nonlinear birefringence and its applications.....	4
1.4 Soliton stability and collisions in birefringent optical fibers.....	7
1.5 Self-defocusing of short pulse in gases.....	11
1.6 Outlines.....	14
References.....	16
Chapter 2	
Frequency-domain interferometer for measurements of polarization-mode dispersion in birefringent media.....	22
2.1 Introduction.....	23
2.2 Basics of frequency-domain interferometer.....	27
2.3 Experimental results.....	32
2.4 Conclusions.....	40
References.....	42

Chapter 3	Nonlinear birefringence and its applications.....	45
3.1	The origin of nonlinear birefringence.....	46
3.2	Nonlinear birefringence in high birefringent optical fibers.....	52
3.3	Nonlinear birefringence in low birefringent optical fibers.....	57
3.4	Conclusions.....	65
	References.....	68
Chapter 4	Soliton stability and soliton collisions in birefringent optical fibers.....	70
4.1	Introduction.....	71
4.2	Stability of vector solitons in birefringent optical fibers.....	73
4.2.1	Derivation of the virial theorem.....	75
4.2.2	Solitary-wave solutions.....	80
4.2.3	Relationship between threshold amplitude and birefringence.....	82
4.3	Collision of temporal vector solitons in birefringent optical fibers.....	91
4.4	Stability and collisions of spatial vector solitons.....	105
4.4.1	Fusion threshold of spatial vector solitons.....	107
4.4.2	All-optical switching via collisions of spatial vector solitons.....	108
4.5	Conclusions.....	114
	References.....	118
Chapter 5	Self-defocusing of ultra-intense 1 ps laser pulses in low-pressure thin gas target.....	121

	5.1	Introduction.....	122
	5.2	Experimental setup.....	124
	5.3	Experimental results.....	131
	5.4	Theoretical model and computer simulations.....	135
	5.4.1	Comparison of experimental results with the thin lens approximation.....	143
	5.4.2	Comparison of experimental results with computer simulations.....	145
	5.5	Conclusions.....	151
		References.....	153
Chapter 6		Summary	155
Appendix		Numerical method.....	157
		References.....	161

List of Figures

Fig. 2.1	Temporal stretching of short pulses in a spectrometer.....	29
Fig. 2.2	The experimental setup. Where $\lambda/2$ means half-wave plate, MO microscope objectives, P polarizer, and M mirror. The linearly polarized light is coupled into the optical fiber with the polarization direction aligned to 45° with respect to fiber axes.....	30
Fig. 2.3	The spectrum of the incident pulses. The spectrum shape is typical of the combined effects of SPM and GVD. The peak-peak width is 31.6 \AA	34
Fig. 2.4	Frequency-domain interference fringes. The fringe spacing is measured to be 9.13 \AA	36
Fig. 2.5	Frequency-domain interference fringes of sample CDA I. The fringe spacing is measured to be 6.7 \AA . The solid line is the experimental data, while the dashed line is the theoretical fit.	39
Fig. 2.6	Dependence of the group-velocity walkaway on the propagation direction. The angle is measured with respect to the phase-matching angle of the sample (KDPII).....	41
Fig. 3.1	Experimental setup. $\lambda/2$ -half wave plate; MO- $\times 10$ micro-objective; $\lambda/4$ -quarter wave plate; P-polarizer.....	51

Fig. 3.2	Experimental results of nonlinear transmission for a twisted fiber. The data points are 5° apart.....	54
Fig. 3.3	Experimental results of nonlinear transmission for a loosely placed fiber. The data points are 2° apart. The transmission shows periodic modulations.....	56
Fig. 3.4	Experimental setup. x and y are the axes of the first quarter wave plate; q is the angle between x and the polarization vector; P-polarizer.....	58
Fig. 3.5	Nonlinear transmission verses incident angle of the polarization vector; Upper curve corresponds to the new scheme, while the lower one corresponds to the scheme of Stolen et al. ⁸	60
Fig. 3.6	Peak nonlinear transmission verses incident power. Upper curve corresponds to the new scheme, while the lower one corresponds to the scheme of Stolen et al. ⁸	64
Fig. 3.7	Optimal polarization ellipticity e_{opt} verses incident power measured by ϕ_{spm}	66
Fig. 4.1	The solid line shows the analytical result of Kivshar; the dashed line is the estimation of Hasegawa; the numerical result of Menyuk is given by filled circles; the band bounded by two solid curves is plotted according to Eq. (4.30) with $L = 8$, and $L = 4$, respectively, corresponding to 99.96% and 96% of the energy in a soliton pulse; the unfilled circles are our numerical simulations, $\epsilon = 2/3$	86
Fig. 4.2	The partial solitons are separated while experience nonlinear oscillations along their own paths.....	88

- Fig. 4.3 The partial solitons bounce back and forth while propagating, and form a trapped state.....89
- Fig. 4.4 Dependence of M on the linear birefringence δ . (a) The overall behavior. (b) Fine structure of the second interval, $0.27 < \delta < 0.305$90
- Fig. 4.5 Dependence of v - δ of colliding solitons on the linear birefringence δ . (a) The overall behavior. (b) Fine structure of the second interval, $0.27 < \delta < 0.305$ 94
- Fig. 4.6 Dynamic behavior of soliton collision in the second interval with $\delta = 0.298$. (a) Variation of $m(z)$ versus propagation distance Z . (b) Variation of center of mass of one soliton versus propagation distance Z95
- Fig. 4.7 Dynamic behavior of soliton collision in the second interval with $\delta = 0.304$. (a) Variation of $m(z)$ versus propagation distance Z . (b) Variation of center of mass of one soliton versus propagation distance Z98
- Fig. 4.8 There is no mixing when velocities of colliding solitons are large, $\delta = 2$ 99
- Fig. 4.9 A new kinds of soliton generated by soliton collision. $\delta = 0.304$. After 200 soliton periods, one of the outgoing solitons is used as the initial condition for the next simulation.....100
- Fig. 4.10 Cerenkov emission generated by two colliding solitons in the second interval. $\delta = 0.2$, propagation distance $Z = 200$ soliton periods. (a) The trapping state is shown in the center, while the radiation is shown outside the center part. The radiation field is

	amplified 1000 times. (b) Radiation detected at position far from the trapping region, $T = 20$	104
Fig. 4.11	Dynamic behavior of a soliton collision in the second interval with $\theta = 0.301$, $A_0 = 1$. (a) Propagation of the intensity profile of component A_1 . (b) Variation of $m(z)$ versus propagation distance Z	109
Fig. 4.12	Dynamic behavior of a soliton collision in the third interval with $\theta = 0.35$, $A_0 = 1$. (a) Propagation of the intensity profile of component A_1 . (b) Variation of $m(z)$ versus propagation distance Z . (c) Variation of center of mass of one soliton versus propagation distance Z	111
Fig. 4.13	Dynamic behavior of soliton collision in the second interval with $\theta = 0.3002$, $A_0 = 1$. Each soliton is totally reflected by the other because of the nonlinear refraction.....	114
Fig. 5.1	A top-view schematic of the vacuum chamber. The distance from the lens to the focus is approximately 1.5 m. ⁸	124
Fig. 5.2	Schematic of the chirped-pulse-amplification laser system. ⁸	125
Fig. 5.3	A schematic setup of 9mm amplifier system. ⁸	127
Fig. 5.4	A schematic experimental setup for measuring the self-defocusing effect.....	128
Fig. 5.5	Focal shifts at different pressure due to the effect of self-defocusing. The vertical axis represents the radius of the beam, while the horizontal axis is the relative position along the beam propagating direction. The solid curve corresponds to the case of $p = 0$ torr, the dashed curve represents $p = 2$ torr, and the dashed and dot curve corresponds to $p = 5$ torr.	130

- Fig. 5.6 The intensity distribution of $p = 0$ and 5 torr at normalized distance $z = 1.2$ are shown. When propagating in vacuum, the laser beam remains close to a Gaussian beam, no extra structure was observed, as shown in Fig. (5.6a). When $p = 5$ torr, as shown in Fig. (5.6b), the cone formation is evident.....134
- Fig. 5. 7 Focal shifts at different pressure due to the effect of self-defocusing. The vertical axis represents the radius of the beam, while the horizontal axis is the relative position along the beam propagating direction. The solid curve corresponds to the case of $p = 0$ torr, the dashed curve represents $p = 2$ torr, and the dashed and dot curve corresponds to $p = 5$ torr. $f^\# = 25$136
- Fig. 5.8 Fig. (5.8a) shows intensity distribution during the propagation assuming a Gaussian distribution in the electron density. Fig. (5.8b) shows the same intensity distribution, but with a super-Gaussian electron density profile. Fig. (5.8a) shows a smooth variation with a single peak distribution, while Fig. (5.8b) clearly shows that there are two peaks corresponding to a ring structure in 2D.....144
- Fig. 5.9 Shows the variation of $1/I(0,0)$ during the propagation in the image space, assuming that the electron density profile is a super-Gaussian. At $p = 0$, there is no effect of self-defocusing, the corresponding curve shows a smooth variation. At $p = 2, 5$ torr, we can see strong self-defocusing, as well as the existence of two foci, very similar to Fig. (5.5).....146
- Fig. 5.10 Computer simulation results of intensity distribution at $z = 0.8$.
 (a) $p = 0$ torr; (b) $p = 5$ torr.148

- Fig. 5.11 3D plot of intensity distributions at different pressures. (a) $p = 5$ torr. (b) $p = 0$ torr.150
- Fig. 5.12 $f^\#$ -dependence of effective focal shifts. The vertical axis is the peak intensity, the horizontal axis is the relative distance from the geometric focal point when $p = 0$ torr.152

List of Tables

Table 2.1	Waveguide parameters of the fiber used in the experiment.....	35
Table 2.2	Parameters of nonlinear crystals and measured walk-off.....	37

CHAPTER 1

Introduction

1.1 Origins of optical nonlinearities

Traditionally, the response of an optical medium to applied laser radiation becomes nonlinear when the polarization density of the medium depends nonlinearly on the laser field. According to Maxwell's equations, this nonlinear polarization will be a source of new radiation. It is well known in nonlinear optics that the nonlinear polarizability is responsible for many important phenomena such as harmonic generation, frequency mixing, stimulated Raman scattering (SRS), stimulated Brillouin scattering (SBS), phase conjugation, and nonlinear refraction.¹⁻⁷ The origins of this nonlinear polarization can be microscopic, or macroscopic, depending on whether the nonlinear response is from electronic excitation within an atom or a molecule, or from acoustic excitations of the bulk medium. Sometimes, the temperature of the medium rises due to linear and nonlinear absorption, which modifies its optical properties and thus causes a nonlinear response. Since different excitations have different response times, the corresponding nonlinearities also have different response times. For example, electronic polarization is almost instantaneous, molecular orientation has a response time of picoseconds, electrostriction has a response time of nanoseconds, saturated atomic absorption has a time scale of 10 nanoseconds, while thermal effects have response times of milliseconds.⁷

Among the variety of nonlinear mechanisms, only electronic polarization is nearly instantaneous. This ultrafast nonlinearity has found more and more applications in fields such as self mode-locked lasers, or the Kerr-lens mode locking

(KLM) laser, ^{8,9} optical switching and optical computing.¹⁰ The purpose of this thesis is to investigate the nonlinear propagation of ultrashort pulses and their applications. We are particularly interested in nonlinearities resulting from the instantaneous electronic response. All other kinds of nonlinear contributions will be ignored due to their finite response time. The mechanisms of nonlinear electronic polarizations can be further classified into two subgroups depending on whether the nonlinearity comes from (a) the anharmonic motion of bound electrons under the influence of an applied field or (b) the field-generated free electrons or free-carriers. It should be pointed out that the second kind of nonlinearity does not come from the free electrons themselves, since the response of free electrons will become nonlinear only when the laser intensity is relativistically high ($> 10^{18}$ W/cm²).¹¹ The nonlinearity comes from the fact that the ionization changes the free electron density in the medium, and thus changes the refractive index. When the free-carrier or electron densities are changed by optical excitations, we are concerned with real transitions. The resulting nonlinear processes proceed via a real exchange of energy from the optical field to the medium, and are often referred as 'dynamic nonlinearities' in the field of semiconductors.^{12,13} This kind of nonlinear response occurs in semiconductors when free electrons or carriers are generated by an applied field, or in gases and bulk media when ionization occurs. For bound electrons, the nonlinearity comes from the virtual transitions between the ground state and other virtual states when the laser wavelength is far away from any resonance.⁷ From the Heisenberg uncertainty principle, we know the response time is inversely proportional to the energy difference between the ground state and the excited states, which corresponds to a time scale around 10^{-16} seconds, almost instantaneous. The tunneling rate for hydrogen is approximately 10^{14} s⁻¹ at an intensity of 10^{14} W/cm², which corresponds a response time of a few optical cycles for 1 μ m wavelength light. It should be

mentioned that the dynamic nonlinearity in a gas medium is much simpler than that in semiconductors, in which the collective effects of electrons, energy band structure, and Coulomb shielding effects play very important roles in modifying the nonlinear response. In this thesis, the only dynamic nonlinearity we consider is that in low-density gases. Although the nonlinearities of bound electrons and ionized free electrons all have a fast response, they have different properties. In this thesis, we study the effects of these two nonlinearities on the propagation of ultrashort pulses and their practical applications.

1.2 Significance of nonlinear propagation of ultrashort pulses

The propagation of laser radiation becomes nonlinear when the optical properties of a medium are modified due to the presence of intense light. The most important optical property that affects light propagation is the refractive index. Therefore, nonlinear propagation usually means that the refractive index becomes a function of the intensity of applied field, or mathematically, $n = n_0 + \Delta n(I)$, where n is the total refractive index, n_0 is the linear refractive index, Δn is the nonlinear refractive index. In most applications in which the nonlinear effect is relatively weak, Δn can be expanded as $\Delta n = n_2 I + n_4 I^2 + \dots$, where $n_2 I \gg n_4 I^2$.

It is very important to study the nonlinear propagation of ultrashort pulses. Nonlinear refraction is universal for all nonlinear media. Nonlinear propagation has strong effects on other kinds of nonlinear interactions such as three and four-wave mixing, SRS and SBS. For instance, it can detune the three and four-wave mixing processes,^{14,15} reduce the threshold of SRS,⁵ and change the characteristics of high-order harmonic generation.¹⁶ Second, nonlinear refraction is a phase-insensitive process in the sense that it depends only upon laser intensity, it does not require any phase matching. Third, it provides an important method for controlling light with light

more rapidly than is possible with any electronic device can provide. In recent years, many applications have been found in the area of optical switching, optical computing, and optical communications.¹⁰

For most applications in which the nonlinear effect is weak, the refractive index can be truncated as $n = n_0 + n_2 I$. The values of n_2 can be either positive or negative, depending on the detailed nonlinear mechanisms. For the electronic polarizations in which we are interested in this thesis, n_2 is positive for nonlinearity coming from bound electrons, and negative for ionized free electrons. Aside from the sign of n_2 , there is another important factor which causes very different behaviors of nonlinear propagation of short pulses; dispersion. Since we are interested in pulse widths less than 10 ps, chromatic dispersion may play an important role in the propagation of short pulses. Chromatic dispersion is usually described by group velocity dispersion (GVD).¹ The combination of nonlinear refraction and GVD generates a variety of phenomena such as optical solitons, spatial-temporal self-focusing or dark solitons, or/and self-defocusing.^{1,17} The spatial analogy of GVD is diffraction, and the combination of nonlinear refraction with diffraction is responsible for spatial solitons, self-focusing, and self-defocusing. In this thesis, we study different cases depending on whether GVD or diffraction is important, or the sign of n_2 is positive or negative. Different combinations of n_2 , GVD and diffraction can generate very different spatial and temporal behaviors.

1.3 Nonlinear birefringence and its applications

In an isotropic nonlinear medium, the nonlinear refraction manifests itself in many ways. Nonlinear birefringence (or nonlinear polarizations rotation) is one of the more interesting phenomena.¹ In a birefringent medium, the polarizations state of an incident laser beam will change as it propagates if the initial polarizations state is not

one of the polarizations eigenstates of the birefringent medium. Nonlinear birefringence means that the medium becomes birefringent due to the presence of intense light, and the polarizations state will change during propagation through the medium. Nonlinear birefringence can be best understood in terms of self-phase modulation (SPM) and cross-phase modulation (XPM).¹ When there are two or more laser beams copropagating in a medium, each beam experiences some amount of nonlinear phase modulation due to the effect of nonlinear refraction. There are two contributions to the nonlinear phase modulations, one comes from the presence of the beam itself, the other is from all the other copropagating beams. The nonlinear phase-modulation due to the beam is referred as SPM, while those due to the presence of other intense beams is referred as XPM. An elliptically polarized beam can be described by two linearly and orthogonally polarized beams. In a nonlinear Kerr medium, the effect of SPM and XPM generates a phase difference between these two orthogonally polarized components, similar to the situation in which a light beam passes through a birefringent medium. The difference is that in the former case, the phase difference is intensity-dependent, and that is why it is called nonlinear birefringence. The physical reason for this phase difference comes from that fact that SPM and XPM have different strengths even if the beams have the same intensity.

Since its first discovery in 1964,¹⁸ nonlinear birefringence has been found very useful in many applications. Basically, there are two reasons that make nonlinear birefringence practical. One comes from that fact that its nonlinear response is almost instantaneous, which makes it very desirable in broadband optical devices such as optical switches with THz bandwidths.¹⁰ The other reason is related to the advanced technology of optical fibers. The small mode size and extremely low loss of optical fibers provide an ideal nonlinear medium. The small mode size makes it possible to obtain high intensity with relatively low power, while low loss makes it possible to

use longer lengths of optical fiber so that enough nonlinear phase modulation can be accumulated. Furthermore, it is difficult to separate nonlinear birefringence from self-focusing in a bulk medium, while there is no self-focusing in optical fibers. Nonlinear birefringence or self-induced birefringence in optical Kerr media has found many applications since its discovery by Maker et al.¹⁸ For example, nonlinear birefringence has been used in optical shutters and optical modulators with picosecond response times,¹⁹ pulse shaping or intensity discriminators,²⁰ optical pulse cleaners,²¹⁻²³ fiber-optic logic gates^{10,24,25} high-resolution distributed fiber sensors,²⁶ and for passive mode locking of fiber lasers.²⁷⁻³⁰

One goal of this work is to perform more detailed investigations of nonlinear birefringence, and try to find optimal conditions for using nonlinear birefringence. Since residual birefringence always exists in optical fibers, the polarizations rotation depends on both linear and nonlinear birefringence in a very complicated manner. From the point of view of practical applications, there are two very interesting cases: one is the case in which nonlinear birefringence dominates, the other is the case in which linear birefringence dominates. In the former case, Maker et al.¹⁸ found there are two nonlinear eigenstates of polarizations that will not change with propagation, the linearly and circularly polarized states. For a given incident laser intensity, the nonlinear polarizations rotation is a function of the polarizations ellipticity. Since linear and circular polarizations are eigenstates, there must exist an optimal ellipticity for which the nonlinear birefringence is the largest. In the latter case, the effect of nonlinear birefringence can be understood in the following way. If the angle between the polarizations direction of the incident laser light and the fast axis of the optical fiber is not zero, the electric fields along both fast and slow axes will not be zero. Therefore, both components induce refractive index changes not only along their own

axis but also along the other axis, that is, the refractive index change along one axis is due to both self-phase modulation and cross-phase modulation. As a consequence of this nonlinear birefringence, the polarizations of the total electric field rotates, and the electric field polarizations will in general be elliptical. If the linear birefringence is compensated for and a polarizer is used to block low intensity light that does not have a polarizations rotation, then the transmitted light will depend on the incident power and polarizations direction. Previous experiments^{31,32} only confirmed the power dependence of the transmission; discrepancies were found in the relation between transmission and input polarizations. For example, when the incident polarizations is along one of the optical axes, there is no electric field along the other axis. Thus, there should be no nonlinear birefringence and, hence, zero transmission. Previous experimental results showed that the nonlinear birefringence was not zero, and no experiment confirmed the overall behavior of transmission with respect to the polarizations direction. This discrepancy was believed to be due to the random fluctuations of the birefringent axis and the misalignment of the incident polarizations vector in the experiments. One disadvantage of previous investigations was the low switching contrast since the residual birefringence of optical fibers was not compensated, and the transmission was not optimized. In this thesis, we investigate the nonlinear transmission under a variety of conditions, and find the optimal conditions.

1.4 Soliton stability and collisions in birefringent optical fibers

In 1973, Hasegawa and Tappert realized that optical fibers exhibit both the optical Kerr effect and negative GVD at wavelengths longer than 1.3 μm .³³ Thus they predicted optical fibers could satisfy the mathematical requirements for the propagation of optical solitons, or nonlinear pulses that do not suffer from any

distortion of the pulse shape as they propagate. The broadening caused by linear dispersion associated with any short pulses is compensated for by nonlinear effects. Seven years after the prediction by Hasegawa and Tappert, Mollenauer et al.³⁴ succeeded in the generation and transmission of optical solitons in a fiber for the first time. One of the important applications of optical solitons is in high bit-rate optical transmission systems. Since solitons are not distorted by fiber dispersion, they can be transmitted for an extended distance only by providing amplification to compensate for the fiber loss. Since fibers can be converted to amplifiers by appropriate doping,³⁵ this property of a soliton can be used to construct an all-optical transmission system, which is much more economical and reliable than a conventional system that requires repeaters involving both photonics and electronics in order to reshape the optical pulse distorted by the fiber dispersion. The early experiments were carried out using Raman amplification. With the development of diode-pumped Erbium-Doped-Fiber-Amplifiers(EDFA)³⁵, a much more practical amplifier became available. All long-distance-fiber-propagation experiments are currently done with such amplifiers. Mollenauer³⁶⁻⁴⁰ demonstrated this repeaterless transmission system over distances of 12,000 km. Another important application of optical solitons is for all optical-switching. The aim of all optical-switching is to effect the travel of one optical pulse by another, the 'signal' pulse by the 'control' pulse¹⁰. Islam used the properties of soliton collisions in a birefringent fiber to build all-optical switching devices, called soliton-dragging devices.¹⁰ The advantage of using solitons instead of ordinary optical pulses comes from the unique properties of solitons. Since solitons can adjust themselves in such a way that the phase is uniform across the whole pulse, they can be switched as a whole unit, while for non-soliton pulses only high intensity part will be switched, and the pulse shape will be distorted due to the intensity-dependent transmission.

Real fibers always have some residual birefringence due to manufacturing processes such as stress, twisting, and environmental conditions such as thermal effects. It has been found that it is always possible to find two principal states of polarizations (PSP) in birefringent fibers.⁴¹ When the incident polarizations direction is aligned to one of the PSP's, there will be no change in the exit polarizations state. For short pulses, birefringence combined with GVD causes a pulse to split in the time domain because of the difference in the group velocities of polarizations components along the two birefringent axes. This group velocity difference of pulses with their polarizations aligned to different birefringent axes of a fiber is referred to as polarizations mode dispersion (PMD). Just as nonlinear refraction can negate linear birefringence to form solitons in isotropic medium, the same nonlinearity can also be used to compensate for the polarizations mode dispersion, and regain the property of soliton propagation in an optical fiber. The penalty is a higher amplitude threshold for generating stable solitons. Menyuk numerically studied soliton stability under the effect of PMD,^{42,43} and found that a soliton with sufficient energy can still be robust in the presence of substantial birefringence. It was found that when a pulse consisting of both polarizations is injected into an optical fiber, each polarizations component shifts its central frequency in such a way that the two polarizations self-trap and move down the fiber with the same average velocity. If the power or amplitude of the initial injected optical pulse is below a certain threshold, the two polarizations will not be able to trap each other, they will separate from each other after propagating some distance. However, they change each other's phase after separation. The problem of soliton stability in a birefringent fiber was later analyzed by Kivshar using a perturbation method.⁴⁴ His results showed a linear dependence of the soliton threshold amplitude on linear birefringence or PMD, which is in agreement with computer simulations when the PMD is small. Menyuk's simulation showed that this

dependence is nonlinear, and there is a significant deviation for larger PMD. In this thesis, we use a new method to study the problem of soliton stability. We are able to find an analytic result for the soliton threshold, which agrees very well with computer simulations.⁴⁵ It provides a useful criteria for practical system design.

PMD not only changes the soliton threshold, it also changes the fundamental physical properties of the system. In an isotropic medium ($\text{PMD} = 0$), solitons are described by the Nonlinear Schrodinger equation(NSE),³³ which is integrable in the sense that there is an infinite number of constants of motion. Soliton propagation in birefringent optical fibers is described by two coupled nonlinear Schrodinger equations [NSE's],^{46,47} which are known to be nonintegrable by means of the inverse-scattering method.⁴⁷ The most important difference between an integrable nonlinear wave equation and a nonintegrable one is that the collision between solitary waves is elastic in the former case and inelastic in the latter.^{46,47} There is always radiation emitted during solitary wave collisions in a nonintegrable system such as the system governed by the coupled NSE's. In this thesis, we study the details of soliton collisions in birefringent optical fibers and their applications. This subject attracts great current interest due to its scientific importance^{42,43,48,49} and its potential applications to optical logic devices.^{10,50,51} If the amplitudes of two colliding solitons with orthogonal polarizations directions are below a threshold value, the two solitons will separate from each other after the collision. Each soliton will be strongly changed after the collision with the other, although each still propagates as a soliton. The most important changes include polarizations mixing, central frequency shifts and velocity changes. In this thesis, it is found that the relative contribution to the total polarizations state varies over a large range and depends very sensitively on the linear birefringence. By linearizing the coupled nonlinear Schrodinger equations, Malomed and Wabnitz⁵² found that there exists a critical value of linear

birefringence for which the soliton collision is resonant in the sense that the spatial frequency of the soliton shadow equals that of the soliton with much larger amplitude. When the linear birefringence is above this critical value, the interaction between two solitons is small and each soliton picks up a shadow after a collision. Most of the previous work on soliton collisions was in the nonresonant regime, and the mixing effect was very small. In this thesis it is found that the resonant regime is more subtle in that it consists of bound states and unbound states. In an integrable system, solitons will not change their velocities after a collision. However, the velocities of two colliding solitons generally change after a collision in a nonintegrable system. We also investigate this aspect by numerical simulation. It is found that both the velocity change and the amount of mixing measured by means of cross-correlation depend strongly on the linear birefringence. The XPM between two colliding pulses generates nonlinear frequency shifts and, thus, velocity changes due to group velocity dispersion. The dependence of the velocity changes on the linear birefringence is similar to that of the mixing on the linear birefringence. None of the previous work on soliton collisions was concerned with the dependence on the linear birefringence. It is not surprising that only very small mixing has been found, since the linear birefringence chosen in previous work was very large, and the collisions were in the nonresonant regime. The entire range of parameter space in the magnitude of the linear birefringence is investigated in this thesis. A variety of phenomena in soliton collisions are found in this thesis and their application to all-optical switching is discussed in detail.

1.5 Self-defocusing of short pulse in gases

When n_2 is negative, an intense laser beam will experience self-defocusing when propagating in a bulk or gas medium. Like self-focusing,⁵ self-defocusing is an

intensity-induced lens effect. For a beam with a Gaussian-like transverse profile, the central part of the beam having a larger intensity experiences less refractive index than the edges due to the presence of free electrons, and therefore the center region travels at a faster velocity than the edges. Consequently, the wavefront distortion is similar to that generated by a negative lens, and the beam appears to defocus by itself.

Among many nonlinear mechanisms that give rise to negative n_2 , we are particularly interested in the dynamical nonlinearity, that is, the nonlinear refraction resulting from ionization of a gas medium or free-carrier generation in semiconductors. In this thesis, we concentrate on self-defocusing in gas media, although the physics is also valid for the other case. Since the invention of the chirped pulse amplification system (CPA),^{53,54} the availability of ultrahigh intensity lasers opened a new era for both nonlinear optics and high-field atomic physics. Currently, CPA systems are able to provide pulses with 54 TW peak power and an intensity of $10^{19} - 10^{20}$ W/cm² at focus.⁵⁵ With such high power lasers, a variety of new phenomena can be investigated experimentally. These phenomena include (i) wake-field acceleration,⁵⁶⁻⁶¹ (ii) relativistic optical guiding or self-focusing,⁶²⁻⁶⁴ (iii) laser frequency amplification,^{65,66} (iv) relativistic harmonic generation,⁶⁷ (v) nonlinear Thomson scattering,^{11,68} (vi) multiphoton ionization⁶⁹⁻⁷² (vii) above-threshold ionization,^{73,74} (viii) high-harmonic generation in gases,⁷⁵ (ix) and X-ray lasers.^{76,77} A common factor of all these applications of high-power laser systems is that almost all the media used in these experiments are gases or plasmas, since only gases or plasmas don't have the problem of material damage. A direct consequence of this fact is the self-defocusing associated with the dynamical nonlinear response. All these experiments require nonlinear propagation of laser pulses in a gas target with intensities ranging from 10^{13} W/cm² to 10^{19} W/cm². It is well-known that the laser-generated plasma decreases the refractive index, or in other words has a negative n_2 .

As a result of this laser-generated negative lens, the laser beam may begin to defocus before the beam reaches the geometric focal point in vacuum, which greatly limits the maximum intensity achievable in a gas target. The ionized gas or plasma can have a drastic effect on the propagation of the laser pulse due to self-defocusing. The effect of self-defocusing in an ionized gas is not new. In 1974, Feit and Fleck used this phenomenon to explain the dependence of the breakdown threshold of gases on focal spot size.⁷⁸ Borger and Smith found that the threshold increases as the spot size is decreased.⁷⁹ Self-defocusing causes a significant portion of the laser energy to be refracted, resulting in a reduction in absorption. As the spot size is reduced, this effect becomes more important. Recently, new interests have been stimulated by the potential applications of ultrashort intense laser pulses in underdense plasmas: both experimental investigations⁸⁰⁻⁸⁴ and computer simulations^{82,83,85,86} have been done. All these studies concern relatively high pressure, for example, > 10 torr for high-harmonic generation, > 1 bar for x-ray recombination lasers and plasma-based accelerators. It was found recently that self-defocusing could be important at a pressure as low as 3 torr with an intensity of the order of 10^{14} W/cm².¹⁶ The focal spot was three times larger than that associated with vacuum propagation. This finding shows that self-defocusing may play a more important role than previously expected. For example, the work of Auguste et al.⁸¹ and Rae⁸⁶ were performed with backfilled gas tanks at pressures larger than 15 torr. Rae found that the tighter the focus, or the smaller the $f^\#$, the larger the maximum electron density. Intuitively, more severe self-defocusing is expected for smaller $f^\#$, since the change in refractive index is proportional to N_p . However, both the effective interaction length and ionized volume will be smaller for a beam with tighter focus, which results in less accumulated phase distortion. Therefore, the self-defocusing will be less significant for smaller $f^\#$. In order to understand this, we developed a thin lens model. It is found

that the significant self-defocusing at pressure as low as a few torr can be explained by the $f^{\#}$ dependence of self-defocusing. We also found that the saturation of focal shifts can be explained by this model. On the other hand, the experimental data clearly showed the formation of a cone in the laser intensity distribution, which is beyond the thin lens approximation. However, an improved model based on the thin lens approximation can be used to explain the cone formation. Since this improved model is more complicated than the thin lens approximation, we can only obtain results by computer simulation, instead of analytic results.

1.6 Outline

Chapter 2 describes an experimental technique called frequency-domain interferometry (FDI). This technique has been used to measure polarizations mode dispersion (PMD) in optical fibers, since PMD has strong effects on soliton stability and soliton collisions in birefringent optical fibers. Detailed working principles of FDI have been given in this chapter, as well as the experimental results.

Chapter 3 is devoted to the experimental investigations of nonlinear birefringence and its application in optical pulse cleaning. Nonlinear transmission has been measured as a function of the incident polarizations angle for the first time, and good agreement between theory and experiment has been found. The possible applications of nonlinear birefringence are also discussed.

Chapter 4 describes numerical studies of the effects of PMD on the stability and collisions of temporal solitons in birefringent optical fibers. An analytic result for the soliton threshold has been obtained by using a virial theorem. This result is the only one that is consistent with computer simulation for the whole range of PMD. Collisions of vector solitons have been numerically investigated in detail. Many new

properties have been found, and their possible applications in all-optical switching have been discussed.

Chapter 5 describes the propagation of intense laser pulses in a thin gas target. After describing the experimental setup, we show several experimental results. It has been found that the self-defocusing induced by ionization can be explained by the thin lens approximation. The theoretical predictions of the thin lens approximation, such as effective focal shifts in the image plane and the saturation of the focal shifts, have been confirmed experimentally. It has been found experimentally that there are two foci in the image plane, which give rise to the formation of a cone in the transverse intensity distribution. Based on the thin lens approximation, we have developed an improved model to explain the cone formation. The physical mechanism of cone formation has been discussed.

Finally, this work is summarized in Chapter 6.

REFERENCES

1. G. P. Agrawal, *Nonlinear Fiber Optics* (Academic Press, Boston, 1989).
2. S. A. Akhmanov and R. V. Khokhlov, *Problems of Nonlinear Optics* (Gordon and Breach, New York, 1972).
3. N. Bloembergen, *Nonlinear Optics* (Benjamin, New York, 1964).
4. P. N. Butcher and D. Cotter, *The Elements of Nonlinear Optics* (Cambridge University Press, 1990).
5. Y. R. Shen, *The Principles of Nonlinear Optics*, (Wiley, New York, 1984).
6. A. Yariv, *Quantum Electronics*, 2nd Edition (Wiley, New York, 1989).
7. R. W. Boyd, *Nonlinear Optics*, (Academic Press, Boston, 1992).
8. D. E. Spence, P. N. Kean, and W. Sibbett, *Opt. Lett.* **16**, 42(1991).
9. M. T. Asaki, C.-P. Huang, D. Garvey, J. Zhou, H. C. Kapteyn, and M. M. Murnane, *Opt. Lett.* **18**, 977(1993).
10. M. N. Islam, *Ultrafast Fiber Switching Devices and Systems*, (Cambridge University Press, Cambridge 1992).
11. E. S. Sarachik and G. T. Shappert, *Phys. Rev. D***1**, 2738(1970).
12. A. Miller, D. A. B. Miller and S. D. Smith, *Adv. Phys.* **30**, 697(1981).
13. J.-L. Oudar, *Nonlinear Optics: Materials and Devices*, 91, C. Flytzanis and J.-L. Oudar eds. (Springer-Verlag, Berlin, 1985).
14. C. J. McKinstrie and X. D. Cao, *J. Opt. Soc. Am.* **B10**, 898 (1993).
15. C. J. McKinstrie, X. D. Cao, and J. S. Li, *J. Opt. Soc. Am.* **B10**, 1855 (1993).
16. J. P. Peatross, "The Far-field Angular distribution of High-order Harmonics Production in Light scattering from a Thin Low-density Gas Target", Ph. D Thesis, 1994, University of Rochester. Ch. 2.
17. *Optical Solitons*, J. R. Taylor, ed., (Cambridge University Press, 1992).

18. P. D. Maker, R. W. Terhune, and C. M. Savage, *Phys. Rev. Lett.* **12**, 507 (1964).
19. M. A. Duguay, in *Progress in Optics*, edited by E. Wolf (North-Holland, Amsterdam, 1976), Vol. 14, p.163.
20. R. H. Stolen, J. Botineau, and A. Ashkin, *Opt. Lett.* **7**, 512 (1982).
21. B. Nikolaus, D. Grischkowsky, and A. C. Balant, *Appl. Phys. Lett.* **8**, 189 (1983).
22. N. J. Halas and D. Grischkowsky, *Appl. Phys. Lett.* **48**, 823 (1986).
23. J.-L. Tapie and G. Mourou, *Opt. Lett.* **17**, 136 (1992).
24. K. Kitayama, Y. Kimura, and S. Seikai, *Appl. Phys. Lett.* **46**, 317 (1985).
25. Y. Kimura, K.-I. Kitayama, N. Shibata, and S. Seikai, *Electron. Lett.* **22**, 277 (1986).
26. W. Zhao and E. Bourkoff, *IEEE J. Quantum Electron.* **29**, 2198 (1993).
27. M. Hofer, M. E. Fermann, F. Haberl, M. N. Ober, and A. J. Schmidt, *Opt. Lett.* **16**, 502 (1991).
28. D. U. Noske, N. Pandit, and J. R. Taylor, *Electron. Lett.* **28**, 2185 (1992).
29. K. Tamura, E. P. Ippen, H. A. Haus, and L. E. Nelson, *Opt. Lett.* **18**, 1080 (1993).
30. H. A. Haus, E. P. Ippen, H. A. Haus, and K. Tamura, *IEEE J. Quantum Electron.* **30**, 200(1994).
31. B. Nikolaus, D. Grischkowsky, and A. C. Balant, *Opt. Lett.* **8**, 189 (1983).
32. N. J. Halas and D. Grischkowsky, *Appl. Phys. Lett.* **48**, 823 (1986).
33. A. Hasagawa and F. Tappert, *Appl. Phys. Lett.* **23**, 142 (1973).
34. L. F. Mollenauer, R. H. Stolen, and J. P. Gordon, *Phys. Rev. Lett.* **45**, 1095 (1980).

35. M. Nakazawa, Y. Kimura, K. Suzuki, and H. Kubota, *J. Appl. Phys.* **66**, 2803 (1989).
36. L. F. Mollenauer and K. Smith, *Opt. Lett.* **13**, 675 (1988).
37. L. F. Mollenauer and K. Smith, in *Digest of Conference on Lasers and Electro-Optics* (Optical Society of America, Washington, D.C., 1989), paper TUU1.
38. K. Smith and L. F. Mollenauer, *Opt. Lett.* **14**, 1284 (1989).
39. L. F. Mollenauer, M. J. Neubelt, S. G. Evangelides, J. P. Gordon, J. R. Simpson, and L. G. Cohen, *Opt. Lett.* **15**, 1203 (1990).
40. L. F. Mollenauer, B. M. Nyman, M. J. Neubelt, G. Raybon, and S. G. Evangelides, *Electron. Lett.* **27**, 178 (1991).
41. C. D. Poole, *Opt. Lett.* **13**, 687 (1988).
42. C. R. Menyuk, *Opt. Lett.* **12**, 614 (1987); *J. Opt. Soc. Am. B* **5**, 392 (1988).
43. C. R. Menyuk, *IEEE J. Quantum Electron.* **25**, 2674 (1989).
44. Y. S. Kivshar, *J. Opt. Soc. Am. B* **7**, 2204 (1990).
45. X. D. Cao and C. J. McKinstrie, *J. Opt. Soc. Am. B* **10**, 1202 (1993).
46. Y. Kodama, *Phys. Lett. A* **123**, 276 (1987).
47. Y. S. Kivshar and B. A. Malomed, *Rev. Mod. Phys.* **61**, 763 (1989).
48. Y. S. Kivshar, *J. Opt. Soc. Am. B* **7**, 2204 (1990).
49. B. A. Malomed, *Phys. Rev. A* **43**, 410 (1991).
50. M. N. Islam, C. E. Socolich, and D. A. B. Miller, *Opt. Lett.* **15**, 909 (1990).
51. M. N. Islam, C. R. Menyuk, C.-J. Chen, and C. E. Socolich, *Opt. Lett.* **16**, 214 (1991).
52. B. A. Malomed and S. Wabnitz, *Opt. Lett.* **16**, 1388 (1991).
53. D. Strickland and G. Mourou, *Opt. Commun.* **55**, 216 (1985).

54. P. Maine, D. Strickland, P. Bado, M. Pessot, and G. Mourou, *IEEE J. Quantum Electron.* **QE-24**, 398 (1988).
55. C. Rouyer, E. Mazataud, I. Allais, A. Pierre, R. Rossage, S. Seznec, C. Sauteret, A. Migus, and G. Mourou, *OSA Proceedings on Shortwavelengths V: Physics with Intense Laser Pulses*, M. D. Perry and P. B. Corkum eds., San Diego, California, March 29-31, 1993.
56. T. Tajima and J. M. Dawson, *Phys. Rev. Lett.* **43**, 267 (1979).
57. L. M. Gorbunov and V. I. Kirsanov, *Sov. Phys. JETP* **66**, 290 (1987).
58. V. N. Tsytovich, U. DeAngelis, and R. Binham, *Comments Plasma Phys. Controlled Fusion* **12**, 249 (1989).
59. P. Sprangle, E. Esarey, A. Ting, and G. Joyce, *Appl. Phys. Lett.* **53**, 2146 (1988).
60. P. Sprangle, E. Esarey, and A. Ting, *Phys. Rev. Lett.* **64**, 2011(1990).
61. P. Sprangle, E. Esarey, and A. Ting, *Phys. Rev. A.* **41**, 4463 (1990).
62. C. Max, J. Arons, and A. B. Langdon, *Phys. Rev. Rev. Lett.* **33**, 209 (1974).
63. G. Schmidt and W. Horton, *Comments Plasma Phys. Controlled Fusion* **9**, 85 (1985).
64. P. Sprangle, C. M. Tang, and E. Esarey, *IEEE Trans. Plasma Sci.* **PS-15**, 145 (1987).
65. S. C. Wilks, J. M. Dawson, and W. B. Mori, *Phys. Rev. Lett.* **61**, 337 (1988).
66. E. Esarey, G. Joyce, and P. Sprangle, *Phys. Rev. A.* **44**, 3908(1991).
67. X. Liu, D. Umstadter, J. S. Coe, C. Y. Chien, E. Esarey, and P. Sprangle, in *Coherent Short Wavelength Radiation: Generation and Application*, edited by P. Bucksbaum and N. Ceglio (Optical Society of America, Washington, D.C., 1991).

68. P. Sprangle and E. Esarey, in *High-Brightness Beams for Advanced Accelerator Applications*, AIP Conf. Proc. **253**, edited by W. Destler and S. Guharay (AIP, New York, 1992), p. 87.
69. I. S. Aleksakhin, I. P. Zapesochnyi, and V. V. Suran, *JETP Lett.* **26**, 11 (1977).
70. A. L'Huillier, L. A. Lompre, G. Mainfray, and C. Manus, *J. Phys.* **B16**, 1363 (1983).
71. T. S. Luk, H. Pummer, K. Boyer, M. Shahidi, H. Egger, and C. K. Rhodes, *Phy. Rev. Lett.* **51**, 110 (1983).
72. S. Augst, D. D. Meyerhofer, D. Strickland, and S. L. Chin, *J. Opt. Soc. Am.* **B8**, 858 (1991).
73. P. Agostini, F. Fabre, G. Mainfray, G. Petite, and N. K. Rahman, *Phy. Rev. Lett.* **42**, 1127 (1979).
74. P. Kruit, J. Kimman, H. G. Muller, and M. J. van der Wiel, *Phy. Rev.* **A28**, 248 (1983).
75. A. L'Huillier, L. A. Lompre, M. Ferray, X. F. Li, G. Mainfray, and C. Manus, *Europhys. Lett.* **5**, 601 (1988).
76. OSA Proceedings on Short Wavelength Coherent Radiation: Generation and Applications, 1991, P. Buchsbaum and N. Ceglio, eds. (Optical Society of America, Washington, D. C. 1991).
77. Special issue on "The generation of coherent XUV and soft x-ray radiation," *J. Opt. Soc. Am. B* **4**, 530 (1987).
78. M. D. Feit and J. A. Fleck Jr., *Appl. Phys. Lett.* **24**, 169 (1974).
79. P. L. Berger and D. C. Smith, *Appl. Phys. Lett.* **21**, 167 (1972).
80. P. Monot, T. Auguste, L.-A. Lompre, G. Mainfray, and C. Mannus, *J. Opt. Soc. Am.* **B9**, 1569(1992).

81. T. Auguste, L.-A. Lompre, G. Mainfray, and C. Mannus, *Opt. Commun.* **89**, 145 (1992).
82. W. L. Leemans, C. E. Clayton, W. B. Mori, K. A. Karsh, P. W. Kaw, A. Dyson, and C. Joshi, *Phys. Rev. A* **46**, 1091 (1992).
83. X. Liu and D. Umstadter, *OSA Proceedings on Shortwavelengths V: Physics with Intense Laser Pulses*, M. D. Perry and P. B. Corkum eds., San Diego, California, March 29-31, 1993. p.45.
84. T. Auguste, P. Monot, G. Mainfray, and C. Manus, *Opt. Commun.* **105**, 292 (1994).
85. R. Rankin, C. E. Capjack, N. H. Burnett, and P. B. Corkum, *Opt. Lett.* **16**, 835 (1991).
86. S. C. Rae, *Opt. Commun.* **97**, 25 (1993).

CHAPTER 2

Frequency-Domain Interferometer for Measurements of Polarization Mode Dispersion in Birefringent Media

In this chapter, we discuss one of the most important properties of optical fibers, the polarization mode dispersion (PMD). Polarization mode dispersion causes a short optical pulse to split into two components, each propagates with its polarization aligned to one of the two principal polarization states of the fiber. PMD limits the transmission bandwidth in fiber communication systems, increases the soliton threshold in optical fibers, and changes the characteristics of soliton collisions in optical fibers. There are many methods for measuring PMD, we have developed a new method based on the frequency-domain interferometry (FDI). In this chapter, we have discussed the fundamentals of FDI, and its applications in measuring PMD in optical fibers and group velocity walkaway in nonlinear crystals. This technique is based on the spectral interference of two short pulses in the frequency domain. In the frequency domain, two temporally separated pulses interfere in the same way that two waves with different frequencies beat in time domain. Measuring the interference fringes in the frequency domain gives the temporal delay of two short pulses.

2.1. Introduction

Single-mode optical fibers have been increasingly used in (coherent) optical transmission systems and as polarization-dependent fiber-optic sensors. In these applications, it is of fundamental importance to know the polarization properties of single-mode fibers because these properties govern the degree and state of the polarization of the radiation. It is well-known that birefringence in optical fibers can be induced by built-in stress or by geometric deformation of the fiber core.^{1,2} The most important parameters characterizing birefringent fibers are the polarization mode dispersion (PMD) and modal birefringence (MB). PMD is the group delay time difference between two orthogonally polarized HE_{11} modes, while MB is the refractive index difference between these two modes. Unlike birefringence in crystals, optical fibers suffer from the random coupling of two polarization modes due to the uncontrollable random changes of local birefringence axes. Depending on the relative length of optical fiber compared to the mode coupling length, PMD shows very different characteristics. For instance, the average PMD is linearly proportional to the propagation distance when the fiber length is much shorter than the mode coupling length, while PMD is proportional to the square root of fiber length when the fiber length is much longer than the mode coupling length. In the later case, the random mode coupling can be described through statistical picture.³ PMD is a fundamental characteristic of a fiber or a device that describe its propensity to split a narrow-band optical input pulse into two temporally separate output pulses according to its state of polarization, which results in bandwidth limitations.⁴ PMD has two contributions: one is the phase delay, which is proportional to MB; the other arises from dispersion difference between two modes. Since the first experimental verifications of PMD in birefringent optical fibers made by Rashleigh and Ulrich,⁵ many methods for measuring PMD in single-mode fibers have been reported.⁶⁻²⁴ These methods fall

into six categories: (i) optical short-pulse methods,⁸ (ii) frequency domain techniques,^{9, 10} (iii) interferometric methods,^{5, 9–17} (iv) optical heterodyne techniques,^{18–19} (v) Jones matrix eigenanalysis^{20–22} (vi) wavelength scanning^{23,–25} The white-light interferometric method has proved to be very accurate and applicable to meter-length samples,^{5,17} and better results can be obtained by the method of Jones matrix eigenanalysis with a resolution of roughly 50 attoseconds (50×10^{-18} s).²²

Recently, PMD has attracted many investigations due to its important impact on fiber communications.^{20–25} In this thesis, we will focus on other important effects of PMD on the nonlinear propagation of short pulses in optical fibers. Previously, people concentrated on the measurement of PMD and its effects on the linear propagation of short pulses. To the first order, PMD causes a short pulse to be split into two. However in the nonlinear regime, especially in the system of soliton propagation, this pulse-splitting effect raise the question of soliton stability in soliton communication systems. On the other hand, PMD also strongly changes the characteristics of soliton collisions in birefringent optical fibers. In this chapter, we will describe a new method of measuring PMD, while studying the effects of PMD on nonlinear propagation of short pulses in Ch. 4. This new method is based on frequency-domain interferometry. There are several advantages of this new method compared to previous methods. First of all, this method provides a dynamic measurement of PMD without tedious calculations and curve fitting. For instance, the method of Jones matrix eigenanalysis provides very good resolution, but requires solution of eigenvalues of the Jones matrix based on three different steps of measurements. In the method of wavelength scanning, the wavelength resolution is usually poor (>0.5 nm), which results in low resolution in the case of high birefringence. However, our new method provides a dynamic measurement as well as

high resolution for the measurement PMD in high birefringent fibers. Finally, this method is even ideal for the applications involving propagation of short pulses, since the same short pulses can be used to measure PMD, thus the results are immediately relevant for the application.

This new method has many other applications. In this chapter, we apply this technique in the measurement of group velocity walkaway in nonlinear crystals, which is a very important factor in determining the wavelength conversion efficiency of short pulses in nonlinear crystal. Frequency conversion in nonlinear crystals has been an important method for obtaining coherent radiation sources with wavelengths not covered by lasers. This is especially true in applications involving ultrashort laser pulses. Frequency conversion includes second, and higher harmonic generation,²⁶⁻²⁸ and optical parametric oscillators (OPO) and amplifiers (OPA).^{29,30} A major limitation to ultrashort frequency conversion is the group-velocity walkaway(GVW) between the ordinary (o-wave) and extraordinary (e-wave) waves due to the different group velocities for the two polarizations.³¹ Since birefringence and dispersion exist in all nonlinear crystals, the GVW effect becomes a fundamental factor in determining the frequency conversion efficiency on applications involving short pulses. The walkaway has been used to increase the conversion efficiency of type II doubling of 1 μm , 1 ps laser pulse by using a second crystal to predelay the extraordinary wave relative to the ordinary wave.^{26,27} It was also found that the pulse duration could be reduced from 1 ps to 200 fs.³² Chien et al. ²⁸ have studied the conversion efficiency of high power ultrashort pulses and have found that the GVW between two polarization causes reconversion of the second harmonic back to the fundamental frequency.

Typically, the walkaway is inferred by measuring the refractive indices and the dispersion of the e- and o-waves. In this work we report on the first direct

measurement of the GVW between the e- and o- waves in a birefringent crystal. The same ultrashort pulse which is to be frequency converted can be used for these measurements. Most values of the refractive index have been obtained by the minimum-deviation method(MDM), and are accurate to the fifth decimal place.³³ Extensive measurements of refractive indices of nonlinear crystals isomorphous to KH_2PO_4 have been made by Kirby and DeShazer.³⁴ Although MDM provides an accurate measurement of the refractive indices of e- and o- waves, it is not convenient for many applications involving nonlinear frequency conversion. Since the MDM measurement requires a high quality prism made of the sample crystal, this method can be expensive and impractical for ordinary frequency conversion applications. The dispersion properties are usually obtained by fitting to the Sellmeier or Zernike formula, ^{35,36} which requires multiple measurements with different light frequencies. Since narrow spectral lines of different lamps are used in MDM, it is possible that no experimental data exists for some specific wavelength that is used in frequency conversion experiments. Another disadvantage of this method is that the refractive indices of o- and e- waves is a function of propagation direction. All the calculations require the relative angle between the propagation direction and the optical axis to be known precisely. Hence precise locations of optical axes and propagation angle are required before the final calculations can be made.

There are several other advantages of technique presented here for nonlinear frequency conversion. In practical applications of frequency conversion involving short pulses, it is desirable to know the walkaway parameter for the laser frequency involved. The walkaway can be measured using the same laser pulses that will be used in frequency conversion, therefore the measured data about the walkaway is immediately relevant. For the applications involving cascade processes of frequency conversion of short pulses, it is crucial to know the polarization direction, or the

crystal orientation which correspond to the minimum walkaway, so that the orientations of nonlinear crystal for the next stage of frequency conversion can be optimized.³² Our method provides real time information about the GVW, its simplicity will be helpful in the system design of devices of nonlinear frequency conversion. To our knowledge, this method provides the first direct measurement of angular dependence of the GVW.

2.2 Basics of frequency-domain interferometer

In this chapter, a new technique based on frequency-domain interferometry (FDI)^{37,38} has been used to measure the PMD, or the group-velocity walkaway of short pulses in birefringent media. As the name implies, this technique is based on the spectral interference of two short pulses in the frequency domain. The intrinsic phase delay between the fast and slow modes of a birefringent medium is used. Due to the different group delays, the two pulses launched along the fast and slow arms will come out of the medium at different times. In the frequency domain, two temporally separated pulses interfere in the same way that two waves with different frequencies beat in time domain. In the frequency-domain interferometer described in this work, the measurement of the modulation period of the interference fringes in frequency domain gives the group-velocity walkaway (GVW) directly without further assumptions about the properties of the light source. By analogy with an ordinary interferometer, the two axes of the birefringent medium can be regarded as two interfering arms, while a polarizer placed at the output end of the medium combines the two field components to generate interference fringes in frequency domain. Temporally separated pulses can interfere owing to the linear dispersion of the grating in a spectrometer.^{37,38} Different frequency components propagate along different directions, which results in a frequency-dependent time delay. Therefore, two

temporally separated pulses can physically overlap on the detector surface of the spectrometer. Compared with other methods, the experimental setup of our interferometer is quite simple; the alignment is also very easy. More importantly, the experimental data is directly related to the GVW; no further curve fitting is needed.

In order to understand the physics of the frequency-domain interferometer, we need to understand the properties of a spectrometer. A simplified version of a spectrometer is shown in Fig. (2.1). The incident beam is collimated, and has a diameter D . The incident angle to the grating is i , while the diffracted angle is α . Assuming two pulses with pulse width τ_p are separated by T , we find that the energy fronts, or the amplitude fronts of these two pulses are no longer parallel to the phase fronts. At the focus of the image lens, each pulse is temporally stretched to a duration of $DN\lambda/\cos(i)c$, where N is the groove number of the grating, λ is the wavelength of the pulses, c is the speed of light. It is easy to see that two separate pulses can physically overlap with each other at the focal plane, or the frequency plane. Note that no such overlapping is possible if the original separation T is greater than the grating stretching $DN\lambda/\cos(i)c$, as can be seen in Fig. (2.1).

The configuration of the frequency-domain interferometer is shown schematically in Fig. (2.1). The birefringent axes are labeled as x and y ; the laser light propagates along the z direction. Two identical pulses temporally displaced by T are launched into the birefringent fiber with their polarization directions aligned to the x and y axes, respectively. At the input plane ($z = 0$), the electric fields of these two pulses can be expressed by

$$E_x(t, z = 0) = E(t) \exp(i \omega_0 t)$$

$$E_y(t, z = 0) = E(t - T) \exp[i \omega_0 (t - T)] , \quad (2.1)$$

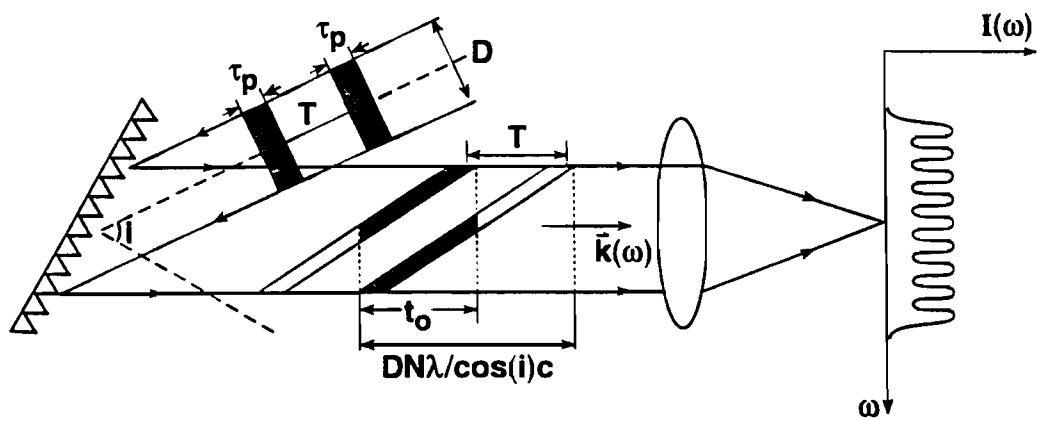


Fig. 2.1 Temporal stretching of short pulses in a spectrometer.

where $E(t)$ is the slowly varying envelope of the two pulses and ω_0 is the carrier frequency of the laser pulses. At the exit end of the fiber, the Fourier transformations of the electric fields are

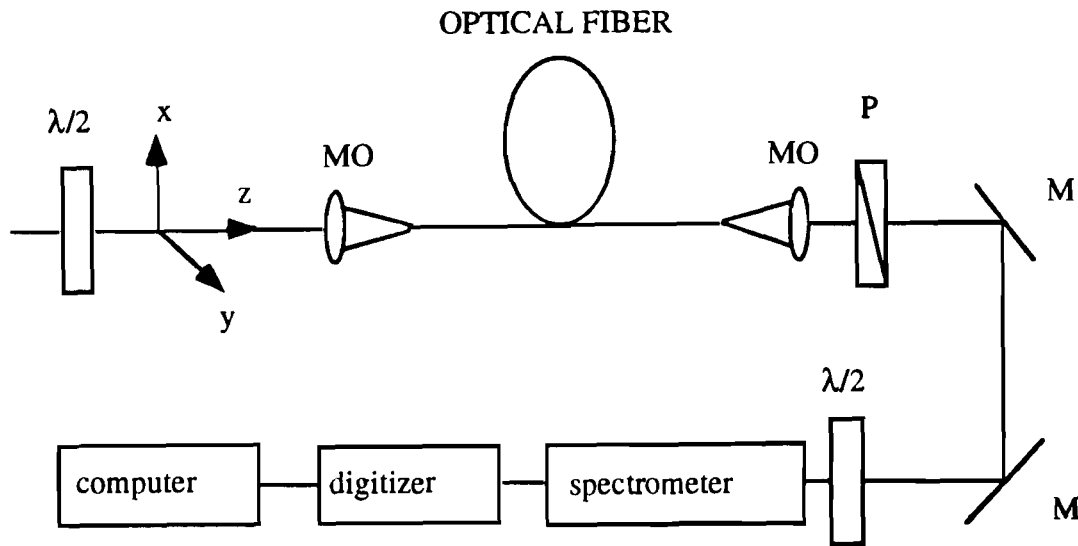


Fig. 2.2 The experimental setup. Where $\lambda/2$ means half-wave plate, MO microscope objectives, P polarizer, and M mirror. The linearly polarized light is coupled into the optical fiber with the polarization direction aligned to 45° with respect to fiber axes.

$$E_x(\omega, z = L) = E(\omega - \omega_0) \exp[-i \beta_x(\omega) L]$$

$$E_y(\omega, z = L) = E(\omega - \omega_0) \exp[-i \beta_y(\omega) L] \exp(-i \omega T), \quad (2.2)$$

where $E(\omega - \omega_0)$ is the Fourier transform of $E(t)$ and $\beta_x(\omega)$ and $\beta_y(\omega)$ are propagation constants of the x and y modes.

A polarizer with its transmission axis set to be 45° with respect to the x and y axis combines the two electric fields,

$$E_{out}(\omega, z = L) = \frac{1}{2} [E_x(\omega, z = L) + E_y(\omega, z = L)] . \quad (2.3)$$

The power spectrum detected by a spectrometer can be expressed as

$$I(\omega) = \frac{1}{4} |E(\omega - \omega_0)|^2 \{1 + \cos[\Delta\beta(\omega)L + \omega T]\} , \quad (2.4)$$

where $\Delta\beta(\omega) = \beta_x(\omega) - \beta_y(\omega)$ is the modal birefringence and can be expanded as follows:

$$\Delta\beta(\omega) = \Delta\beta(\omega_0) + \frac{d\Delta\beta(\omega_0)}{d\omega} \Delta\omega + \frac{1}{2} \frac{d^2\Delta\beta(\omega_0)}{d\omega^2} \Delta\omega^2 + \dots , \quad (2.5)$$

where $d\Delta\beta/d\omega$ is the polarization mode dispersion. The third term in Eq. (2.5) is the difference of the group velocity dispersion (GVD), which describes the difference of the pulse spreading in two principal axes. For subpicosecond pulses, the dispersion distance (the distance at which pulse width becomes twice the initial value) can be shorter than 1 m.³⁹ However, as pointed out in Ref. (5), this term can be ignored since the temporal spreading is almost the same for each mode; in other words, the difference of temporal spreading due to GVD is still negligible. Substituting Eq. (2.5) into Eq. (2.4) gives

$$I(\omega) = \frac{1}{4} |E(\omega - \omega_0)|^2 \left\{ 1 + \cos[\Delta\beta(\omega_0) + T\omega_0 + \left(\frac{d\Delta\beta}{d\omega}L + T\right)\Delta\omega] \right\}. \quad (2.6)$$

From Eq. (2.6), it is easy to find that the periodicity of the interference fringes is given by

$$\Omega = 2\pi / \left(\frac{d\Delta\beta}{d\omega}L + T \right). \quad (2.7)$$

The polarization mode dispersion can be determined in terms of measured quantity Ω , that is, the fringe spacing in frequency domain. From Eq. (72.), we have

$$\frac{d\Delta\beta}{d\omega} = \left(\frac{2\pi}{\Omega} - T \right) / L. \quad (2.8)$$

Note that Eq. (2.8) provides two ways of measuring PMD. First, no optical delay is needed, which means $T = 0$. Measuring the fiber length L and interference spacing Ω gives the required result of PMD. This method is very simple to implement. On the other hand, it is possible to adjust the temporal delay such that $\Omega = \text{infinity}$, then $\text{PMD} = -T/L$. Physically, this means that the pre-delay T is set such that two pulses come out of the fiber at same time; therefore there will be no interference in frequency domain.

2.3 Experimental results

The experimental setup is shown in Fig. (2.2). The laser beam originates from an actively mode-locked Nd:YLF oscillator that produces a 50-ps pulse train at a

wavelength of 1054 nm with a repetition rate of 100 MHz. The pulse train goes through an 800-m, single-mode optical fiber that increases the bandwidth from 0.3 Å to 31.6 Å through the combined effects of self-phase-modulation (SPM) and GVD.³⁹ The pulses are then temporally compressed to 1 ps by a double-pass grating pair. Two microscope objectives are used to couple the laser beam into and out of a highly birefringent fiber (3M product, FS-HB-5651). A $\lambda/2$ -wave plate placed in front of the fiber was used to control the polarization direction of the incident laser beam. A polarizer placed at the exit end of fiber was used to combine the electric field components of the fast and slow modes. Finally the collimated output beam was sent to the spectrometer with an optical multichannel analyzer (OMA). Another $\lambda/2$ -wave plate placed in front of the spectrometer was used to match the polarization direction of the laser beam to that of the grating inside the spectrometer. The waveguide parameters of the fiber used in the experiment are listed in Table 2.1.

The input spectrum $\left[|E(\omega - \omega_0)|^2\right]$ is shown in Fig. (2.3). The power spectrum has nearly a square-top shape with a width about 31.60 Å. In the experiment, the input polarization direction was adjusted to be 45° with respect to the fast and slow axes of the birefringent fiber. The polarizer was also aligned to the same angle as described in Eq. (2.3). The frequency-domain interference fringes are shown in Fig. (2.4). Least squares method is used to fit Fig. (2.4) using Eq. (2.6); Ω was found to be 22.7 ± 0.1 pixels, giving a modulational period of the interference fringes of 9.13 ± 0.04 Å, corresponding to a temporal delay of 3.91 ± 0.04 ps. The length of the fiber was measured with an accuracy of 1 mm. According to Eq. (2.8), the PMD is found to be 1.42 ps/m with an accuracy of 1%. It is well known that $d\Delta\beta/d\omega$ can be expressed as

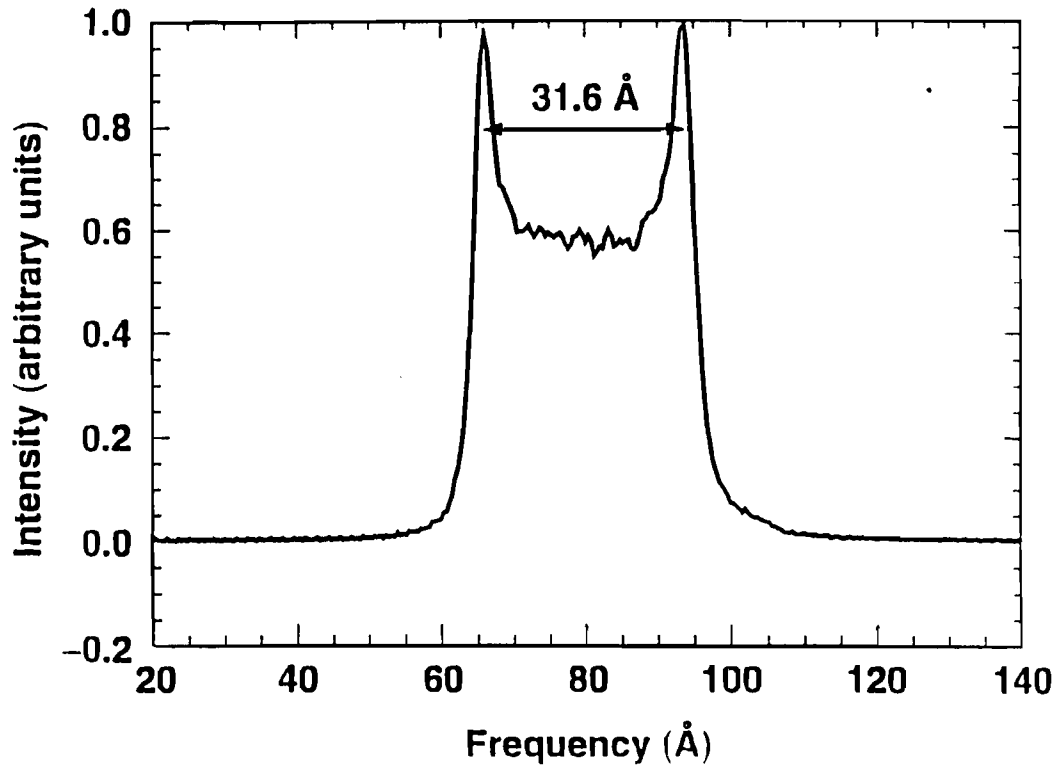


Fig. 2.3 The spectrum of the incident pulses. The spectrum shape is typical of the combined effects of SPM and GVD. The peak-peak width is 31.60 Å.

the PMD is found to be 1.42 ps/m with an accuracy of 1%. It is well known that $d\Delta\beta/d\omega$ can be expressed as

$$\frac{d\Delta\beta}{d\omega} = \frac{\Delta n}{c} + \frac{\omega}{c} \frac{d\Delta n}{d\omega}, \quad (2.9)$$

where Δn is the modal birefringence. Table 1 shows that the first term on the right-hand side of Eq. (2.9) equals 1.3 ± 0.1 ps/m (the uncertainty comes from the fact that there is not enough information about the sample fiber, see Table 2.1), which is very close to the measured PMD. This means that the contribution of the second term in Eq. (2.9) is much smaller than the first term, which is true in most stress induced birefringent fibers.^{40,41} In fact, it is easy to show that the first term in Eq. (2.9) takes approximately 90% of the total group delay in the case studied here.

Table 2.1: Waveguide Parameters of the Fiber Used in the Experiment.

fiber length	2.750 m
mode field diameter	6.8 μm
fiber diameter	100 μm
operating wavelength	1.060 μm
cutoff wavelength	1.000 μm
birefringence	4×10^{-4}
loss	<2 dB/km

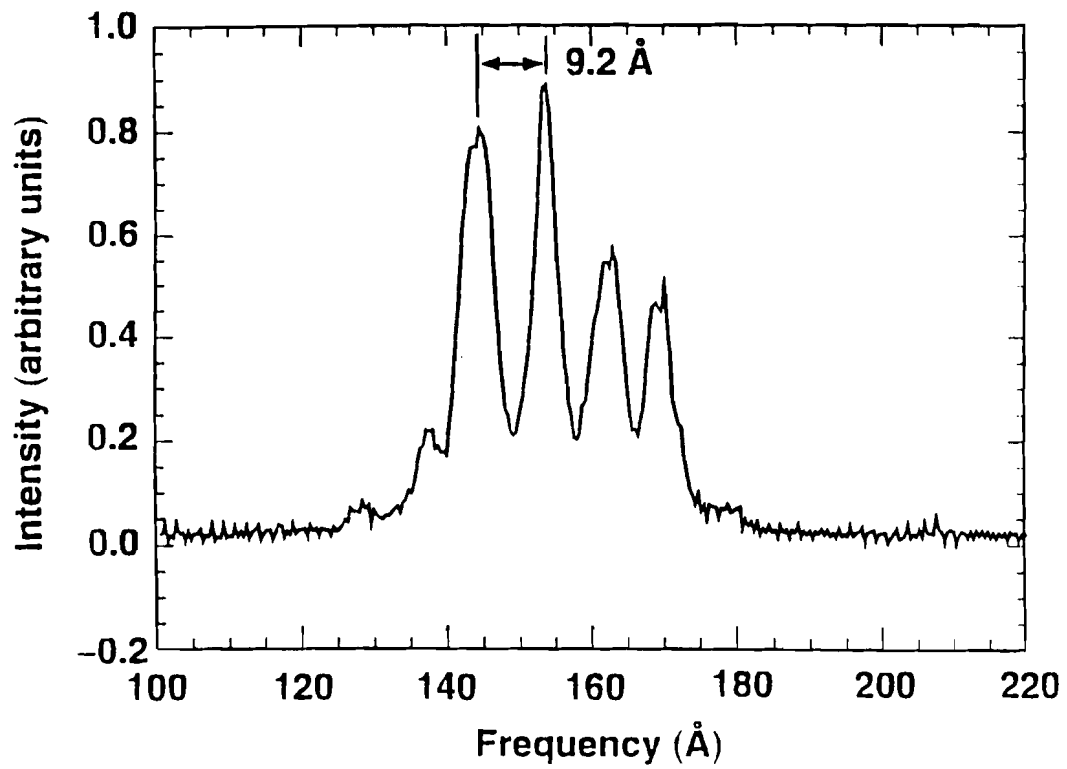


Fig. 2.4 Frequency-domain interference fringes. The fringe spacing is measured to be 9.13 Å.

Table 2.2 Parameters of Nonlinear Crystals and Measured Walk-off

Crystal	Cut angle	Length ×2 (cm)	Walk-off (a) (ps/cm)	Walk-off (b) (ps/cm)
CDA I	85°	2.50	1.00 ± 0.01	1.01
KDP* II	53.7°	1.50	0.94 ± 0.02	0.97
KDP II	59.2°	1.90	1.35 ± 0.02	1.33
KDP I	41.2°	1.029 ± 0.005		0.79

(a) measured results

(b) calculated results³⁴

From Eq. (2.4), the power spectrum detected in the spectrometer takes following form

$$I(\omega) = \frac{1}{4} |E(\omega - \omega_0)|^2 [1 + \cos(\phi_0 + \Delta\tau\Delta\omega)] \quad (2.10)$$

where $E(\omega - \omega_0)$ is the spectrum of the incident pulse; ϕ_0 is a constant, $\Delta\tau$ is the temporal delay between the two pulses traveling along the fast and slow axes of birefringent medium; $\Delta\omega = \omega - \omega_0$. Therefore the GVW is just the periodicity of the interference pattern in frequency domain.

The experimental setup is similar to Fig. (2.2), except the fiber is replaced by a nonlinear crystal. The frequency-domain interference fringes for a 2.5 cm thick CDA crystal are shown in Fig.(2. 5). A least squares method is used to fit Fig. (2.5) using

Eq. (2.10), as shown in dashed curve. There are three sources of error in the measurements, the error in measuring the lengths of the crystals, the error in calibrating the spectrometer, and the error in determining the spacing of the interference fringes. The uncertainty of the thickness measurement is 1 %. The calibration was performed using five spectral lines of Rubidium lamp ranging from 1053 nm to 1073 nm. The spectral lines were fitted with Lorentzian line shape, and the overall uncertainty in the calibration was found to be 0.2 %. The least square fit for the interference fringes gives an error of 0.3 %. The largest uncertainty comes from the measurement of the thickness of the crystals. After taking into account of these three error sources, we found that the error in determining the temporal walkaway is about 1 %. The GVW parameters of several commonly used nonlinear crystals have been measured, the results are listed in Table 2.2. The cut angles and lengths of the tested crystals are also listed. The last column of Table 2.2. shows the calculated values of the GVW based on the dispersion data of Ref.[34]. The measured results are very close to the calculated ones, as can be seen from Table 2.2.

It is well-known that the refractive index of extraordinary wave is a function of propagation direction, which means that the GVW is also a function of propagation direction. Fig.(2.6) shows the dependence of walkaway on the propagation angle. The angle is measured with respect to the phase-matching angle of the crystal (KDPII) in YZ plane. The scattered triangles are experimental data, the solid curve is the theoretical prediction based on material dispersion³⁴. The experimental data fits the theory, with an accuracy of 1%. It should be mentioned that the angle in Fig. 6 is the angle inside the crystal, that is, Snell's law has been used to obtain the internal angle. Since the crystal is cubic, the propagation distance is also a function of angle, which has been taken into account in Fig. (2.6).

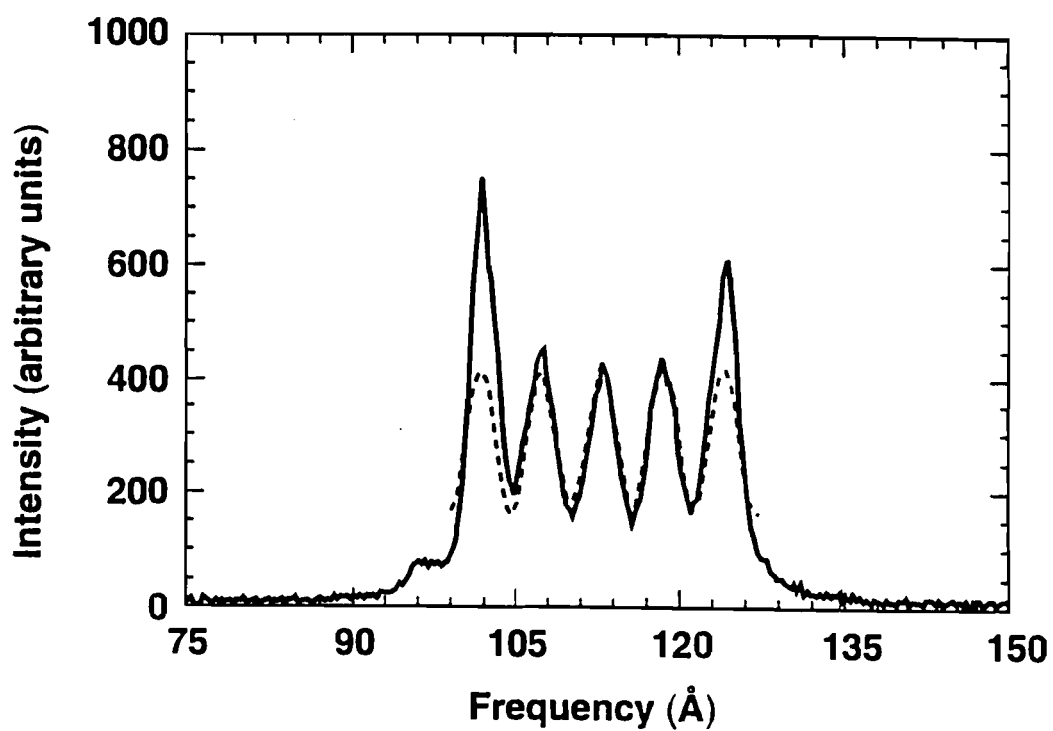


Fig. 2.5 Frequency-domain interference fringes of sample CDA I. The fringe spacing is measured to be 6.7 Å. The solid line is the experimental data, while the dashed line is the theoretical fitting.

2.4 Conclusions

In conclusion, a new technique based on frequency-domain interferometry has been used to measure the polarization mode dispersion of birefringent media. In contrast to the usual interferometric methods that measure the interference visibility as a function of optical delay between two interfering arms, we measure the periodicity of the interference fringes in frequency domain by using short broadband optical pulses. No curve fitting is needed to find the values of PMD since the measured modulation period of the fringes is directly related to PMD, as shown in Eq. (2.8). Two different schemes of measurement have been discussed in detail. These two methods differ from each other in that one needs an optical delay line, while the other does not. The method without an optical delay line has been demonstrated experimentally. There are several advantages of this new method for measuring the GVW in a birefringent medium. First of all, the measurement is direct. The group-velocity walkaway can be measured in real time, which is useful for applications in which the GVW can be controlled by tuning the crystals. Secondly, for most applications of frequency conversion, this method provides the values of GVW at the appropriate wavelength, since the source is the same source that is used in the nonlinear frequency conversion. Thirdly, this method makes it possible to measure the angular dependence of GVW, which is useful for experiments involving serial frequency conversion. The walkaway can be compensated for in the second crystal.³² Our method can be used to align the crystal by monitor the compensation. Compared to other methods, our method provides reasonably good accuracy, as well as experimental simplicity. It should be mentioned that our method is linear in the sense that it does not depend on the laser power. In our experiment, the pulses were not transform limited, in other words, the pulses are slightly chirped. It is believed

that the chirp may be responsible for the finite visibility of the interference patterns, so it could affect the accuracy of the measurements when the visibility is poor.

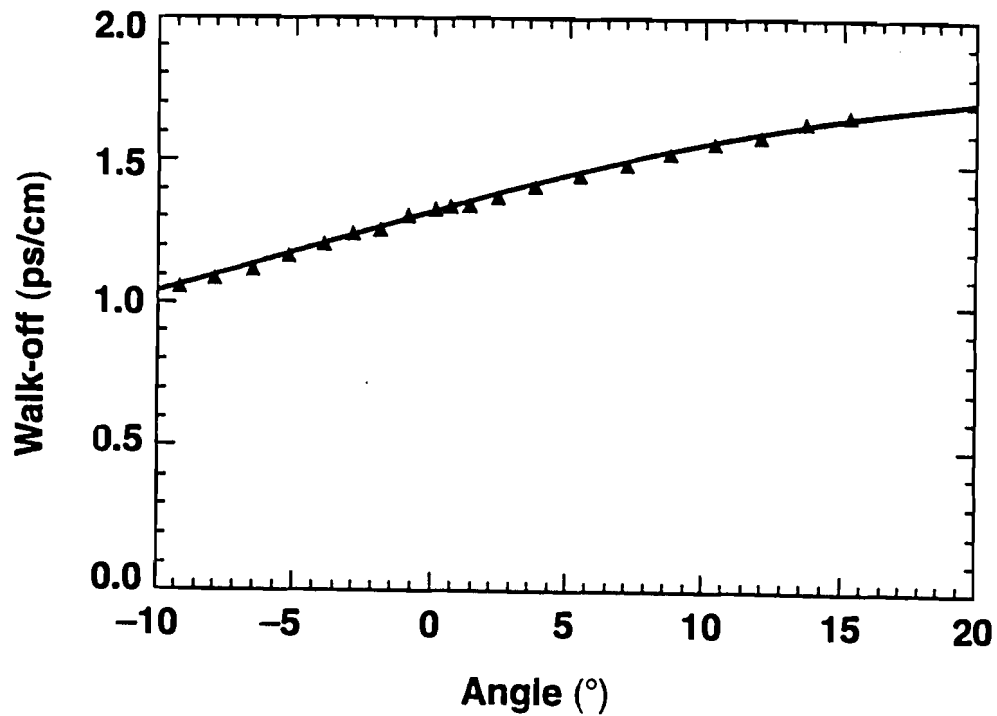


Fig. 2.6 Dependence of the group-velocity walkaway on the propagation direction. The angle is measured with respect to the phase-matching angle of the sample (KDPII).

REFERENCES

1. R. H. Stolen, W. Pleibel, and J. R. Simpson, *IEEE J. Lightwave Technol.* **LT-2**, 639 (1984).
2. S. C. Rashleigh and M. J. Marrone, *IEEE J. Quantum Electron.* **QE-18**, 1515 (1982).
3. G. J. Foschini and C. D. Poole, *J. Lightwave Technol.*, **9**, 1439 (1991).
4. I. P. Kaminow, *IEEE J. Quantum Electron.* **QE-17**, 15 (1981).
5. S. C. Rashleigh and R. Ulrich, *Opt. Lett.* **3**, 60 (1978).
6. Y. Sasaki, N. Shibata, and J. Noda, *Electron. Lett.* **18**, 997 (1982).
7. M. Monerie, P. Lamouler, and L. Jeunhomme, *Electron. Lett.* **16**, 907 (1980).
8. Y. Yamabayashi and M. Saruwatari, *Electron. Lett.* **19**, 239 (1983).
9. K. Mochizuki, Y. Namihira, and H. Wakabayashi, *Electron. Lett.* **17**, 153 (1981).
10. N. Shibata, M. Tateda, and S. Seikai, *IEEE J. Quantum Electron.* **QE-18**, 53 (1982).
11. N. Imoto and M. Ikeda, *IEEE J. Quantum Electron.* **QE-17**, 542 (1981).
12. S. C. Rashleigh, *Opt. Lett.* **7**, 294 (1982).
13. S. C. Rashleigh, *Opt. Lett.* **8**, 336 (1983).
14. A. B. Grudinin, G. L. Dyankov, and V. B. Neustruev, *Sov. J. Quantum Electron.* **16**, 1522 (1986).
15. L. Thévenaz, V. de Coulon, and J. P. Von der Weid, *Opt. Lett.* **12**, 619 (1987).
16. J.-P. Von der Weid, L. Thevenaz, and J.-P. Pellaux, *Electron. Lett.* **23**, 151 (1987).
17. W. J. Bock and W. Urbanczyk, *Appl. Opt.* **32**, 5841 (1993).
18. N. Shibata, M Tsubokawa, and S. Seikai, *Electron. Lett.* **20**, 1055 (1984).
19. N. Shibata, M. Tsubokawa, and S. Seikai, *Opt. Lett.* **10**, 92 (1985).

20. B. L. Heffner, *IEEE Photon. Technol. Lett.*, **5**, 814 (1993).
21. B. L. Heffner, *IEEE Photon. Technol. Lett.*, **4**, 1066 (1992).
22. B. L. Heffner, *Opt. Lett.*, **18**, 2102 (1993).
23. C. D. Poole, J. H. Winters, and J. A. Nagel, *Opt. Lett.*, **16**, 372 (1991).
24. C. D. Poole, *Opt. Lett.*, **14**, 523 (1989).
25. C. D. Poole, *Opt. Lett.*, **13**, 687 (1988).
26. Y. Wang, and R. Dragila, *Phys. Rev. A* **41**, 5645 (1990).
27. Y. Wang, B Luther-Davies, Y.-H. Chuang, R. S. Craxton, and D. D. Meyerhofer, *Opt. Lett.* **16**, 1862 (1991).
28. C. Y. Chien, G. Korn, J. S. Coe, J. Squier, G. Mourou, and R. S. Craxton, submitted to *Opt. Lett.*, to be published.
29. R. L. Byer, *J. Opt. Soc. Am. B*, **10**, 1656 (1993).
30. R. L. Byer, *J. Opt. Soc. Am. B*, **10**, 2148 (1993).
31. R. W. Boyd, *Nonlinear Optics* (Academic Press, San Diego, 1992).
32. Y. Wang and B. Luther-Davies, *Opt. Lett.* **17**, 1459 (1992).
33. W. L. Wolfe, Properties of optical materials, in *Handbook of Optics*, W. G. Driscoll ed., (McGraw-Hill Publishing Company, 1978)
34. K. W. Kirby and L. G. DeShazer, *J. Opt. Soc. Am. B*, **4**, 1072 (1987).
35. M. Born and E. Wolf, *Principles of Optics*, 6th ed. (Pergamon, Oxford, 1986).
36. F. Nernike, Jr., *J. Opt. Soc. Am.* **54**, 1215 (1964).
37. N. F. Scherer, R. J. Carlson, and A. Matro, M. Du, A. J. Ruggiero, V. Romero-Rochin, J. A. Cina, G. R. Fleming, and S. A. Rice, *J. Chem. Phys.* **95**, 1487 (1991).
38. E. Tokunaga, A. Terasaki, and T. Kobayashi, *Opt. Lett.* **17**, 1131 (1992).
39. G. P. Agrawal, *Nonlinear Fiber Optics* (Academic, Boston, 1989), Chap. 3–5.
40. N. K. Sinha, *Phys. Chem. Glasses*, **18**, 66(1978).

41. N. Shibata, K. Okamoto, K. Suzuki, and V. Iehida, *J. Opt. Soc. Am.* **73**, 1972 (1983).

CHAPTER 3

Nonlinear Birefringence and its Applications

In recent years, nonlinear birefringence has been found many applications in ultrafast optical pulse shaping or cleaning, and all-optical switching. Optical fibers are the idea media for the study of nonlinear birefringence. In this chapter, we investigated nonlinear birefringence in two different regimes: (a) linear birefringence dominates nonlinear birefringence; (b) nonlinear birefringence dominates. In the first case, we experimentally confirmed the dependence of nonlinear transmission on the incident polarization direction with respect to the birefringent axes. The existence of an optimal incident polarization angle will be useful in the optimization of nonlinear transmission. We also proposed and analyzed an improved scheme of pulse shaping using nonlinear polarization rotation. It was found that our improved scheme is much more efficient than the previous scheme. The peak transmission can be increased more than three times, from 7% to 24% for a incident power that is equivalent to that of generating a self-phase modulation(ϕ_{spm}) of π . For $\phi_{\text{spm}} = 2\pi$, the gain in nonlinear transmission is about 2.5 times, corresponding an increase from 23% to 57%. For higher power, the gain becomes saturated. Since stimulated Raman and Brillouin scattering limit the power level that can be used, this improved scheme will be very useful for many applications involving moderate power levels.

3.1 The origin of nonlinear birefringence

Birefringence is an optical property of an anisotropic optical medium when its refractive index depends on the polarization states of an incident optical radiation. For a given propagation direction, there are two polarization eigenstates that have different refractive indices. This birefringence is referred to as linear birefringence compared to the nonlinear birefringence we are going to study in this chapter. Linear birefringence is a property of an optical medium itself, typical of anisotropic media such as crystals. Nonlinear birefringence, however, is a birefringence induced by the intense optical radiation that propagates in the medium; it can exist in all nonlinear media. Nonlinear birefringence is simply a vectorial representation of nonlinear refraction, thus it is a universal phenomenon for all nonlinear media, both isotropic and anisotropic. In order to compare linear and nonlinear birefringence, we first review the basic results of linear birefringence. In a birefringent medium, there exist two polarization eigenstates of an incident laser beam that will not change during the propagation along a given direction in the medium. The corresponding refractive index and thus propagation velocities are different for each eigenstate. Usually, an eigenstate with larger(smaller) refractive index is called slow(fast) mode since the group velocity is smaller(higher). If these polarization eigenstates are linearly (circularly) polarized states, then the medium is called linearly(circularly) birefringent. It can also be elliptically birefringent if the eigenstates are elliptically polarized. Nonlinear birefringence has similar characteristics in the sense of polarization eigenstates. However, there are several important differences between linear and nonlinear birefringence. First of all, as mentioned previously, the physical origin of linear and nonlinear birefringence is different; linear birefringence comes from the material asymmetry, while nonlinear birefringence is due to the vectorial aspects of nonlinear refraction, independent of material structure. Secondly, linear

birefringence is usually dominated by one type of birefringence, in other words, it is either linearly birefringent or circularly birefringent. Nonlinear birefringence can support simultaneously two kinds of nonlinear eigenstates, both linearly and circularly polarized eigenstates.¹ If the incident polarization state is either linear or circular, then the output polarization state will be the same as the incident polarization state. Thirdly, the evolution of polarization states is very different for linear and nonlinear birefringence. In a medium with linear birefringence, the polarization state changes periodically from linearly polarized to elliptically or circularly polarized, and then back to linearly polarized, the polarization ellipticity evolves periodically between zero and 1. However in the case of nonlinear birefringence, the ellipticity is a constant of motion, only the orientation of the polarization ellipse changes periodically with propagation distance. The distance at which the polarization state go through a complete cycle is called beat length in the case of linear birefringence, and is given by $\lambda/\Delta n$, where λ is the wavelength of the optical radiation, Δn is the refractive index difference between the two eigenstates. In the case of nonlinear birefringence, the output ellipticity is the same as the input, it is the azimuth orientation of the polarization ellipse that changes periodically with a constant angular velocity determined by both the laser intensity and the polarization ellipticity. In fact, nonlinear birefringence is very different from linear birefringence, which is why nonlinear birefringence is sometimes called nonlinear polarization rotation or ellipse rotation to emphasize the fact that nonlinear birefringence mainly causes a rigid rotation of the polarization ellipse. Nonlinear birefringence is more like optical activity than linear birefringence.

As we mentioned before, nonlinear birefringence is just a vectoral representation of nonlinear refraction, therefore nonlinear birefringence will appear at the same time as nonlinear refraction is observed. In other words, nonlinear

birefringence will be accompanied by self-focusing or self-defocusing in a bulk medium. Since self-focusing (self-defocusing) results in an increase(decrease) in peak intensity or a reduction(increase) in beam size, the nonlinear phase modulation or polarization state will also be modified in a bulk medium. In order to prevent the complication of nonlinear transverse effects, one needs to limit the medium length to be smaller than self-focusing (self-defocusing) distance. Since the nonlinear polarization rotation is proportional to the product of incident power and the effective interaction distance, this limitation of medium length increases the power requirements, which limits its practical applications. The advances in optical fiber fabrication have made it possible to obtain single-mode fibers with small core size and extremely low loss. The small core size makes it possible to obtain high intensity with relatively low incident average power, while low loss makes it possible for an optical pulse to propagate thousands of meters without significant reduction in peak power. On the other hand, the transverse effect is absent in optical fibers due to their waveguide nature. Therefore, a significant amount of nonlinear phase modulation is possible for very low input power, which is very useful in practical applications. All these advantages make optical fibers an ideal medium for the study of nonlinear birefringence and its practical applications.

Optical fibers can be classified into two categories according to whether they are birefringent or not. The difference in refractive indices of two polarization eigenmodes or birefringent axes, Δn , is usually used to characterize the significance of linear birefringence. For instance, an optical fiber with $\Delta n > 10^{-5}$ is usually called high birefringent fiber, while it is called low birefringent fiber when $\Delta n < 10^{-6}$ or 10^{-7} . In fact, no optical fiber is free of birefringence. It is well-known that birefringence in optical fibers is due to the presence of asymmetric stress or geometric deformation.^{2,3} Birefringence can be present if the fiber core is not perfectly circular,

or if the fiber is bent, twisted, or under external pressure. Since linear birefringence is unavoidable in optical fibers, we should consider both linear and nonlinear birefringence when we are going to study the polarization evolution in optical fibers. It turns out that the absolute value of linear birefringence is not relevant in describing the polarization evolution in birefringent optical fibers. It is the relative strength of linear and nonlinear birefringence that is important in determining the dynamics of polarization. The power under which nonlinear birefringence is equal to linear birefringence is defined as the critical power P_{cr} . There are two extreme cases that we are interested in this chapter: (a) low birefringent. In this case, the input power $P \gg P_{cr}$, or in other words, the nonlinear birefringence dominates the linear birefringence so that the medium can be considered as a medium with negligible linear birefringence; (b) high birefringent. In this case, $P \ll P_{cr}$. The nonlinear birefringence is much smaller than the linear birefringence, the polarization dynamics is dominated by linear birefringence, the nonlinear birefringence is only a small perturbation. The reason for choosing these two extreme cases is that the polarization dynamics show much simpler behaviors than the case when the nonlinear birefringence is comparable to linear birefringence. There is an instability known as polarization instability when P is comparable to P_{cr} .⁴⁻⁶

Nonlinear birefringence or self-induced birefringence in optical Kerr media has found many applications since its discovery made by Maker et al.¹ For example, nonlinear birefringence has been used in optical shutter or optical modulators with picosecond response time,⁷ pulse shaping or intensity discrimination,⁸ optical pulse cleaning,⁹⁻¹¹ fiber-optic logic gates,^{12,13} high-resolution distributed fiber sensor,¹⁴ passive mode locking of fiber lasers.^{15 - 18} Recently, J.-L. Tanié and G. Mourou used this effect to remove the pedestal associated with the pulses compressed by a fiber-pulse compressor, and a contrast ratio as high as 10^7 was obtained.¹¹ Due to the

complication of self-focusing of intense laser beam in bulk Kerr media, which is closely related to nonlinear birefringence, most investigations have been made in single mode optical fibers.

The purpose of our work is twofold. First we want to conduct further experimental investigation of nonlinear birefringence, and find a way to optimize the nonlinear transmission in a scheme similar to Stolen et al's.⁸ Previous experimental investigation only partially confirmed the theoretic predictions of Ref. (8), it was confirmed that the nonlinear transmission increases quadratically with incident power.^{14,16} However, according to Stolen et al's theory,⁸ the nonlinear transmission is also a function of incident polarization angle with respect to the birefringent axes, and there is an optimal incident angle such that the nonlinear transmission is the largest. It is the purpose of this work to test the existence of this optimization, which will be very helpful to many other applications based on nonlinear polarization rotation. Secondly, we are also interested in looking for improved schemes of pulse cleaning based on nonlinear polarization rotation. The theory of Stolen et al⁸ is valid for high birefringent cases, it is also interesting to study the low birefringent case.

The outline of this chapter is as follows. In Sec. (3.2), we are going to study the nonlinear birefringence in the high birefringent regime. The existence of optimal nonlinear transmission, as well as the overall angular-dependence of nonlinear transmission, has been confirmed experimentally. In Sec. (3.3), a improved scheme of ultrafast pulse cleaning device based on nonlinear polarization rotation in the low birefringent regime is analyzed in detailed. Comparison between our improved scheme and that of Stolen et al's has been made, it is found that our improved scheme is much more efficient than that of Stolen et al'. Finally, we summarize our results and discussions in Sec. (3.4).

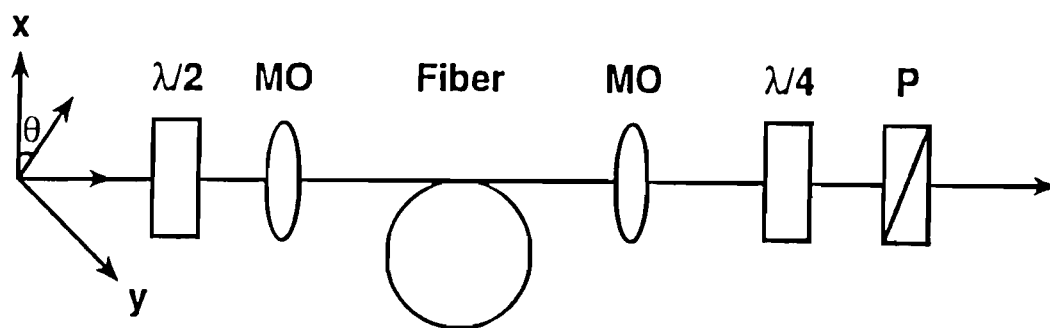


Fig. 3.1 Experimental setup. $\lambda/2$ -half wave plate; MO— $\times 10$ micro-objective; $\lambda/4$ -quarter wave plate; P-polarizer.

3.2 Nonlinear birefringence in high birefringent optical fibers

When the intensity of a light wave propagating in a birefringent optical fiber is large enough, the refractive indices of the fast and slow axes are changed by different amounts depending on the polarization direction of incident light wave. This phenomenon, referred to as nonlinear birefringence or self-induced birefringence, has many applications.

If the angle between the polarization of incident laser light and fast axis of optical fiber is not zero, the electric fields along both fast and slow axes will not be zero; therefore both components induce refractive index changes not only along its own axis but also along the other axis, that is, the refractive index change along one axis is due to both self-phase modulation and cross-phase modulation. As a consequence of this nonlinear birefringence, the polarization of the total electric field rotates, and the electric field polarization will be elliptical in general. If the linear birefringence is compensated for and a polarizer is used to block low intensity light that does not have a polarization rotation, then the transmitted light will depend on the incident power and polarization direction. Previous experiments^{14,16} only confirmed the power dependence of the transmission; discrepancies were found in the relation between transmission and input polarization. For example, when incident polarization is along one of the optical axes, there is no electric field along the other axis, thus there should be no nonlinear birefringence, hence, zero transmission. Experimental results showed that the nonlinear birefringence was not zero, and no experimental results confirmed the overall behavior of transmission with respect to the polarization direction. This discrepancy was believed to be due to the random fluctuations of the birefringent axis and the misalignment of the incident polarization angle in the experiments. An elliptical rotation of polarization due to the four-wave mixing was also considered important for low birefringent fibers.¹⁹ However, it is shown in this

paper that this discrepancy is not physical, and good agreement between theory and experiment is verified.

The experimental setup is shown in Fig. (3.1). A 50-ps Nd:YLF laser pulse ($\lambda = 1.053 \mu\text{m}$) was coupled into a 800-m single-mode optical fiber. A chirped pulse with spectrum broaden to 2.4 nm is formed due to self-phase modulation. A double-pass grating was then used to compress the chirped pulse to 1 ps before being coupled into a 3-m single-mode fiber of type FS-LB-4211 (product of 3M company) by a micro-scope objective. The core diameter of the fiber is 4 μm . Another microscope objective was used to collimate the output laser light. A quarter wave plate was used to compensate for the linear birefringence of the optical fiber. A polarizer was positioned to block the low intensity light. For high intensity light, the polarization direction of the light pulse will rotate a finite angle depending on light intensity and fiber length. Therefore, part of high intensity pulse is expected to pass through the polarizer. The transmission induced by nonlinear birefringence is given by⁸

$$T = \sin^2[\gamma P_0 L \cos(2\theta)/6] \sin^2(2\theta), \quad (3.1)$$

where P_0 is the input power and θ is the incident polarization angle with respect to the fast axis of the fiber. $\gamma = 2\pi n_2 / \lambda A_{\text{eff}}$ and A_{eff} is the effective fiber cross section. n_2 is the Kerr parameter of optical fiber. For fused silica, $n_2 = 3.2 * 10^{-16} \text{ cm}^2/\text{W}$.

In our experiment, as much as 50% of incident light was coupled into the low birefringent fiber, which gave a peak power of 150-300 W depending on the pulse width. It was not difficult to find the two optical axes. The extinction ratio was measured to be about 400. It was found that the linear birefringence fluctuates randomly for different values of θ . It is important to compensate the linear birefringence as much as possible, otherwise the transmission will suffer a large

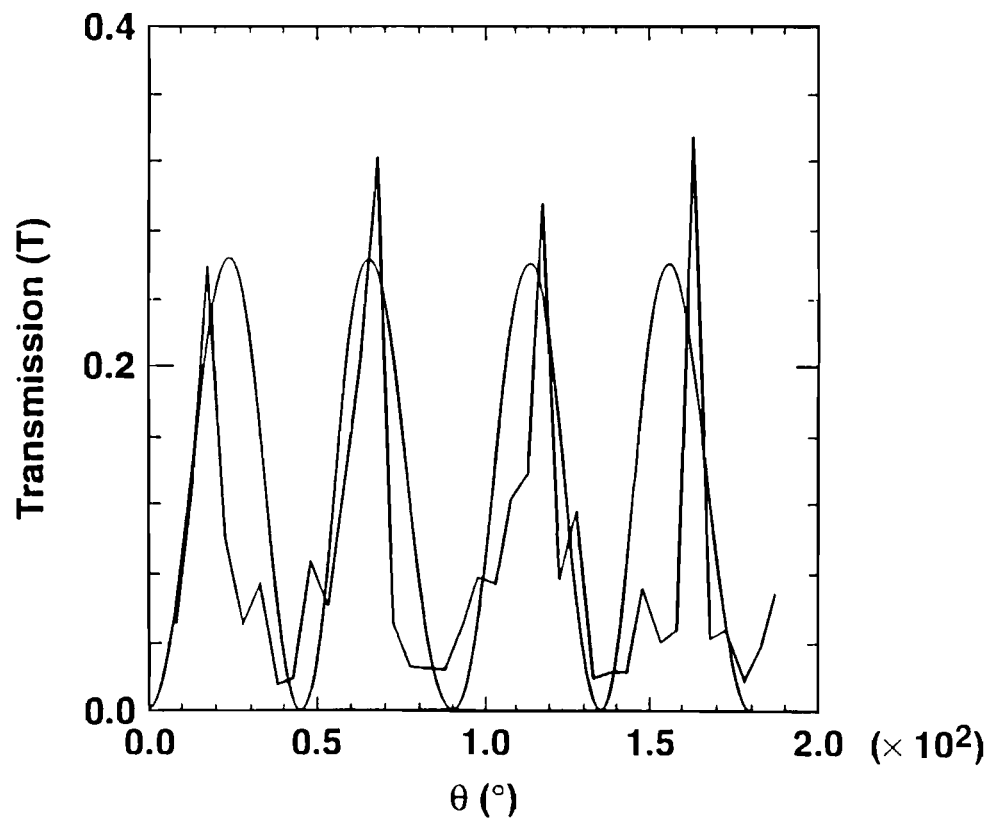


Fig. 3.2 Experimental results of nonlinear transmission for a twisted fiber. The data points are 5° apart.

deviation. Figure (3.2) shows the experimental result. The fiber was wound on a drum of a diameter of 20.5 cm with some axial twisting introduced. The vertical axis is the transmission, and the horizontal axis is the incident polarization angle θ . The smooth curve is fit using Eq. (3.1) with $P_0 = 150\text{W}$ and $L = 3\text{ m}$. It should be pointed out that the transmission T strongly depends on the optical power or $\phi_m = \gamma P_0 L$, a 50% change in ϕ_m will cause T to be three times smaller in the weak nonlinear regime studied here. Although the transmission is nonzero throughout, the overall behavior is consistent with the theory. The data points in Fig. 2 are 5° apart.

Fig. (3.3) shows the transmission with more data points (every 2° apart) and different winding. The overall behavior is the same to that of Fig. (3.2). Fig. (3.3) was obtained with the fiber loosely placed on an optical table with the bending and twisting reduced as much as possible. The main difference between Fig.(3.2) and Fig. (3.3) was the absolute values of the transmission. From the theory, the higher the nonlinearity, the larger the transmission. It was confirmed that the nonlinearity of fiber can be increased by introducing axial twisting of the fiber. The fine scale fluctuations in Fig. (3.2) and Fig. (3.3) are believed to be due to the error in adjusting the polarization angle and the incident laser power. In order to compensate the linear birefringence, we need to reduce the incident laser power to make sure that the nonlinear effect is negligible. Since both the $\lambda/2$ waveplate for the control of incident power and the $\lambda/4$ waveplate used to compensate the linear birefringence are adjusted manually, an error of a significant fraction of 1° is expected. From Eq. (3.1), an error of 5% in transmission is possible if an error of 0.5° is introduced in adjusting the polarization angle. It is found that the transmission is very sensitive to the polarization angle. It is also very difficult to compensate the linear birefringence completely due to the finite extinction ratio of the polarizer and the error in adjusting the polarization

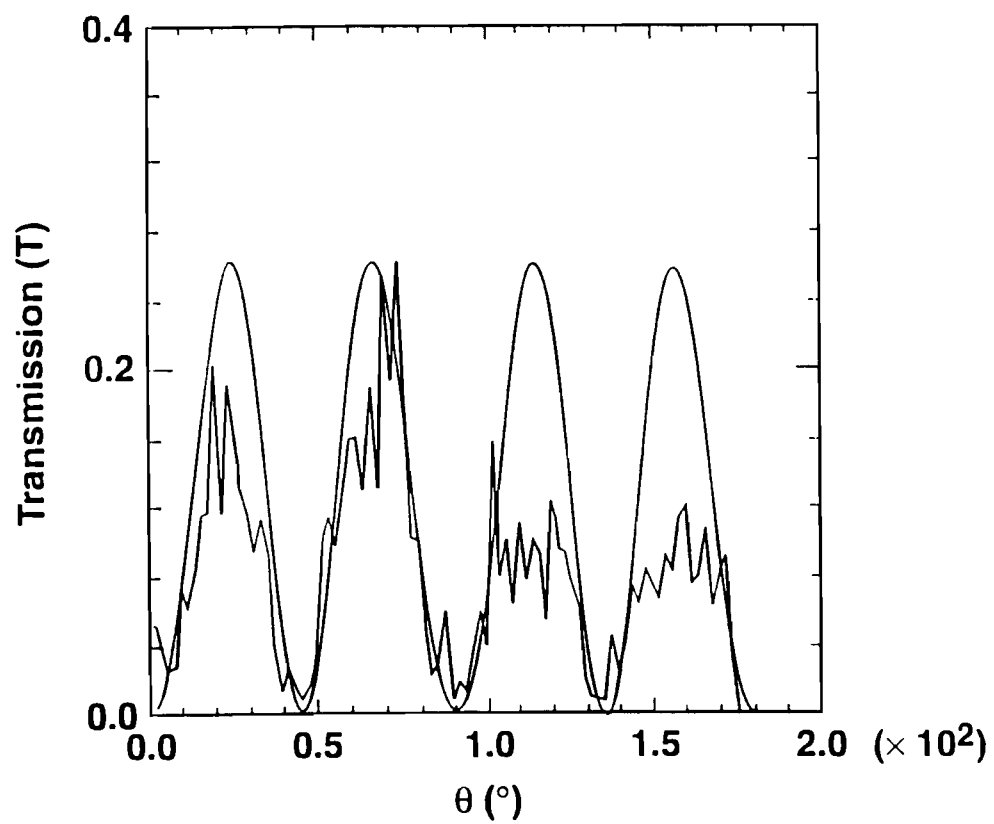


Fig. 3.3 Experimental results of nonlinear transmission for a loosely placed fiber. The data points are 2° apart. The transmission shows periodic modulations.

angle. A more precise control of the waveplate and polarizer is needed to obtain a better result with less fluctuations.

Both Fig. (3.2) and Fig. (3.3) show that the transmission is always nonzero. However, this is not considered as a large discrepancy between theory and experiment, since the overall behavior of experimental result is so close to that of theory. It is believed that the error in the compensation of the linear birefringence, the finite extinction ratio of the polarizer, and the angular misalignment of incident polarization angle could be the important reasons for the nonzero transmission at $\theta = 0^\circ, 45^\circ, 90^\circ, 135^\circ, \text{ and } 180^\circ$. It seems that nonlinear elliptical rotation is not as important as the factors mentioned above. In fact, any failure compensate the linear birefringence could destroy the observed results completely.

3.3 Nonlinear birefringence in low birefringent optical fibers

Nonlinear birefringence is also known as nonlinear polarization rotation in some of the applications mentioned above. Maker et al¹ found that the direction of the major axis of an intense, elliptically polarized laser beam will change after propagating through a nonlinear Kerr medium. The ellipticity of the polarization ellipse will not change. In order to use this self-induced modification of the polarization state, people usually place the nonlinear medium between a crossed polarizer-analyzer pair. Low intensity radiation will not transmit, while high intensity component experiences polarization rotation, part of the high intensity component transmit. In the perturbative regime, the nonlinear transmission increases quadratically with the incident peak power.⁸ Stolen worked out the theory that laid down the foundation for most practical applications.⁸ Experimental confirmation of

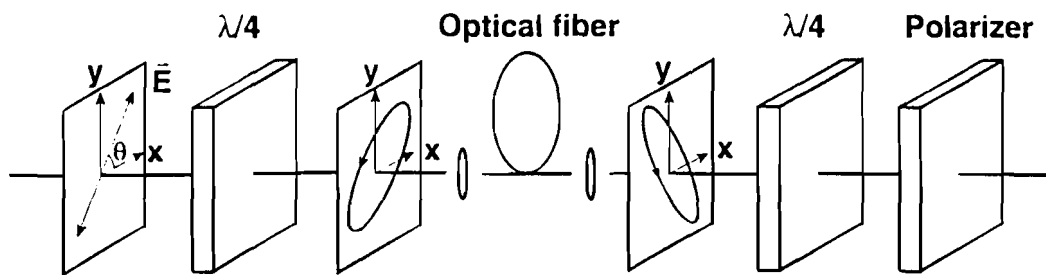


Fig. 3.4 Experimental setup. x and y are the axes of the first quarter wave plate; θ is the angle between x and the polarization vector; P-polarizer.

Stolen's theoretical predictions had been made by Nikolaus et al,¹⁴ Kitayama et al,¹⁶ and Cao and Meyerhofer.²⁰ There are two factors that prevent investigators from obtaining high values of nonlinear transmission. First most laser systems do not provide the high power required by the theory. Secondly, stimulated Raman scattering(SRS) and stimulated Brillouin scattering(SBS) will become important when the incident power is above the threshold of SRS or SBS.²¹ This power requirement has greatly limited the practical applications of nonlinear birefringence. It should be pointed out that Stolen et al's theory⁸ is valid for a birefringent medium, although his analysis did not include explicitly any parameter characterizing the linear birefringence. There has been some confusion in applying Stolen et al's ⁸ theory. Since Stolen et al ⁸ considered linearly polarized laser beams, the nonlinear transmission has been incorrectly interpreted as the polarization rotation of a linearly polarized light. Maker et al ¹ showed that there will be no polarization rotation for a linearly polarized laser beam in an isotropic Kerr medium. The fact that there still exists nonlinear transmission is due to the presence of linear birefringence, which changes the polarization state from linear to elliptical. The reason that this linear birefringence did not appear in final analysis is due to the rapid oscillation of polarization state caused by the linear birefringence. In other words, when the beat length is much shorter than the nonlinear beat length, only the average effect of linear birefringence is left. When the beat length is comparable to the nonlinear length, the interplay of linear and nonlinear birefringence has to be taken into consideration.¹⁹

It is well known that the nonlinear polarization rotation depends on not only the incident power, but also the polarization state, or the ellipticity of the incident beam. In a isotropic Kerr medium, there exist two nonlinear eigenstates of polarization, that is, linearly and circularly polarized states. In order words, there will

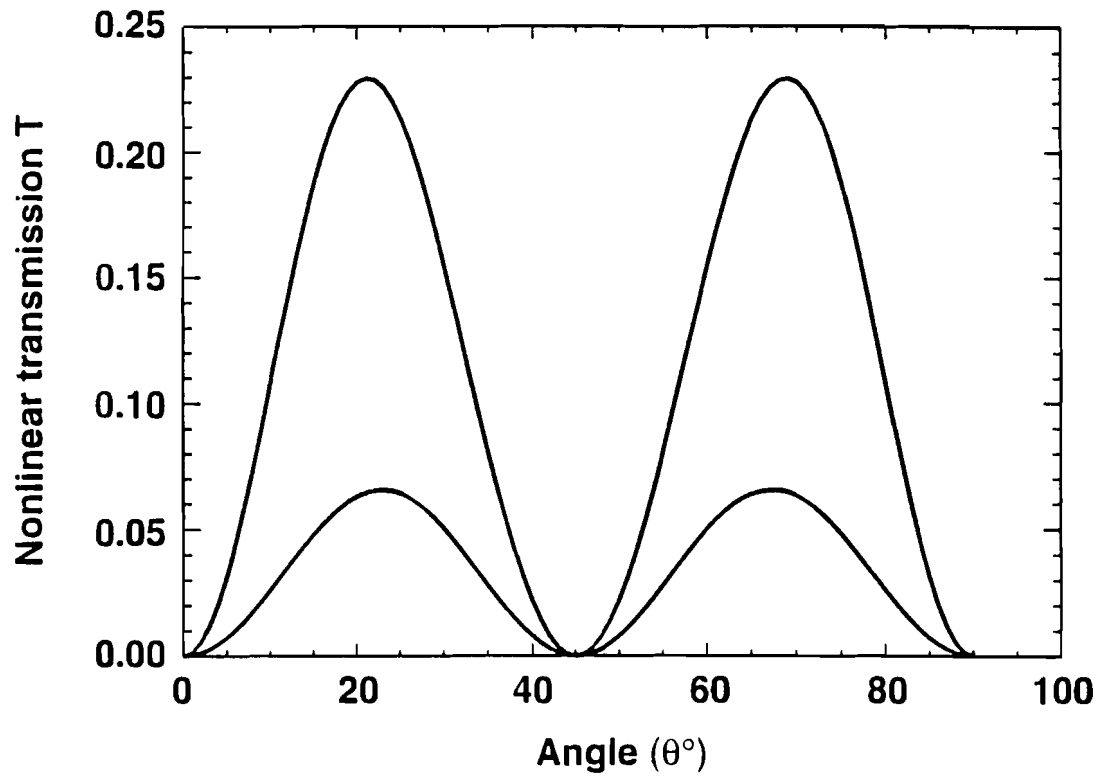


Fig. 3.5 Nonlinear transmission versus incident angle of the polarization vector; Upper curve corresponds to the improved scheme, while the lower one corresponds to the scheme of Stolen et al.⁸

be no polarization change if the incident beam is either linearly or circularly polarized. Since linearly polarized light was used in the scheme of Stolen et al,⁸ there should be no nonlinear transmission. However, as mentioned previously, the finite nonlinear transmission in the scheme of Stolen et al ⁸ is due to the presence of linear birefringence that changes the polarization state periodically from linear and circular. Since there are no nonlinear transmission for both linearly and circularly polarized light, there should be an optimal choice for the polarization state of the incident beam. It is the purpose of this work to find out this optimum polarization state that gives the largest nonlinear transmission.

In our improved scheme, the incident polarization is assumed to be elliptical in general. Since most previous applications were based on the scheme of Stolen et al,⁸ it will be helpful to make direct comparison of these two schemes. Therefore, we start with a linearly polarized light, then change the polarization to elliptical using a quarter waveplate($\lambda/4$) as shown in Fig.(3.4). An analyzer consisting of another quarter waveplate and a polarizer is placed at the exit of a nonlinear Kerr medium. The analyzer is adjusted in a way such that there will be no transmission for light with low intensity. The polarization ellipse of high intensity component will rotate an angle after passing through the nonlinear medium, which causes finite amount of nonlinear transmission. The axes of the first quarter wave plate is along x and y axis as shown. The angle between fast axis(x) and the polarization direction of the incident beam is θ . Our scheme is very similar to that of Stolen et al, ⁸ except the polarization states.

The nonlinear polarization of an isotropic Kerr medium is given by¹

$$\bar{P}^{(NL)} = A(\bar{E} \cdot \bar{E}^*)\bar{E} + \frac{1}{2}B(\bar{E} \cdot \bar{E})\bar{E}^* \quad (3.2)$$

where $A = \chi_{1122}$, $B = \chi_{1221}$. \bar{E} and \bar{E}^* are the amplitude of the electric field and its complex conjugate, respectively. For medium like fused silica, in which the nonlinearity comes from the nonresonant electronic response, $A = B$.²² $B/A = 6$ for nonlinearity of molecular orientation, $B/A = 0$ for electrostriction. Since the nonresonant electronic nonlinearity is almost instantaneous, we concentrate on this kind of nonlinearity in this work. There will be no coherent coupling terms between components of orthogonal basis if the basis are chosen to be circular polarized states. The intensity-dependent refractive indices of right- and left-hand polarized beams are given by²²

$$n_{\pm} = n_0 \pm \frac{2\pi}{n_0} \left[A |E_{\pm}|^2 + (A + B) |E_{\mp}|^2 \right] \quad (3.3)$$

where $E_{\pm} = (E_x \pm iE_y)/\sqrt{2}$ are the electric field components of right- and left-hand polarized basis. The rotation angle of the polarization ellipse equal to half the phase difference between the two components, and is given by²

$$\phi = \frac{\pi\omega}{n_0 c} L \left(|E_{-}|^2 - |E_{+}|^2 \right) \quad (3.4)$$

where n_0 is the linear refractive index of optical fiber, ω is the frequency of incident laser. L is the length of the nonlinear medium. It is straightforward to calculate the nonlinear transmission due to the rotation of the polarization ellipse, and it is given by

$$T = \cos^2(2\theta) \sin^2[\phi_{\text{spm}} \sin(2\theta)/3], \quad (3.5)$$

where $\phi_{\text{spm}} = \gamma P_0 L$ is the self-phase modulation of a linearly polarized beam with equal amount of power or intensity, P_0 is the input power, $\gamma = 6\pi^2 \omega A_{\text{eff}} / n_0 c$ and A_{eff} is the effective fiber cross section. The dependence of nonlinear transmission of both schemes on the incidence polarization angle are plotted in Fig. (3.5) for $\phi_{\text{spm}} = \pi$. The peak values of the nonlinear transmission are functions of incident angle of polarization direction and power. The upper curve is obtained from Eq. (3.5), while the lower one is from Eq. (3.1). It is obvious that our improved scheme provides a much larger transmission. The peak transmission of Stolen et al is about 6.5% for $\phi_{\text{spm}} = \pi$, while it reaches 24% in the improved scheme. The peak nonlinear transmission as a function of incident power or ϕ_{spm} are plotted in Fig. (3.6). Again, the upper curve is obtained from Eq. (3.5), while the lower one corresponds to Eq. (3.1). When $\phi_{\text{spm}} = 2\pi$, the corresponding peak transmissions are 57% and 23% respectively; When $\phi_{\text{spm}} = 3\pi$, the peak transmission our improved scheme approaches 78%, showing the characteristics of saturation, while the peak transmission of the scheme of Stolen et al is about 42%. The gain in the nonlinear transmission of our improved scheme is tremendous, which is expected to reduce the power requirement in many applications significantly.

Since the polarization ellipticity is related to θ by $e = \tan(\theta)$ when $0 < \theta < \pi/4$, $e = \cotan(\theta)$ when $\pi/4 < \theta < \pi/2$. Fig. (3.4) also shows the dependence of nonlinear transmission on the incident ellipticity e . The transmission curve is mirror-symmetric around $\theta = 45^\circ$, we concentrate on the first half of the transmission curve, or $0 < \theta < \pi/4$. As θ increases from 0 to 45° , the ellipticity e also increases from 0 to 1. Fig. (3.4) shows that there is an optimal value of ellipticity such that the nonlinear transmission is the largest. It turns out that this optimal ellipticity e_{opt} depends on the incident power. Fig. (3.7) shows the variation of e_{opt} for different incident power indicated by

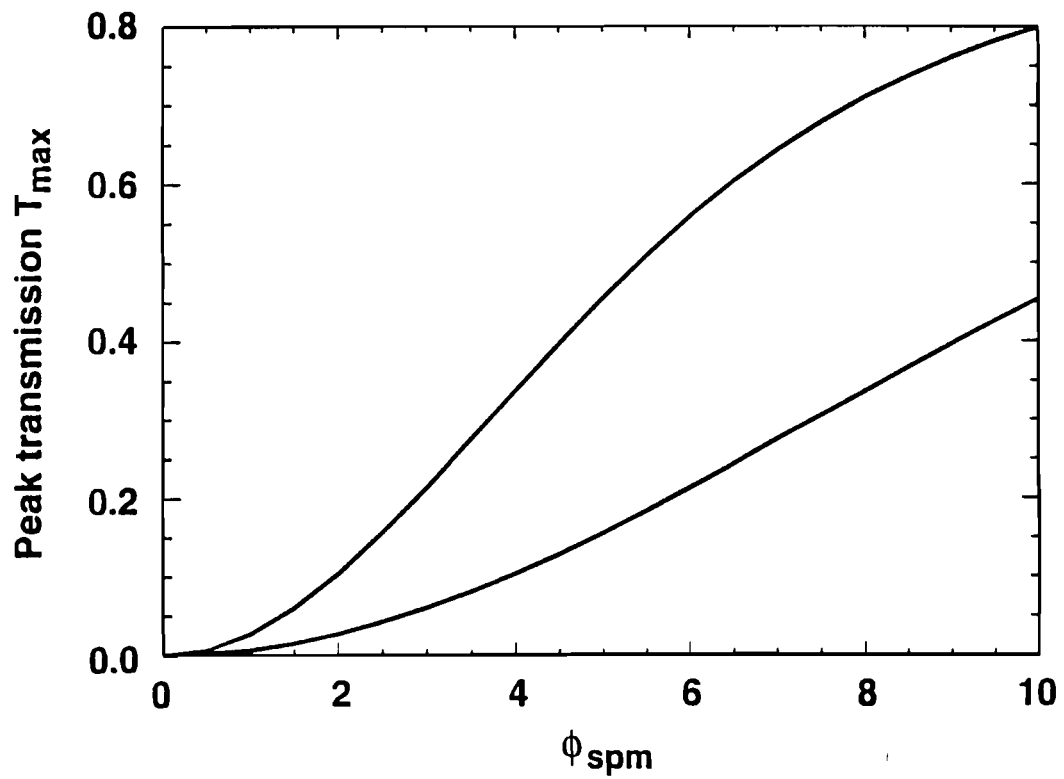


Fig. 3.6 Peak nonlinear transmission versus incident power. Upper curve corresponds to the improved scheme, while the lower one corresponds to the scheme of Stolen et al.⁸

ϕ_{spm} . At low power level, $\phi_{\text{spm}} < \pi$, e_{opt} is approximately 0.414, corresponding an incident angle $\theta = \pi/8$. At high power level, $\phi_{\text{spm}} \gg \pi$, e_{opt} approaches a constant of 0.057, corresponding $\theta = 3.3^\circ$. The higher the input power, the smaller the optimal ellipticity, and thus the smaller the incident polarization angle. It should be mentioned that the nonlinear transmission T is a periodic function of ϕ_{spm} , therefore there are multiple peaks in the transmission curve. Correspondingly, there are multiple optimal values of e_{opt} when $\phi_{\text{spm}} \gg \pi$. As long as ϕ_{spm} is less than 40, the optimal ellipticity e_{opt} in Fig. (3.7) still corresponds to the highest transmission, although it is possible that other peaks are comparable to this one. Therefore, the regime of $\pi/8 < \theta < 3\pi/8$ or $0.414 < e < 1$ should always be avoided in order to obtain higher transmission.

3.4 Conclusion

In conclusion, the nonlinear birefringence of low birefringent fiber has been studied experimentally. It is found that the earlier discrepancies between experimental results and theory could be due to the failure to compensate the linear birefringence, and the experimental results obtained in this paper are consistent with theory. It should be mentioned that the dependence of nonlinear transmission on the polarization angle could be used to optimize the nonlinear transmission in pulse shaping, optical switching, and other applications as well. A improved scheme of pulse shaping using nonlinear transmission has been analyzed in detail. It is found that the nonlinear transmission of this improved scheme is much larger than that of previous scheme. The peak transmission can be increased more than three times, from 7% to 24% for a incident power that is equivalent to that of generating a self-phase modulation of π . For $\phi_{\text{spm}} = 2\pi$, the gain in nonlinear transmission is about 2.5 times, corresponding an increase from 23% to 57%. For high power, the gain becomes

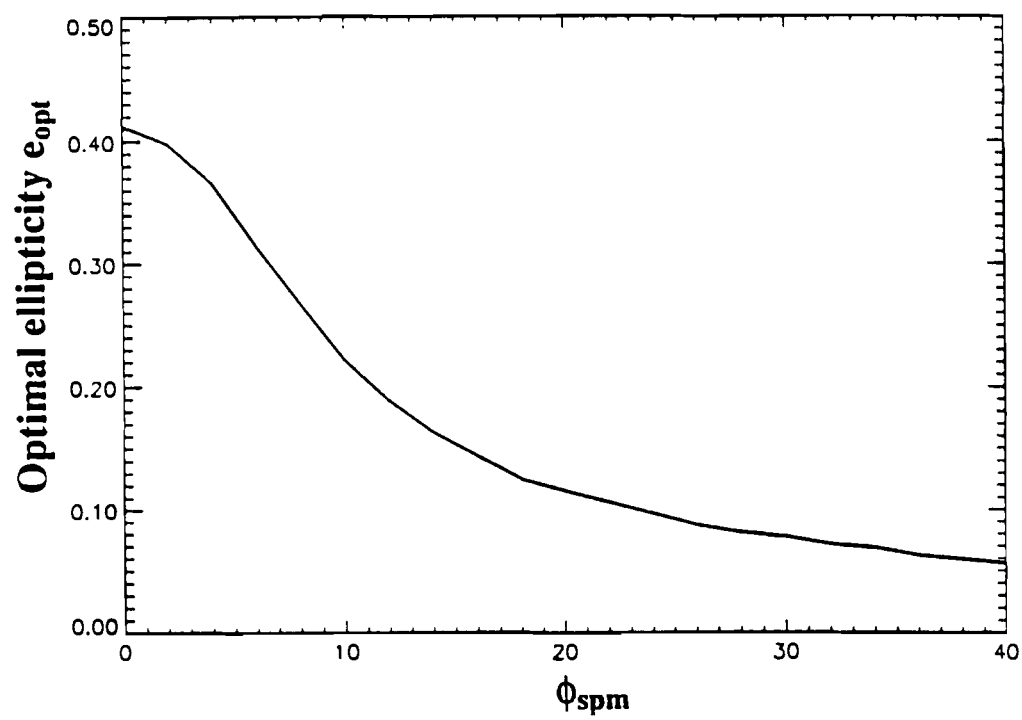


Fig. 3.7 Optimal polarization ellipticity e_{opt} versus incident power measured by ϕ_{spm} .

saturated. Since stimulated Raman and Brillouin scattering limit the power level that can be used, this improved scheme will be very useful for many applications involving moderate power levels. For the same power as used in Fig. (3.3), the nonlinear transmission can be increased from 20% to nearly 60% by using our improved scheme. Similar improvement can be obtained in the pulse shaping experiment of Tapié and Mourou.¹¹ As for the pulse shaping experiment, our improved scheme has two advantages compared to that of Ref.(11). First, the enhanced nonlinear transmission will provide a better contrast. Second, there is no need to compensate for the linear birefringence in our improved scheme, which strongly affects the contrast in the scheme of Tapié and Mourou¹¹ It is found that there is a optimal polarization ellipticity for the maximum nonlinear transmission. The value of e_{opt} depends on the incident power. It is also found that the polarization ellipticity should always kept smaller than 0.414 so that higher nonlinear transmission can be obtained. For high power, the gain becomes saturated. Since stimulated Raman and Brillouin scattering limit the power level that can be used, this improved scheme will be very useful for many applications involving moderate power levels.

REFERENCES

1. P. D. Maker, R. W. Terhune, and C. M. Savage, *Phys. Rev. Lett.* **12**, 507(1964).
2. R. H. Stolen, W. Pleibel, and J. R. Simpson, *IEEE J. Lightwave Technol.* **LT-2**, 639 (1984).
3. S. C. Rashleigh and M. J. Marrone, *IEEE J. Quantum Electron.* **RE-18**, 1515 (1982).
4. B. Daino, G. Gregori, and S. Wabnitz, *J. Appl. Phys.* **58**, 4512(1985); *Opt. Lett.* **11**, 42 (1986).
5. H. G. Winful, *Opt. Lett.* **11**, 33 (1986).
6. G. Gregori and S. Wabnitz, *Phys. Rev. Lett.* **56**, 600 (1986).
7. M. A. Duguay, in *Progress in Optics*, edited by E. Wolf (North-Holland, Amsterdam, 1976), Vol. 14, p. 163.
8. R. H. Stolen, J. Botineau, and A. Ashkin, *Opt. Lett.* **7**, 512 (1982).
9. B. Nikolaus, D. Grischkowsky, and A. C. Balant, *Opt. Lett.* **8**, 189 (1983).
10. N. J. Halas and D. Grischkowsky, *Appl. Phys. Lett.* **48**, 823 (1986).
11. J.-L. Tapié and G. Mourou, *Opt. Lett.* **17**, 136 (1992).
12. K. Kitayama, Y. Kimura, and S. Seikai, *Appl. Phys. Lett.* **46**, 317 (1985).
13. Y. Kimura, K.-I. Kitayama, N. Shibata, and S. Seikai, *Electron. Lett.* **22**, 277 (1986).
14. W. Zhao and E. Bourkoff, *IEEE J. Quantum Electron.* **29**, 2198 (1993).
15. M. Hofer, M. E. Fermann, F. Haberl, M. H. Ober, and A. J. Schmidt, *Opt. Lett.* **16**, 502 (1991).
16. D. U. Noske, N. Pandit, and J. R. Taylor, *Electrpn. Lett.* **28**, 2185 (1992).

17. K. Tamura, E. P. Ippen, H. A. Haus, and L. E. Nelson, *Opt. Lett.* **18**, 1080 (1993).
18. H. A. Haus, E. P. Ippen, and K. Tamura, *IEEE J. Quantum Electron.* **30**, 200(1994).
19. H. G. Winful, *Appl. Phys. Lett.* **47**, 213 (1985).
20. X. D. Cao and D. D. Meyerhofer, *Opt. Commun.* **109**, 151(1994).
21. G. P. Agrawal, *Nonlinear Fiber Optics*, (Academic Press, Boston, 1989).
22. R. W. Boyd, *Nonlinear Optics*, (Academic Press, Boston, 1992).

CHAPTER 4

Soliton Stability and Soliton Collisions in Birefringent Optical Fibers

In previous chapters, we have studied the effects of linear and nonlinear birefringence on the propagation of short pulses. Linear birefringence or polarization mode dispersion (PMD) causes a short pulse to split into two components. However, we neglected the effects of the group velocity dispersion (GVD) in chapters 2 and 3. In this chapter, we study the nonlinear propagation of short pulses in optical fibers when linear birefringence, nonlinear birefringence (or nonlinear refraction), and GVD are important. The combination of nonlinear refraction and GVD gives rise to a very important phenomenon, that is, optical solitons. Linear birefringence can destroy the soliton propagation since it causes a short pulse to split.

In this chapter, we study the effects of linear birefringence on soliton stability and collisions. Several conservation laws are found and used to determine a one-parameter family of solitary-wave solutions. Soliton stability is discussed quantitatively using a virial theorem. By analyzing the virial theorem, we obtain the relationship between the threshold amplitude and the linear birefringence. Our analytic result agrees well with numerical simulations.

The effects of linear birefringence on the collisions of solitons are studied numerically. It is found that there are three regions of interaction in the parameter space of linear birefringence. It has been shown that the governing equations for the temporal solitons in a birefringent optical fiber are mathematically equivalent to those for vector spatial solitons. The collisions of vector spatial solitons is investigated numerically. The applications of spatial vector solitons in all-optical switching are investigated numerically.

4.1 Introduction

In most discussions of optical solitons, it is assumed that the input pulses are linearly polarized, and remain so throughout their propagation. The state of polarization plays no role in the nonlinear propagation.^{1,2} However, there are more general situations in which the state of polarization is important. For example, when optical pulses or beams are elliptically polarized, we know from chapter 3 that nonlinear refraction can result in polarization rotation if the light is elliptically polarized. Therefore, the electric field amplitude can't be described by a single field component, and a vector description is required. The corresponding solitons are referred to as vector solitons to emphasize the fact that an input pulse maintains not only its intensity profile but also its state of polarization.³ Vector solitons are fundamentally different from the usual scalar solitons, they possess many new properties that can't be found in scalar solitons. It is these new properties that make vector solitons have more potential applications than scalar solitons.

There are two kinds of optical solitons, that is, temporal and spatial solitons. Temporal solitons are nonlinear pulses that can maintain their pulse shape or width without distortion during their propagation, while spatial solitons are light beams that can maintain their beam shapes or sizes without broadening. In a waveguide such as an optical fiber, the spatial intensity profile is fixed and only the pulse width is allowed to change due to chromatic and polarization dispersions. In such cases, we can have temporal solitons if self-phase modulation (SPM) or cross-phase modulation (XPM) can negate the effect of linear dispersion. As for the propagation of CW laser beams in planar waveguides, there is no temporal variation, but the beam size is allowed to change with distance under the effect of diffraction. In such cases, spatial solitons are possible if nonlinear refraction can cancel diffraction so that the beams can propagate

without changing their sizes. Both spatial and temporal solitons can be either scalar or vector solitons depending on whether the polarization of the light field comes into play. It should be emphasized that temporal solitons are more likely to be vector solitons in optical fibers due to the presence of the residual birefringence which causes the polarization to evolve periodically. Since most optical solitons are realized in optical fibers, the effect of birefringence on temporal solitons is becoming a very important issue. These effects include the issue of soliton stability and soliton collisions. In other words, it is interesting to know whether solitons can survive the influence of birefringence, and how birefringence affects the soliton collisions. Although the same questions can also be asked for spatial solitons, the effect of birefringence in planar waveguides is not as important as in optical fibers. However, it was found that the role of birefringence in temporal solitons is replaced by another parameter in spatial solitons, that is, the intersection angle between two vector soliton beams. Interestingly, the spatial and temporal solitons are mathematically equivalent if the term describing birefringence in temporal solitons interchanged with the intersection angle in spatial solitons. This makes it possible to study both spatial and temporal solitons using the same governing equations, and the spatial-temporal analogy is very helpful in understanding the underlying physics. In this chapter, we study the stability and collisions of vector solitons in a unified way so that the results are applicable to both spatial and temporal solitons.

The organization of this chapter is as follows. We discuss the soliton stability in Section 4.2, collisions of temporal vector solitons in Section 4.3 and collisions of spatial vector solitons in Section 4.4. The results are summarized in Section 4.5.

4.2 Stability of vector solitons in birefringent optical fibers

Optical solitons are nonlinear pulses that propagate without distortion and can be described by a nonlinear Schrödinger equation (NSE)⁴ for the wave amplitude. Bright solitons in optical fibers were first observed more than ten years ago.^{5,6} Soliton-based communication systems have a tremendous information handling capacity compared with even the most advanced conventional optical systems.⁴ However, solitons suffer from mutual interactions, or collisions, since the same Kerr nonlinearity used to compensate for dispersion also results in interactions among neighboring solitons. This kind of collision limits the bit rate of soliton-based communication systems. Soliton collisions in lossless fibers have been studied both theoretically and experimentally;^{2,7} both attractive and repulsive interaction forces were found. To avoid such interactions, the distance between solitons has to be sufficiently large, usually ten times larger than the pulse width. This requirement significantly limits the achievable transmission rate.

Another important factor which affects soliton propagation is the optical birefringence.^{8,9} The work described above rests on the assumption that single-mode fibers contain only one propagating mode. However, single-mode fibers are really bimodal because of the presence of optical birefringence. These two modes are orthogonally polarized and propagate with different group velocities. When the birefringence is weak, its main effect is the polarization instability, since the critical power for the polarization instability is quite small for weak birefringence.¹⁰ However, birefringence is usually not weak in optical fibers.^{8,9} The resulting difference in group velocities leads to pulse splitting, which is undesirable in communication applications. Just as the Kerr nonlinearity can be used to compensate for linear dispersion and generate solitons,⁴ Menyuk⁸ showed that the same nonlinearity can also negate the walk-off effect and entrain the solitons. He found that the threshold amplitude for

mutually trapped solitons increases with increasing birefringence; solitary light pulses can still be obtained providing their amplitudes exceed this threshold. Using a pseudo-particle model, Caglioti, Crosignani and Di Porto showed that the threshold amplitude depends quadratically on the linear birefringence.¹¹ Based on the model and the numerical results of Menyuk⁸, Kivshar¹² predicted that the threshold amplitude depends linearly on the linear birefringence. The method used by Kivshar is the reduced variational method (RVM) developed by Anderson, Bondeson, and Lisak.¹³⁻¹⁵ In fact, these authors had considered the same model and had obtained a similar potential form.¹⁵ They also pointed out that the perturbed Lagrangean formalism is only valid when the separation between the partial solitons and the birefringence are both relatively small. Our computer simulation shows that the threshold amplitude tends to a finite value as the linear birefringence approaches zero. Kivshar¹² correctly predicted the existence of this gap, while the result of Caglioti, Crosignani and Di Porto¹¹ has no such gap.

In this section, the virial theorem is used to study soliton collisions in birefringent optical fibers. Zakharov, Sobolev, and Synakh¹⁶ were the first to apply the virial theorem of Vlasov, Petrishchev and Talanov¹⁷ to the nonlinear Schrödinger equation. Subsequently, a remarkable analogy has been found between the behavior of NSE and the N-body problem in celestial mechanics.¹⁸ The virial theorem was first extended to coupled NSE's by McKinstrie and Russell.¹⁹ A closely related method is the reduced variational method.¹⁵ The method of Caglioti, Crosignani and Di Porto¹¹ is closer to the RVM than to the virial theory. In this section, an equation governing the behavior of the partial solitons is derived. It is found that the amplitudes of the symmetric partial pulses and their initial separation are both critical factors in the wave evolution. Below threshold, the partial solitons will eventually separate; no mutual trapping exists. Above threshold, trapped states exist in which the partial pulses

oscillate around a common center and which can therefore be regarded as quasi-solitons. Unlike the case of a single NSE mentioned earlier, the interaction force does not depend on the relative phase between the partial pulses. The threshold amplitude is found to depend nonlinearly on the birefringence, not linearly as predicted by Kivshar.¹² The predictions of this section show a better agreement with the numerical results of Menyuk⁸ than do those of Kivshar.¹² The numerical simulations of Menyuk⁸ have been supplemented to show the dependence of threshold amplitude on the birefringence more clearly and to confirm the presence of the gap.

4.2.1 Derivation of the Virial theorem

Pulse propagation in a birefringent optical fiber is described by the coupled NSE's^{8,9}

$$i(\partial_t + \delta\partial_x) A_1 + \frac{1}{2}\partial_{xx}^2 A_1 + (|A_1|^2 + \epsilon|A_2|^2) A_1 = 0, \quad (4.11)$$

$$i(\partial_t - \delta\partial_x) A_2 + \frac{1}{2}\partial_{xx}^2 A_2 + (|A_2|^2 + \epsilon|A_1|^2) A_2 = 0, \quad (4.2)$$

where $\partial_t = \partial/\partial t$, $\partial_x = \partial/\partial x$. A_1 and A_2 are the amplitudes of the two polarization components of the waves. The normalized strength of linear birefringence is denoted by δ and is given by $1/2 (V_{g1}^{-1} - V_g^{-1})T_0/Z_d$, where $V_{g1,2}$ are the group velocities of the fast and slow modes, respectively; T_0 is normalization time and is equal to $0.568 T_{FWHM}$ of the soliton pulse; Z_d is the dispersion distance T_0^2/β_2 , used for spatial normalization; and $\beta_2 = (d^2k/d\omega^2)$ is the GVD parameter. The relation between δ and the linear birefringence Δn is $\delta = \Delta n T_0 / (2c Z_d)$, where c is the speed of light in vacuum. In Eqs. (4.1) and (4-2), t is the distance along the fiber, and x is the local time in a

frame moving with the average velocity of the fast mode and the slow mode. The parameter ϵ describes the strength of XPM relative to SPM.^{8,9} For birefringent fibers with linearly polarized eigenmodes $\epsilon = 2/3$, whereas for circularly polarized modes, $\epsilon = 2$; with elliptically polarized eigenmodes, $2/3 < \epsilon < 2$. In this chapter the fiber modes are assumed to be linearly polarized, so $\epsilon = 2/3$. In Eqs.(4.1) and (4.2), the roles of t and x are interchanged relative to Ref. 8. This interchange facilitates comparisons with the related problem of the nonlinear focusing of two light waves intersecting at a finite angle,²¹ in which 2δ is the approach velocity of the waves and one-dimensional dispersion is replaced by two-dimensional diffraction. We will discuss this issue in detail in Section 4. 4 when discussing spatial vector solitons. The four-wave-mixing terms in Eqs. (4.1) and (4.2) have been neglected since they are highly oscillating terms in most practical situations.^{8,9}

The spatio-temporal evolution of the wave amplitudes is governed by the Lagrangean density^{15,19}

$$L = \frac{1}{2}i \left(A_\alpha^* \partial_t A_\alpha - A_\alpha \partial_t A_\alpha^* \right) + \frac{1}{2} \delta_\alpha \left(A_\alpha^* \partial_x A_\alpha - A_\alpha \partial_x A_\alpha^* \right) - \frac{1}{2} \left(\partial_x A_\alpha^* \right) \left(\partial_x A_\alpha \right) + Q, \quad (4.3)$$

where A_α and A_α^* are the canonical variables, and the potential Q is given by

$$Q = \frac{1}{2} |A_1|^4 + \frac{1}{2} |A_2|^4 + \epsilon |A_1|^2 |A_2|^2. \quad (4.4)$$

Summation over repeated indices in Eq. (4.3) is implied.

Application of the Euler-Lagrangean equations

$$\frac{\partial}{\partial t} \frac{\partial L}{\partial(\partial A_\alpha / \partial t)} + \frac{\partial}{\partial x} \frac{\partial L}{\partial(\partial A_\alpha / \partial x)} - \frac{\partial L}{\partial A_\alpha} = 0 \quad (4.5)$$

to the Lagrangean generates the coupled NSE's (4.1) and (4.2).

Since Q is real, no energy is exchanged between the two waves. Thus, each wave action

$$N_\alpha = \int |A_\alpha|^2 dx \quad (4.6)$$

is conserved. Additional conservation laws can be deduced from the momentum-energy tensor^{19,22}

$$T_\nu^\mu = A_{\alpha,\nu} \left[\frac{\partial L}{\partial A_{\alpha,\mu}} \right] + A_{\alpha,\nu}^* \left[\frac{\partial L}{\partial A_{\alpha,\mu}^*} \right] - \xi_\nu^\mu L, \quad (4.7)$$

where the subscripts μ and ν denote $\delta/\delta x^\mu$ and $\delta/\delta x^\nu$, respectively. In our case here $x^0 = t$, $x^1 = x$. The momentum-energy conservation equation is

$$\partial_\mu T_\nu^\mu = -\partial_\nu L. \quad (4.8)$$

If L doesn't depend explicitly on t , and x , then the following two quantities are conserved:

(a) The total wave momentum

$$\begin{aligned} P &= \int T_n^0 dx \\ &= \int \frac{1}{2i} \left(A_\alpha^* \partial_x A_\alpha - A_\alpha \partial_x A_\alpha^* \right) dx. \end{aligned} \quad (4.9)$$

(b) The total wave energy

$$\begin{aligned}
H &= \int T_0^0 dx \\
&= -\delta_\alpha P_\alpha + \int \left[\frac{1}{2} |\partial_x A_\alpha|^2 - Q \right] dx,
\end{aligned} \tag{4.10}$$

where $\delta_1 = \delta$, and $\delta_2 = -\delta$.

In the moment approach,¹⁶ the average value of a physical quantity F is defined by

$$\langle F \rangle = \frac{\int |A_\alpha|^2 F dx}{\int |A_\alpha|^2 dx} . \tag{4.11}$$

Of particular interest here is the pulse separation

$$\langle \delta x^2 \rangle = \langle x^2 \rangle - \langle x \rangle^2 . \tag{4.12}$$

It is easy to show that

$$d_{tt}^2 \langle \delta x^2 \rangle = d_{tt}^2 \langle x^2 \rangle - 2 [d_t \langle x \rangle]^2 - 2 \langle x \rangle d_{tt}^2 \langle x \rangle . \tag{4.13}$$

where $d_t = d/dt$ and $d_{tt} = d^2/dt^2$. The quantities of interest, $\langle x \rangle$ and $\langle x^2 \rangle$, are the first and second moments of the wave action. The general idea of the moment approach is to use the conservation laws (4.8) to integrate the moments by parts and relate them to the known constants N , P , and H . For example,

$$\begin{aligned}
N d_t \langle x \rangle &= d_t \int x |A_\alpha|^2 dx \\
&= \int x \partial_t |A_\alpha|^2 dx \\
&= N_\alpha \delta_\alpha + P
\end{aligned} \tag{4.14}$$

Thus, the second term in Eq. (4.13) is a constant of the motion, and the third term is equal to zero. Although the algebra is lengthy, the first term in Eq. (4.13) can be evaluated in a similar fashion. The result is

$$d_{tt}^2 \langle \delta x^2 \rangle = \frac{4}{N} \left[H + \frac{1}{2} N_\alpha \delta_\alpha^2 + \frac{1}{2} R - \frac{1}{2} N \left(\frac{P + N_\alpha \delta_\alpha}{N} \right)^2 \right], \quad (4.15)$$

where all terms on the right-hand side are constants except the remainder term

$$R = \int Q \, dx \quad . \quad (4.16)$$

Equation (4.15) is called the virial theorem and is exact. For the special case in which birefringence is absent, Eq. (4.15) reduces to the virial equation of McKinstrie and Russell.¹⁹

If the polarization of incident wave is aligned to one of the birefringent axes, or, in other words, only a single mode is present, one can choose a new reference frame that moves with the group velocity of the wave. The virial equation can then be recast as

$$N d_{tt}^2 \langle \delta x^2 \rangle = 4T + 2V, \quad (4.17)$$

where $T = \int \frac{1}{2} |\partial_x A|^2 \, dx$ is the kinetic energy and $V = -\int Q \, dx$ is the potential energy.

For soliton solutions, one obtains

$$d_{tt}^2 \langle \delta x^2 \rangle = 0. \quad (4.18)$$

It is found that

$$T + \frac{1}{2} V = 0. \quad (4.19)$$

Written in full, Eq. (4.19) becomes

$$F\{A\} = T + \frac{1}{2} V = \int \left[\frac{1}{2} |\partial_x A|^2 - \frac{1}{4} |A|^4 \right] dx = 0. \quad (4.20)$$

Equation (4.20) is a necessary condition for a soliton solution, since we have other conservation laws which impose other constraints on the solutions. In the classical N-body problem, the virial theory of Eq. (4.19) represents a circular orbit around the center of the mass, and the soliton solutions of the NSE correspond to the stationary trapped orbits of the classical N-body problem.¹⁸ In Ref. 18, the authors showed that in higher dimensional cases ($D > 1$), the collapse of nonlinear light waves is analogous to the gravitational collapse; both phenomena have the same collapse criteria and behavior of the singularity.

4.2.2 Solitary-Wave solutions

A solitary-wave solution has been given by Kivshar¹² when there is no linear birefringence. Based on Kivshar's solution, a one-parameter family of solitary-wave solutions of Eqs. (4.1) and (4.2) is given by

$$A_j = \frac{A}{\sqrt{1+\epsilon}} \frac{\exp(ik_j x - i\omega_j t)}{\cosh[A(x - vt)]}, \quad (4.21)$$

where v is the difference between the solitary-wave velocity and the carrier-wave group velocity, A is the solitary-wave amplitude, $\omega_j = (v^2 - A^2)/2$, $k_1 = v$, and $k_2 = v$.

One way to determine a solitary-wave solution to Eqs. (4.1) and (4.2) when the linear birefringence is not zero is to use an ansatz with several free parameters, which can be chosen to satisfy Eqs. (4.1) and (4.2). In general, the correct relation between the free parameters is not obvious. A key part of this procedure is the ansatz. Since the effect of birefringence is to change the linear dispersion characteristics of each mode, one might suspect that Eq. (4.21) will be a solitary-wave solution of Eqs. (4.1) and (4.2), even in the presence of birefringence, if it is modified to allowed for additional shifts in the mode frequencies and wave numbers. There are several conserved quantities associated with Eqs. (4.1) and (4.2), as was shown above. The wavenumber shift of each partial wave is proportional to the momentum carried by the wave, so the momentum conservation law limits the wave-number shift of each wave in such a way that the total shift of both waves is a constant. A straightforward way to determine the free parameters in the ansatz of Eq. (4.21) is to substitute Eq. (4.21) directly into Eqs. (4.1) and (4.2). It is easy to show that $k_1 = -\delta + v$, $k_2 = \delta + v$, and $\omega_1 = \omega_2 = (v^2 - \delta^2 - A^2)/2$. Putting these results together gives

$$A_{1,2} = \frac{A}{\sqrt{1+\epsilon}} \frac{\exp\left[i(\mp\delta + v)x + i(A^2 - v^2 + \delta^2)t/2\right]}{\cosh[A(x - vt)]}. \quad (4.22)$$

Equation (4.21) can be anticipated on purely physical grounds. The linear propagation characteristics of each mode stem from a dispersion relation of the form

$$\omega = \pm\delta k + \frac{1}{2}k^2, \quad (4.23)$$

for which the associated group velocity

$$\frac{d\omega}{dk} = \pm\delta + k. \quad (4.24)$$

Suppose first that $v = 0$. The original solitary-wave ansatz (4.21) has an average wave number of zero, for which the group velocities are δ and $-\delta$, respectively. If the average mode wave numbers were shifted by $-\delta$ and δ correspondingly, the new group velocities would both be equal to zero. Correspondingly, both modes would acquire a frequency shift of $-\delta^2/2$, as found in solution (4.22). Since this physical mechanism relies solely on GVD, coupled solitary waves of arbitrary amplitude exist. Now suppose that $v \neq 0$. At first glance, Equation (4.22) appears to represent two light pulses traveling at some velocity other than the linear group velocity of their carrier waves. Interest in the general issue of nonlinear group velocity has been rekindled recently by Mori et al.²³ However, consideration of the frequency (ω) and wave number (k) shifts associated with finite v shows that the total solitary-wave velocity ($v_0 + v$) is equal to the linear group velocity $d\omega/dk$ evaluated at $(\omega_0 + v^2, k_0 + v)$. In other words, changing the parameter v corresponds to making the SVEA, on which the coupled NSE's are based, relative to a different carrier frequency and wavelength.³⁷ A specific solution, in which $A = 1$ and $v = 0$, was obtained by Menyuk,⁹ who explained the physical significance of his solution in a later paper.²⁰ Some analytical solutions of coupled NSE's were also found independently by Murawski.²⁴ and by Tratnik and Sipe,²⁵ and many others.

4.2.3 Relationship Between Threshold Amplitude and Birefringence

In Sec. 4.2.2, it was found that solitary waves exist when both partial waves have the same pulse shape, and overlap exactly in time. However, it is well known that

each partial wave can separate a small distance and form a quasi-stable state.^{8,9} In this section, the virial theorem is used to study the trapping behavior for arbitrary pulse shape and separation.

The threshold behavior can be obtained by analyzing Eq. (4.15). The only term that changes is R ; all the other terms are either constants of motion or free parameters. From Eq. (4.15) and Eq. (4.4), we obtain

$$R = \int \left[\frac{1}{2} |A_1|^4 + \frac{1}{2} |A_2|^4 + \varepsilon |A_1|^2 |A_2|^2 \right] dx. \quad (4.25)$$

If the right hand side Eq. (4.15) is negative, then $\langle \delta x^2 \rangle$ will be bounded; thus we have a bound state, or trapping state. We know that the energy of each pulse is conserved, the interaction between each pulse only changes the pulse phase and pulse shape, a well-known result for XPM. The magnitude of R increases when the relative distance between the two pulses decreases. When the two pulses are well separated, we have

$$R = \int \left[\frac{1}{2} |A_1|^4 + \frac{1}{2} |A_2|^4 \right] dx. \quad (4.26)$$

Under this condition, if the RHS of Eq. (4.15) is positive, then the two pulses will pass through each other and go to the infinity. On the other hand, if the RHS of Eq. (4.15) is negative, the two pulses will attract each other and form a mutual trapping state. Therefore the condition for trapping state is that the RHS of Eq. (4.15) is negative when the two pulses are well separated.

Using the Cauchy-Schwartz inequality, we obtain the following estimates for the value of R when the relative distance between them is large,

$$R \geq \frac{1}{2} \frac{N_1^2}{L_1} + \frac{1}{2} \frac{N_2^2}{L_2}, \quad (4.27)$$

where N_1 and N_2 are the wave actions and L_1 and L_2 are the distances over which the pulses extend in space. Note that L_1 and L_2 are not sharply defined, because even a soliton with a hyperbolic secant pulse shape does not have a well defined temporal extent. Therefore, it is understood that L_1 and L_2 are parameters related to the pulse width in which most of the pulse energy is located. Using this result, we obtain the sufficient condition for the trapping state:

$$H + \frac{1}{2} N_\alpha \delta_\alpha^2 + \frac{1}{4} \left(\frac{N_\alpha^2}{L_\alpha} \right) - \frac{1}{2} N \left(\frac{P + N_\alpha \delta_\alpha}{N} \right)^2 \leq 0. \quad (4.28)$$

It is important that all the terms involved in the above relation are constants of motion; thus, we can analyze the whole situation simply by considering these constants, no matter how the pulse shape changes. In order to gain some insight to this relation, we consider the symmetric input following the specific case of Menyuk^{8,9}

$$A_1 = A_2 = \frac{A}{\sqrt{2}} \operatorname{sech}(x). \quad (4.29)$$

From Eq. (4.27) and Eq. (4.28), the threshold condition is found to be

$$A_{\text{th}} = \left(\frac{1 + 3\delta^2}{1 + \epsilon - 3/L} \right)^{\frac{1}{2}}. \quad (4.30)$$

In order to compare our results with the results of Menyuk and Kivshar, we plot Eq. (4.30) in Fig. 4.1 with $\epsilon = 2/3$. Using the reduced variational method and the

soliton stability argument from inverse scattering theory, Kivshar obtained his linear relationship between A_{th} and δ , which is denoted by the solid line in Fig. 4.1. The dashed line is the estimate of Hasegawa,²⁶ who used a quantum mechanical analogy to the coupled NSE's. The numerical results of Menyuk are denoted by filled circles. Kivshar's results agree with the numerical simulations only when the linear birefringence is small, which is just the assumption he made in his method, and this assumption limits the range of validity of his method. Hasegawa's result gives an upper bound for the threshold amplitude. The band bounded by two solid curves is our result calculated from Eq. (4.30) by taking $L = 8$, and $L = 4$, respectively. The energies contained in hyperbolic secant pulses with symmetric extensions of $L = 4$ and $L = 8$ are 96% and 99.96%, respectively. The simulation results clearly show a nonlinear dependence of the threshold condition on the strength of linear birefringence. The unfilled circles are our numerical simulations, which are very close to the results of Menyuk's. We solved Eq. (4.1) and (4.2) using the split-step method,² which is described in detail in the Appendix. We used 2048 grid points in our simulation. In order to determine the threshold more accurately, our propagation distance of 50 soliton units is much longer than the propagation distance of Menyuk's.⁸ The uncertainty in determining the threshold value is 0.05. It is easy to see the agreement between our simulation with $L = 8$ and the prediction given by Eq. (4.30) when the birefringence parameter $\delta < 0.5$. When $\delta > 0.5$ simulation results approach the curve of $L = 4$. Finally, we want to point out that McKinstrie and Luther²⁷ showed that the linear modulational instability of waves governed by coupled NSE's can only occur in infinite media when the normalized convection velocity $\delta < A_0$. This is the same scaling we obtain in this section for the threshold amplitude A_{th} when δ is comparable to 1. Therefore, although the linear modulational instability is different from soliton entrainment, the scaling is the same, which suggests that the underlying physics is

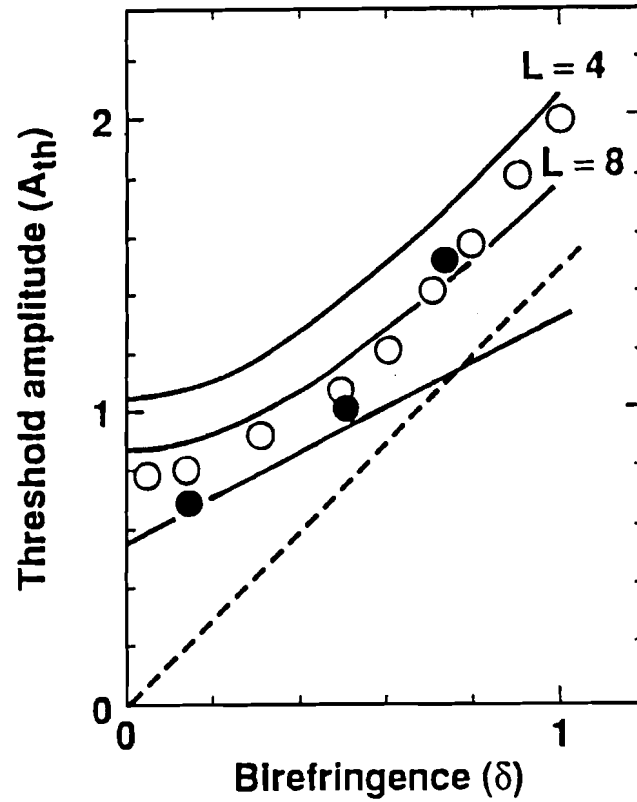


Fig. 4.1 The solid line shows the analytical result of Kivshar; the dashed line is the estimation of Hasegawa; the numerical result of Menyuk is given by filled circles; the band bounded by two solid curves is plotted according to Eq. (4.30) with $L = 8$, and $L = 4$, respectively, corresponding to 99.96% and 96% of the energy in a soliton pulse; the unfilled circles are our numerical simulations, $\epsilon = 2/3$.

similar. Associated with the nonlinear frequency shifts are corresponding shifts in the wave number and group velocity. Consequently, the entrainment of modulations or partial pulses is only possible over a certain range of δ . Since a minimum energy is required to generate a nonlinear frequency shift large enough to compensate the linear dispersion even in single NSE, the coupled NSE's also require a minimum energy to form a soliton: a threshold gap at $\delta = 0$ is expected and is confirmed by Eq. (4.30) and Fig. (4.1).

In our result, the threshold amplitude gap is a natural consequence of our analysis. But in the reduced variational approach of Kivshar,¹² this threshold gap cannot be obtained directly. In fact, Kivshar¹² made the assumptions that the coupled NSE's can support such quasi-solitons and that these quasi-solitons possess the same stability property as do the solitons of single NSE. Using a result from the inverse scattering method (ISM) about the stability of solitons, Kivshar¹² was able to obtain the threshold gap. However, we obtain this threshold gap from the virial theorem directly. In fact, the virial theorem can be utilized to study other aspects of the behavior of interacting solitons. Since the information about evolution is contained in R , analyzing R is sufficient to understand the interaction process. For example, if we assume that the partial pulses do not change their shape during the interaction, which is valid for small δ ,¹⁵ we have

$$d_{tt}^2 \langle \delta x^2 \rangle = d_{tt}^2 \Delta^2, \quad (4.31)$$

since the relative distance $\langle \delta x^2 \rangle$ differs from Δ^2 only by a constant, where Δ is the distance between the pulses measured from the center of each pulse. Making use of Eqs. (4.21) and (4.29) as the pulse profile, we get

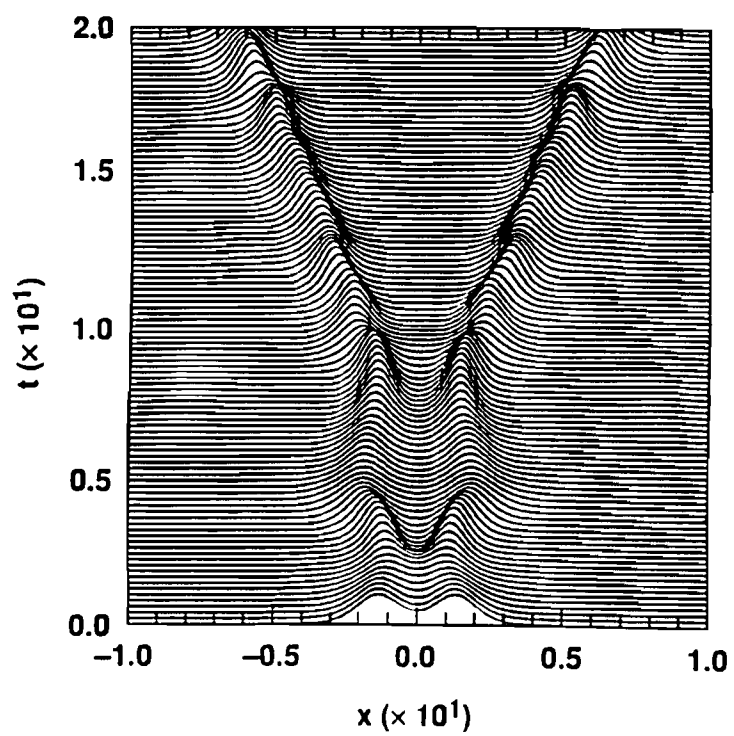


Fig. 4.2 The partial solitons are separated while experience nonlinear oscillations along their own paths.

$$R = R_0 + C \int \frac{dx}{\cosh^2(x) \cosh^2(x - 2\eta\Delta)}, \quad (4.32)$$

$$d_{tt}^2 \Delta^2 = \frac{4}{N} \left[H + \frac{1}{2} N \delta^2 + \frac{1}{2} R_0 + \frac{1}{2} C I(\Delta) \right], \quad (4.33)$$

where

$$C = \frac{8\epsilon\eta^3}{(1+\epsilon)^2}, \quad R_0 = \frac{32\eta^3}{(1+\epsilon)^2},$$

and

$$I(\Delta) = \int_{-\infty}^{\infty} \frac{dx}{\cosh^2(x) \cosh^2(x - 2\eta\Delta)}, \quad (4.34)$$

when $\Delta \ll 1$, $I(\Delta) \equiv \frac{4}{3} - \frac{8}{15} (2\eta\Delta)^2$. (4.35)

Equation (4.33) describes a nonlinear oscillator with gain or loss depending on the sign of the constant term on the RHS of Eq. (4.33). Thus, the oscillating term in Eq. (4.33) is given by

$$d_{tt}^2 \Delta^2 = -\frac{64C\eta^2}{15N} \Delta^2. \quad (4.36)$$

The oscillation frequency is

$$\omega_{\text{osc}}^2 = \frac{64\eta^4}{15(1+\epsilon)}. \quad (4.37)$$

We note that the oscillation frequency is proportional to the pulse intensity, a result earlier obtained previously by Kivshar¹² and Lisak, *et al.*¹⁵

Below the threshold, we have an amplified oscillator, and each pulse will be separated while oscillating around their uncoupled trajectory, as shown in Fig. (4.2).

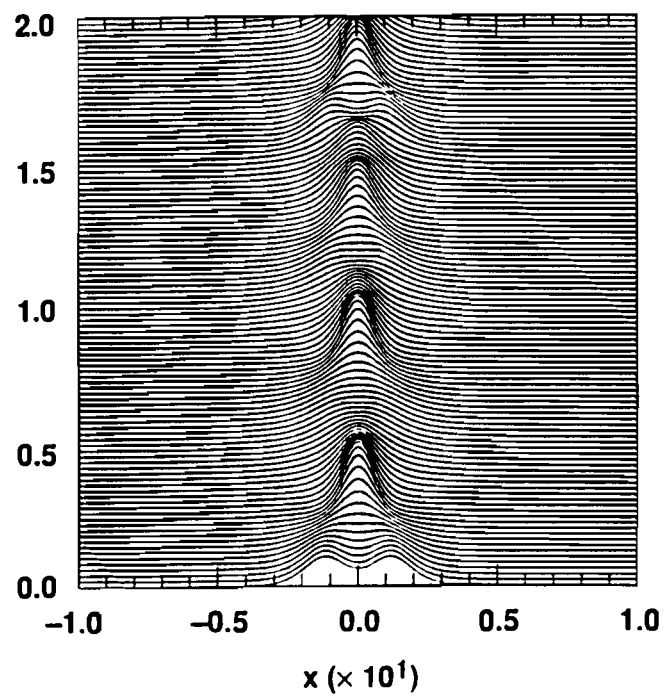


Fig. 4.3 The partial solitons bounce back and forth while propagating, and form a trapped state.

While above threshold, the colliding pulses will form a trapped state as shown in Fig. (4.3).

4.3 Collision of temporal vector solitons in birefringent optical fibers

This section is devoted to the study of soliton collisions in a nonlinear birefringent fiber. This subject attracts great current interest due to its scientific importance^{8,9,12,20,29-32} and its potential applications to optical logic devices.^{33,34} Pulse propagation in birefringent optical fibers is described by two coupled NSE,^{8,9,20} which are known to be nonintegrable by means of the inverse-scattering method [ISM].³⁵ The most important difference between an integrable nonlinear wave equation and a nonintegrable one is that the collision between solitary waves is elastic in the former case and inelastic in the latter.^{35,36} There is always radiation emitted during the solitary wave collisions in a nonintegrable system such as the system governed by the coupled NSE's.

In this section, it is found that strong radiation emission, which has some similarity to Cerenkov emission, is associated with the bound state. If the amplitudes of the two colliding solitons are below a threshold value, the two solitons will separate from each other after the collision. However, each soliton emerges from the collision in a mixed polarization. The component with smaller amplitude or energy is called the soliton shadow.⁹ Although the same phenomena as the soliton shadow is studied in this section, it is found that the amplitude of the shadow is not always much smaller than the other component, thus the word shadow is not an appropriate concept here. This phenomena is simply called mixing here without emphasizing the dominant contribution to the total polarization state. This kind of mixing also exists in the parametric interaction between solitons with different wavelengths.³⁸ Recently, Wang *et al.*³⁹ studied this mixing effect (soliton shadow) in birefringent optical fibers. They

found that the amplitude of the shadow is much smaller than that of the component that traps the shadow. The dependence of the shadow amplitudes, widths, and shapes on the initial separation of the colliding solitons has been studied in some detail. In this section, it is found that the relative contribution to the total polarization state varies in a large range and depends very sensitively on the linear birefringence. By linearizing the coupled NSE's, Malomed and Wabnitz⁴⁰ found that there exists a critical value of linear birefringence for which the soliton collision is resonant in the sense that the spatial frequency of the soliton shadow equals that of the soliton with much larger amplitude. Under the conditions of resonance, solitons collide with each other much more strongly, and show many new phenomena. When the linear birefringence is above this critical value, the interaction between two solitons is weak and each soliton picks up a shadow after a collision. Most of the previous work on soliton collisions was in the nonresonant regime, and the mixing effect was very small. In this section it is found that the resonant regime is more subtle in that it consists of bound states and unbound states. Therefore, the parameter space of linear birefringence is divided into three regimes corresponding to bound, unbound resonant, and unbound nonresonant states. In an integrable system, solitons do not change their velocities after a collision. However, in a nonintegrable system, the velocities of two colliding solitons generally change after a collision. We also investigate this phenomenon by numerical simulation. It is found that both the velocity change and the amount of mixing measured by means of cross-correlation depend strongly on the linear birefringence. The XPM between two colliding pulses generates nonlinear frequency shifts and, hence, velocity changes due to GVD. The dependence of the velocity changes on the linear birefringence is similar to that of the mixing on the linear birefringence. None of previous work on soliton collisions was concerned with the dependence on the linear birefringence. It is not surprising that only very small mixing has been found, since the linear birefringence

chosen in previous work was very large, and the collisions were nonresonant. The entire range of the linear birefringence is investigated in this section.

The governing equations have already been given in a previous section [Eq. (4.1) and (4.2)]. We consider collisions between two solitons that travel in two orthogonally polarized modes. Initially, the two solitons are represented as follows: ⁴¹

$$\begin{aligned} A_1'(z=0,t) &= A_0 \operatorname{sech}[A_0(t + t_0)], & A_2' &= 0, \\ A_2''(z=0,t) &= A_0 \operatorname{sech}[A_0(t - t_0)], & A_1'' &= 0 \end{aligned} \quad (4.38)$$

The two solitons, labeled by A_1' , A_2' , and A_1'' , A_2'' are assumed to have equal amplitudes; t_0 is equal to 5 in all the simulations, and $A_0 = (1 + \epsilon)^{-1/2}$. The initial conditions are chosen in such a way that the two colliding solitons are well separated before the collision. In this section, the propagation distance along fiber is denoted by z , while the local time variable is denoted by t .

Soliton collisions in a nonintegrable system, such as the one described by Eq. (4.38), have many interesting properties that do not appear in an integrable system. Among them are the mixing of two colliding solitons and the frequency shifts after collision. The frequency shifts are most important in the application of soliton logic devices. In dispersive media, the frequency shifts will result in time shifts due to the GVD. In order to investigate the mixing process quantitatively, the following parameter is introduced:

$$m(z) = \frac{\int_{-\infty}^{+\infty} |A_1(z,t)| |A_2(z,t)| dt}{\int_{-\infty}^{+\infty} |A_1(z=0,t)|^2 dt}. \quad (34.9)$$

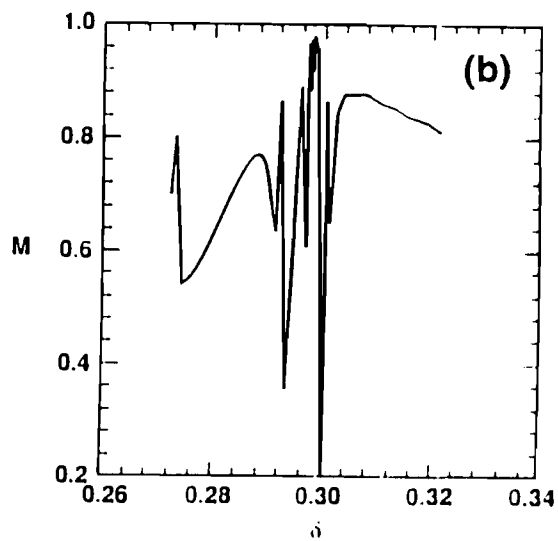
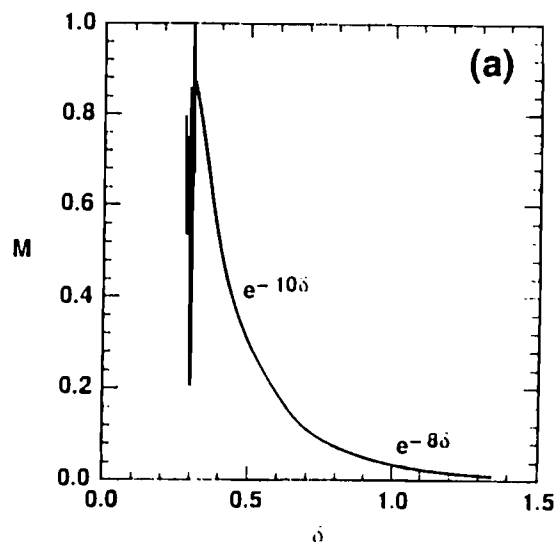


Fig. 4.4 Dependence of M on the linear birefringence δ . (a) The overall behavior. (b) Fine structure of the second interval, $0.27 < \delta < 0.305$.

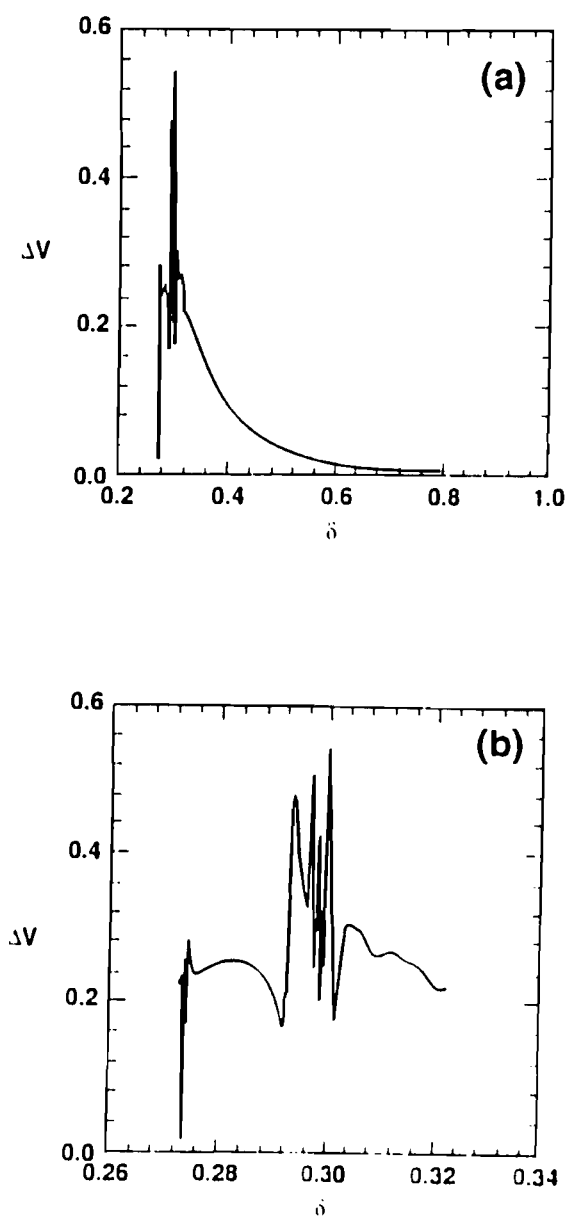


Fig. 4.5 Dependence of v - δ of colliding solitons on the linear birefringence δ . (a) The overall behavior. (b) Fine structure of the second interval, $0.27 < \delta < 0.305$

Since most of the energy of a soliton is localized, it is easy to see that $M = \lim_{z \rightarrow \infty} m(z)$ measures the overlap of two solitons after collision. When two identical solitons overlap exactly, $M = 1$; while they are well separated, $M = 0$. When above the threshold amplitude,^{8,9,12,20} two solitons overlap with each other, and M will be very large (approaching 1). It is easy to understand that high values of M exist when two solitons form a bound state after collision. The important thing is how M changes when there is no trapping. In an integrable system, there is no mixing after a collision; therefore, M will be 0 after the collision of two solitons. However, in the nonintegrable system studied in this section, it is found that M approaches a well-defined value after two colliding solitons are well separated from each other. In order to calculate M , we solve Eq. (4.1) and (4.2) numerically using the well-known split-step method (see Appendix). The initial conditions are given by Eq. (4.38), which guarantees that the two colliding solitons are well separated before collision. The linear birefringence parameter δ is used as a control parameter. Numerical simulations show that the mixing parameter M depends on the linear birefringence δ in a complicated way. There are three kinds of behavior depending on the values of δ . This can be seen from Fig. 4.4(a). The first regime is $0 < \delta < 0.27$, corresponding to the trapping state. In this case, two partial solitons form a breather-like trapping state, M oscillates between 1 and another high value (>0.5), and there is no asymptotic value of M . In this regime the soliton fusion is evident. Note that we leave this regime blank in Fig. 4.4(a) since M is not well defined in this region. The second regime is denoted by $0.27 < \delta < 0.305$. In this regime, the two colliding solitons interact strongly, bouncing back and forth around each other for several times and then separate from each other eventually. M value is well-defined; the fine structure of this regime is shown in Fig. 4.4(b).

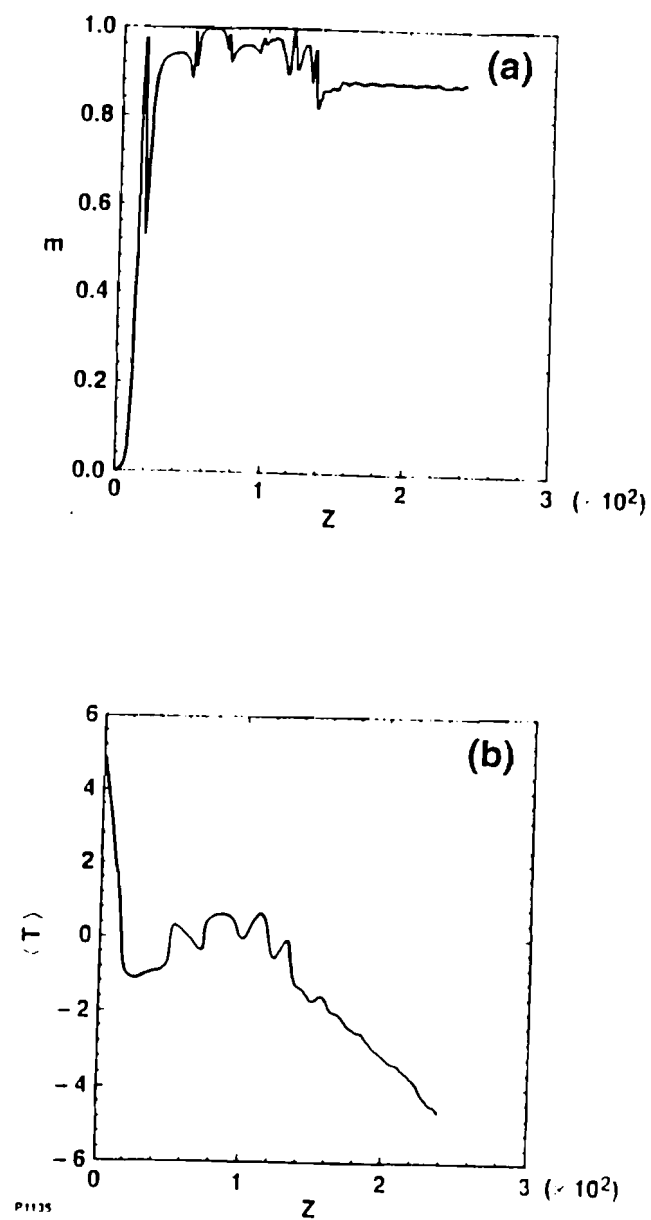


Fig. 4.6 Dynamic behavior of soliton collision in the second interval with $\delta = 0.298$. (a) Variation of $m(z)$ versus propagation distance Z . (b) Variation of center of mass of one soliton versus propagation distance Z .

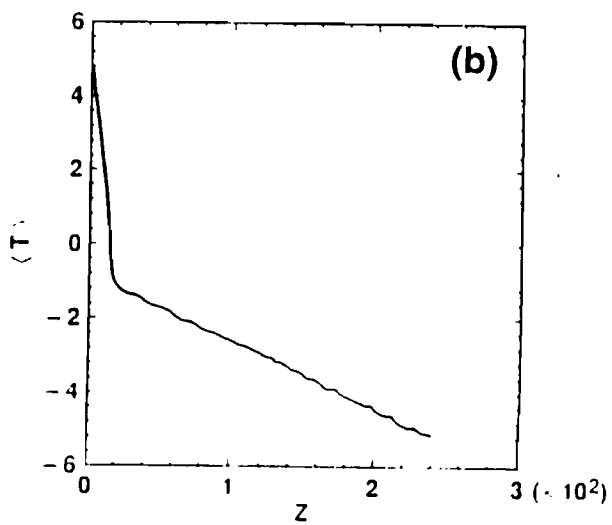
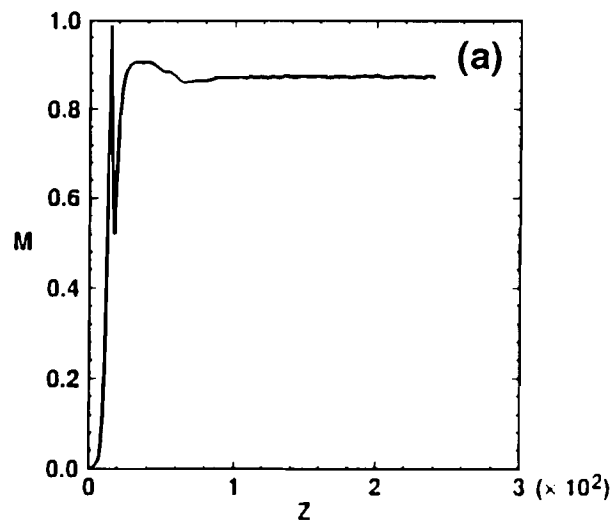


Fig. 4.7 Dynamic behavior of soliton collision in the second interval with $\delta = 0.304$.
 (a) Variation of $m(z)$ versus propagation distance Z . (b) Variation of center of mass of one soliton versus propagation distance Z .

Complicated oscillations occur in this regime. Small changes in δ generate very different final states. The third regime is represented by $\delta > 0.305$. M decays exponentially with increasing δ approximately as $e^{-10\delta}$. This behavior is easy to understand, since the larger the approaching velocity, the smaller the interaction.

The fact that soliton collisions in birefringent fibers are inelastic is very important for many potential applications in all-optical switching and optical logic gates. The inelasticity of soliton collision manifests itself by shifting the central frequencies and the velocities of the colliding solitons. In fact, the velocity changes are closely related to the frequency shifts by the GVD. Furthermore, the velocity change results in a time shift upon propagation along the fiber, which is the major mechanism

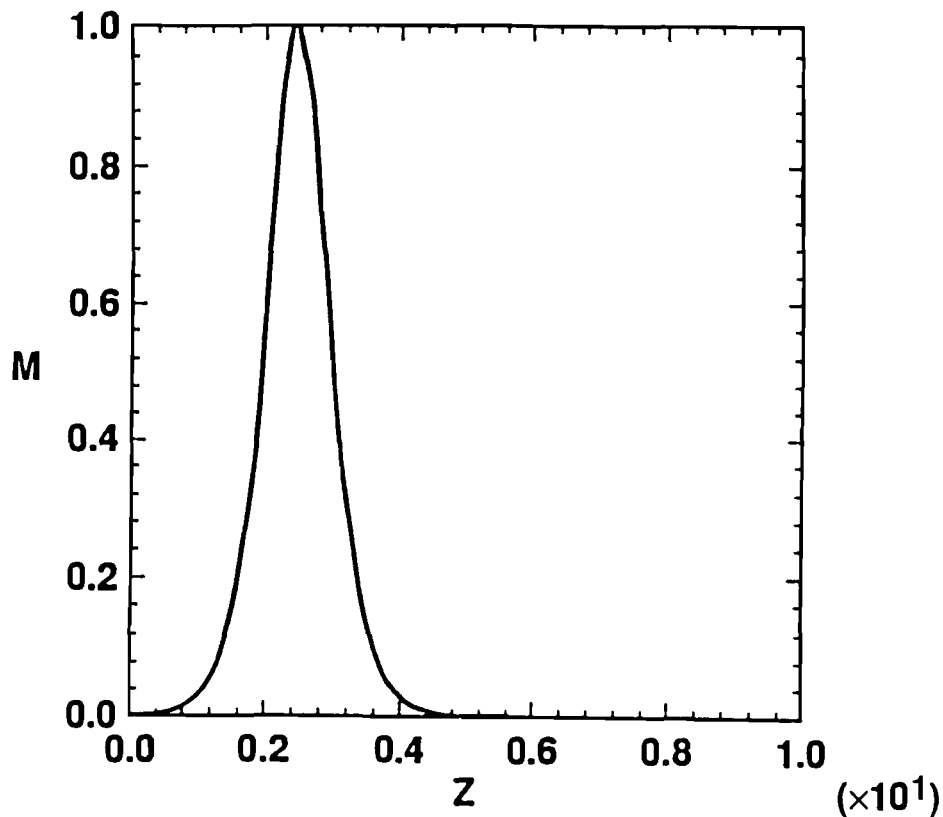


Fig. 4.8 There is no mixing when velocities of colliding solitons are large. $\delta = 2$.

of soliton-dragging logic gates.^{33,34} No such change is possible for a single NSE system because of its integrability. Here the velocity is free to change as long as the momentum of the system is conserved. Before collision, the two solitons will shift $\pm\delta$ in time respectively, after propagating a unit distance. In general, the time shifts per unit distance after a collision will no longer be $\pm\delta$. In this work, the time shift per unit distance of one soliton is labeled by v . As mentioned above, the time shift is closely related to the frequency shift due to the effect of GVD. In general, it is impossible to obtain a direction relationship between v and $\Delta\Omega_c$ (the center frequency of one soliton) due to the presence of SPM. However, it was found that the

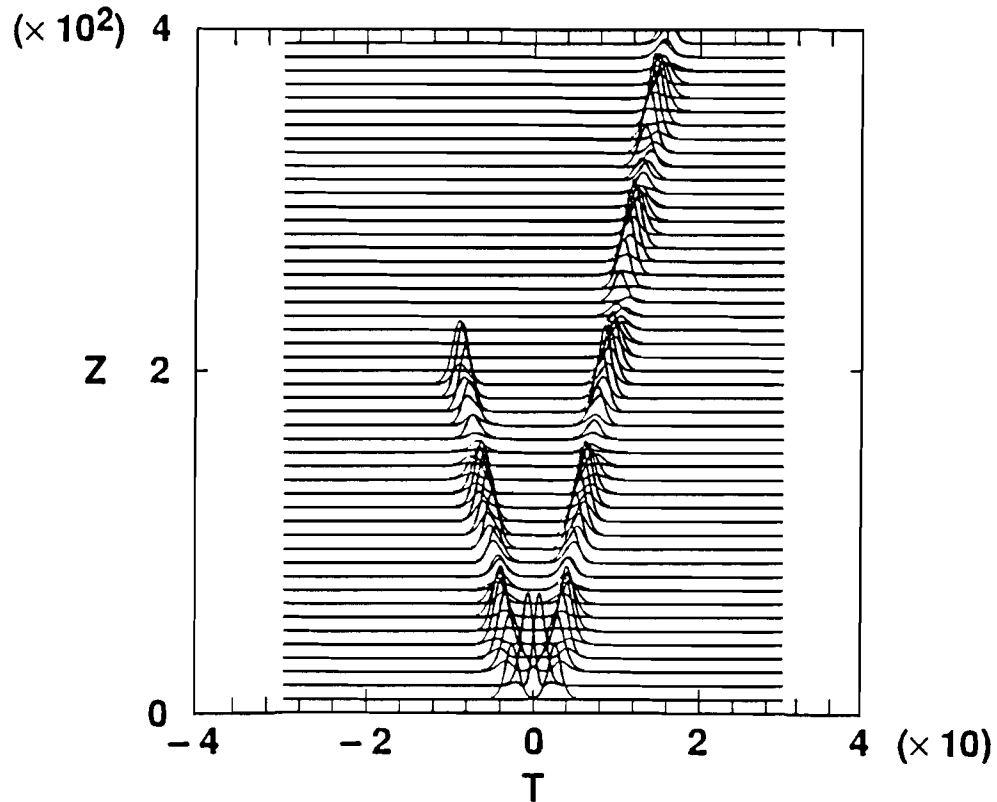


Fig. 4.9 A new kinds of soliton generated by soliton collision. $\delta = 0.304$. After 200 soliton periods, one of the outgoing solitons is used as the initial condition for the next simulation.

relationship between v and $\Delta\Omega_c$ is determined by the linear dispersion relation of Eq. (4.1) and (4.2) for colliding solitons,³⁷ and is given by $\Delta\Omega_c = \pm(v - \delta)$. The center-frequency shifts of the colliding solitons are equal to each other, but have a different sign. In this work, $v - \delta$ is calculated numerically. Figure 4.5(a) shows the dependence of $\Delta v = v - \delta$ on δ . It is easy to see that the dependence is similar to Fig. 4.4 as there are also three different regimes of behaviors. Figure 4.5(b) shows the fine structure of Δv in the second regime. It is evident that there is some correlation between Δv and M , and Δv shows similar structure as M . In the first section, that is $\delta < 0.27$, two colliding solitons trap each other and a bound state is formed; Δv is not defined. In the second regime, Δv shows rapid oscillations. In the third regime, Δv decreases exponentially in the same manner as M . It is interesting to note that the peaks in Δv are anticorrelated with those of M ; that is, a maximum of Δv corresponds to a minimum of M . It is believed that M is closely related to Δv . The center frequencies of both solitons are shifted due to XPM, and their group velocities are changed according to linear GVD.¹²

As an example, the dynamic behavior of m in a typical simulation is shown in Fig. 4.6(a). The simulation is done in the second regime with $\delta = 0.298$ and a propagation distance of 240 soliton periods. Initially the two solitons are well-separated, and the value of m is 0. As they approach each other, m increases almost to 1. The reason that m is less than 1 is because the collision is inelastic. At the moment just before total overlap, each soliton is split into two parts; the small part near the other soliton moves away rapidly and is trapped by the other soliton. After a quasi-bound period, the two colliding solitons separate from each other with a well-defined value of M . This means the final state of each outgoing soliton is a mixture of both polarization. The collision process can be seen more clearly in Fig. 4.6(b), in which the motion of

the center of mass $\langle T \rangle$ of one soliton is plotted. Initially, both solitons move with constant velocity 0.298; they interact strongly during the quasi-bound state. It is easy to see that the two solitons trap each other and move back and forth through each other four times until $Z = 140$. After $Z = 140$, they separate from each other with velocity about 0.03. Figure 4.7 shows the collision behavior in the third regime with $\delta = 0.304$. In this case, two solitons pass through each other and change their final velocities. Something interesting happens when the two colliding solitons are separating from each other, part of one soliton is taken away by the other. The larger the linear birefringence δ , the less the mixing. In fact this mixing decreases exponentially with increasing δ , as shown in Fig. (4.4). Figure 4.8 shows m for a nearly noninteracting situation with $\delta = 2$. m increases to 1 and then drops to zero after collision. Δv approaches zero after the collision.

Linear theory predicts that there is only one bound state and the amplitude ratio between the trapping pulse and the trapped pulse is large.⁹ The simulations in this section show that this is true in the third regime, especially for large values of δ . However, the situation changes quite a lot in the second regime or small δ , large values of mixing M exist as shown in Fig. 4.4. In order to show the evolution of an individual soliton, we plot the evolution of both solitons on top of each other in Fig. 4.9, that is, $|A_1|^2$ and $|A_2|^2$ are plotted individually in Fig. 4.9, not the total intensity $|A_1|^2 + |A_2|^2$. By doing this, the evolution of each polarization component can be seen more clearly. The parameters used in Fig. 4.9 are the same as that of Fig. 4.8. It is easy to see that the amplitude ratio between the trapping and the trapped pulses can be as large as 1. Another interesting feature is that this amplitude ratio is not a constant; it oscillates periodically. Careful examination shows that both the pulse width and pulse location of the trapping and trapped pulses can be different from each other. In fact the trapped pulse is moving back and forth in the potential well, generated by the stronger trapping

pulse. The amplitude of the strong pulse is also oscillating with the same period. The simulation is interrupted at position $Z = 200$ soliton periods, and the result is used as the initial condition for the next simulation of the same propagation distance. In the second simulation, the left soliton is taken away, only the right soliton of the previous simulation is allowed to evolve continuously. Calculation of M shows that it remains the same. This means that after collision the two outgoing mixed pulses move independently. After the collision, each pulse consists of both polarization. The energy confined in each pulse remains localized forever, hence they can be termed solitons. However, this kind of soliton has periodic internal motions, both the amplitude and pulse width of each polarization component are oscillating periodically, as shown in Fig. 4.9. Since linear theory assumes a fixed pulse shape, the mixing state here cannot be explained by linear theory. It is well known that there is no energy exchange between pulses with different polarization; therefore, the oscillations associated with pulse width, amplitude, and location is solely due to XPM between the trapping and trapped pulses. To the best knowledge of the author, this kind of soliton was not known before. Although there is no energy exchange between two pulses, the amplitude ratio can change from 1 to a very large value, since the pulse shape can change quite a lot. That is to say, by changing the phases of the two pulses, the amplitude ratio can be controlled at the end of fiber. This property could be useful in all-optical switches.

Since the system is nonintegrable, radiation is expected to exist. It is found that the trapping is not characterized by a particle model in the sense that each soliton emits photons through tunneling processes, while a particle model predicts two mechanical balls moving around each other.⁴² It is found that the breather formed by two trapping solitons suffers spontaneous decay by emitting dispersive waves, which have characteristics of Cerenkov emission. Figure 4.10(a) shows the Cerenkov emission is

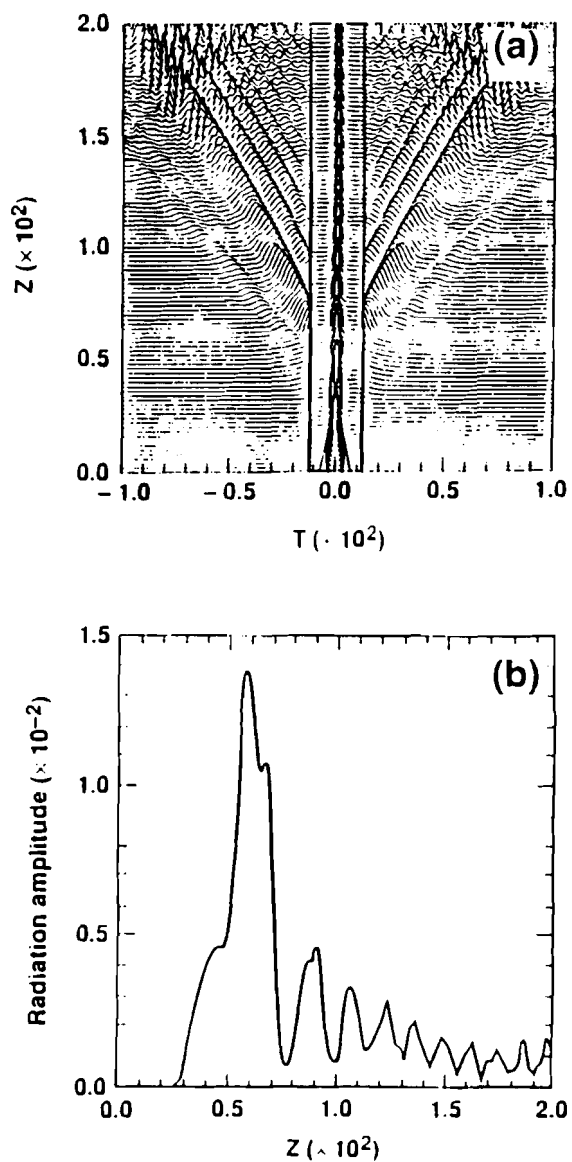


Fig. 4.10 Cerenkov emission generated by two colliding solitons in the second regime. $\delta = 0.2$, propagation distance $Z = 200$ soliton periods. (a) The trapping state is shown in the center, while the radiation is shown outside the center part. The radiation field is amplified 1000 times. (b) Radiation detected at position far from the trapping region, $t = 20$.

formed by two mutual trapping solitons. The radiation field has been magnified by a factor of 10^3 ; the center part is the trapping area. The initial velocities of colliding solitons is $\delta = 0.2$; it is found that the radiation moves three times faster than that of initial soliton velocities. Figure 4.10(b) shows the Cerenkov emission detected at a position far from the trapping region as a function of time. It seems that there is no correlation between the frequency of oscillating breather and that of the Cerenkov-like emission.

In summary, the soliton collision in birefringent optical fibers has been investigated numerically. It is found that the collisions can be divided into three regimes according to different values of linear birefringence δ . The first regime is denoted by $\delta < 0.27$, which corresponds to the soliton fusion or mutual trapped states. The second regime, from 0.27 to 0.304, is a transition regime. In this regime, two solitons interact with each other strongly and then separate eventually. The velocities and the center frequencies of both solitons are changed after collision. A quasi-bound state is found in this region. The third regime is represented by $\delta > 0.304$. Two colliding solitons pass through each other with their final velocities changed slightly. It is found that the center frequency shifts decrease exponentially as δ increases. The pulse mixing of different polarization has characteristics similar to those of the central frequency shifts. A new kind of soliton is found by numerical simulation, as shown in Fig. 4.8. Strong radiation is found to exist in the bound state. The radiation is generated by the internal motion of a pair of bound solitons. The bound solitons will relax to a final bound state by giving away extra energy, as shown in Fig (4.10).

4.4 Stability and collisions of spatial vector solitons

Spatial solitons have been investigated extensively recently because of their potential applications in all-optical switching and processing.⁴³⁻⁵⁰ Most previous

investigations have concentrated on collisions of scalar solitons with the same polarization and wavelength. Relatively little attention has been given to the propagation and interaction of spatial solitons with different polarization or wavelength. The propagation of scalar solitons is governed by NSE, while the propagation of vector solitons is governed by a pair of coupled NSE's.

The governing equations for the propagation of two light fields with different polarization are⁵¹

$$\begin{aligned} i(\partial_z + \theta \partial_x)A_1 + \frac{1}{2} \nabla_{xx}^2 A_1 + (|A_1|^2 + \epsilon |A_2|^2)A_1 + \frac{1}{2} \epsilon A_2^2 A_1^* \exp(-iR\theta x) &= 0, \\ i(\partial_z - \theta \partial_x)A_2 + \frac{1}{2} \nabla_{xx}^2 A_2 + (|A_2|^2 + \epsilon |A_1|^2)A_2 + \frac{1}{2} \epsilon A_1^2 A_2^* \exp(iR\theta x) &= 0, \end{aligned} \quad (4.40)$$

where A_1 and A_2 are the wave amplitudes in the two polarization, normalized to $(2n_0/n_2 k^2 w_0^2)^{1/2}$; n_0 is the linear refractive index of the medium; n_2 is the nonlinear refractive index; $k = n_0(2\pi/\lambda)$ is the wave number; λ is the wavelength of laser in vacuum; w_0 is beam width; z is the propagation axis, normalized to the diffraction length $z_d = kw_0^2$; and x is the transverse coordinate normalized to the beam width w_0 . θ is the normalized incident angle of each beam, $\theta = kw_0(k_x/k_z)$, k_x and k_z are the x and z component of the \mathbf{k} vector. $R = 4kw_0$. If the beam width w_0 is much larger than the wavelength, or $R\theta \gg 1$, then the four-wave mixing terms in Eq. (4.1-2) can be neglected. In this Section, we assume $R\theta \gg 1$. We consider the collisions between two solitons that travel in two orthogonally polarized modes, that is, $\epsilon = 2/3$. Here the medium is assumed to be the isotropic Kerr medium with instantaneous nonlinear response, and the incident angles of each beam are very small, $\pm(k_x/k_z) \ll 1$.

It is interesting to note that Eq. (4.40) becomes identical to Eq. (4.1) and (4.2) under the condition that $R\theta \gg 1$, which is true for most practical applications. Hence

the governing equations of temporal and spatial solitons are mathematically equivalent if this condition is satisfied. The results we obtained in Sections 4.2 and 4.3 can be applied here to spatial solitons with the following correspondance: the longitudinal propagation distance t in temporal solitons is replaced by z that has the same physical meaning; the local time variable x in temporal solitons now has a meaning of transverse coordinate of light beams; the linear birefringence δ in temporal solitons is replaced by the intersection angle θ between two intersecting or colliding light beams.

4.4.1 Fusion threshold of spatial vector solitons

Unlike temporal solitons in optical fibers in which birefringence is unavoidable, and therefore the problem of soliton stability under the splitting effect of birefringence is naturally an important issue, spatial solitons do not suffer from such an effect since the propagation distance is usually much smaller than that of optical fibers. However, the results of temporal soliton stability has an important application in spatial soliton collision, that is, the fusion of spatial solitons. When two spatial soliton beams collide with each other with an angle of 2θ , then according to the analogy between temporal and spatial solitons, they will trap each other if θ is smaller than a threshold value for a given intensity. As a result of this mutual trapping, they propagate along a common direction that is different from the original directions of both soliton beams. Replacing δ with θ in Eq. (4.30), we get the threshold condition for fusion of spatial solitons

$$A_{th} = \left(\frac{1 + 3\theta^2}{1 + \epsilon - 3/L} \right)^{\frac{1}{2}}. \quad (4.41)$$

More general conditions for the fusion threshold of nonsymmetric solitons ($A_1 >$ or $<$ A_2) can be obtained using Eq. (4.28). If condition (4.41) is met, then two solitons with

equal amplitudes will merge as a single soliton beam. This property of spatial solitons can be used to control a light beam with another light beam, a process that has applications in optical beam steering and optical switching.

4.4.2 All-optical switching via collisions of spatial vector solitons

In this section, we are going to discuss a very important issue in photonic device, that is, all-optical switching. Spatial solitons are easier to understand than temporal solitons, since the former can be understood within the concept of the refractive index. Spatial solitons are self-induced waveguides and the refractive index change is made by nonlinear refraction. The collision of spatial solitons can also be understood in terms of a refractive index change. For example, in the case of collisions of two spatial solitons with some intersection angle, in the intersection region one beam will see a spatially varying refractive index generated by another beam. It is well-known in optics that an inhomogeneity in refractive index will cause the incident beam to split into two parts: one is reflected and the other transmitted. Only for very special index profiles, the reflection is zero⁵². It is interesting to mention that one of these special index profile has exactly the shape of a hyperbolic secant. Therefore most phenomena of collisions of spatial solitons can be interpreted in terms of reflection, transmission, total internal reflection, and so on. After a collision, spatial solitons are usually split into two. The transmission or reflection varies from 0 to 1 depending on soliton intensity and intersection angle, which makes it possible to control one beam with another in a variety of ways. In this section, we will find how collisions of spatial solitons can be used in all-optical switching.

Before colliding, two incident spatial solitons are well separated, and are described by

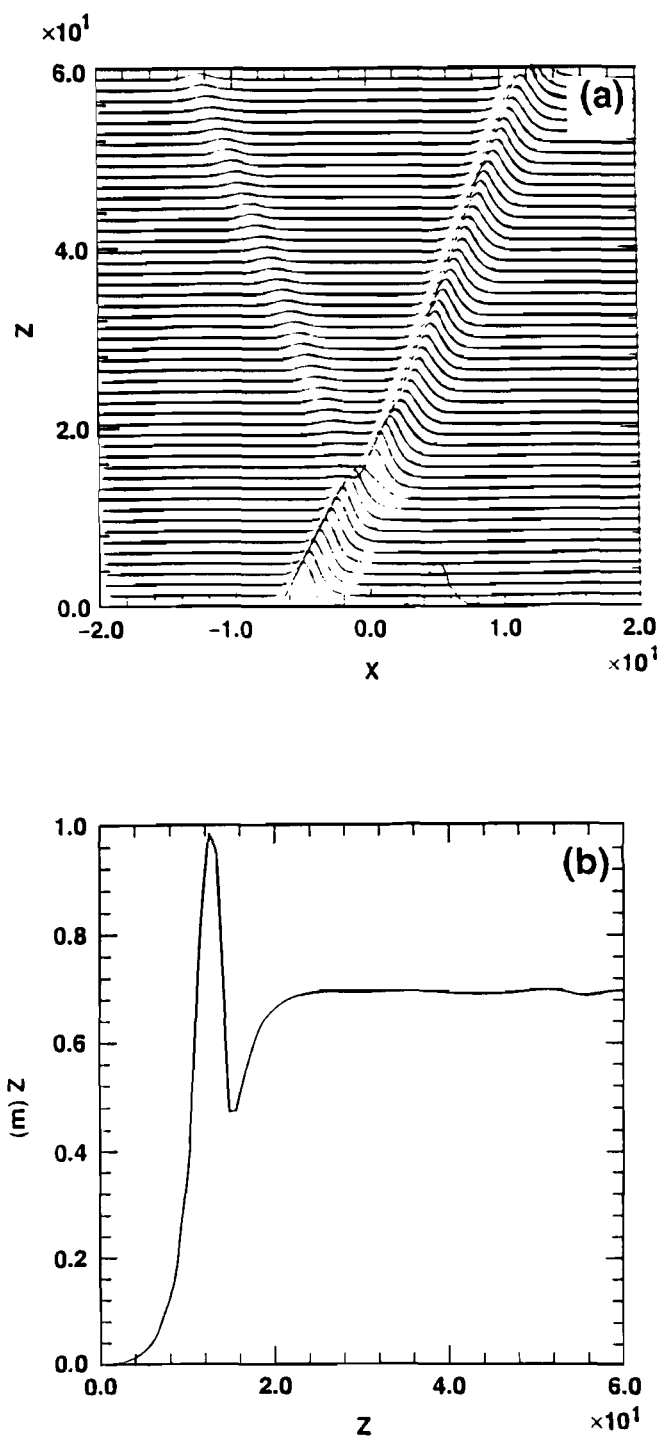


Fig. 4.11 Dynamic behavior of a soliton collision in the second regime with $\theta = 0.301$, $A_0 = 1$. (a) Propagation of the intensity profile of component A_1 . (b) Variation of $m(z)$ versus propagation distance Z .

$$\begin{aligned}
A_1'(z=0, x) &= A_0 \operatorname{sech}[A_0(x + x_0)] , & A_2' &= 0 , \\
A_2''(z=0, x) &= A_0 \operatorname{sech}[A_0(x - x_0)] , & A_1'' &= 0 ,
\end{aligned}
\tag{4.42}$$

Two solitons (labeled by A_1' , A_2' , and A_1'' , A_2'') are assumed to have equal amplitudes; x_0 is equal to 5 in all the simulations; and A_0 is the initial amplitude. The initial conditions are chosen in such a way that the two colliding solitons are well separated before the collision.

Similar to temporal solitons, the collision of spatial solitons can be classified into three kinds depending on the value of incident angle and intensity. For given incident intensities of both colliding solitons, the collision can be classified according to the value of the incident angle, just like the situation of temporal solitons. From section 4.3, we already know that there are three different regions of interactions; (a) soliton fusion or trapping region when $\theta < 0.27$. In this case, two colliding solitons form a breather-like trapping state. M oscillates between 1 and another high value (>0.5), and there is no asymptotic value of M ; (b) resonant region when $0.27 < \theta < 0.304$. In this region, the two colliding solitons interact strongly, bouncing back and forth several times and then separating eventually. M is well-defined; the fine structure of this regime is shown in Fig. 4.4(b). Complicated oscillations occur in this region. Small changes in θ generate very different final states. (c) perturbative region when $\theta > 0.305$. M decays exponentially with increasing θ approximately as $e^{-10\theta}$. After collision, each colliding soliton is no longer linearly polarized as before collision. Both solitons are elliptically polarized after collision. The change of propagation direction of each soliton after collision is similar to the change of velocity of temporal solitons, therefore Fig. 4.5 can also be used to describe the direction change of each soliton after collision with different incident angles.

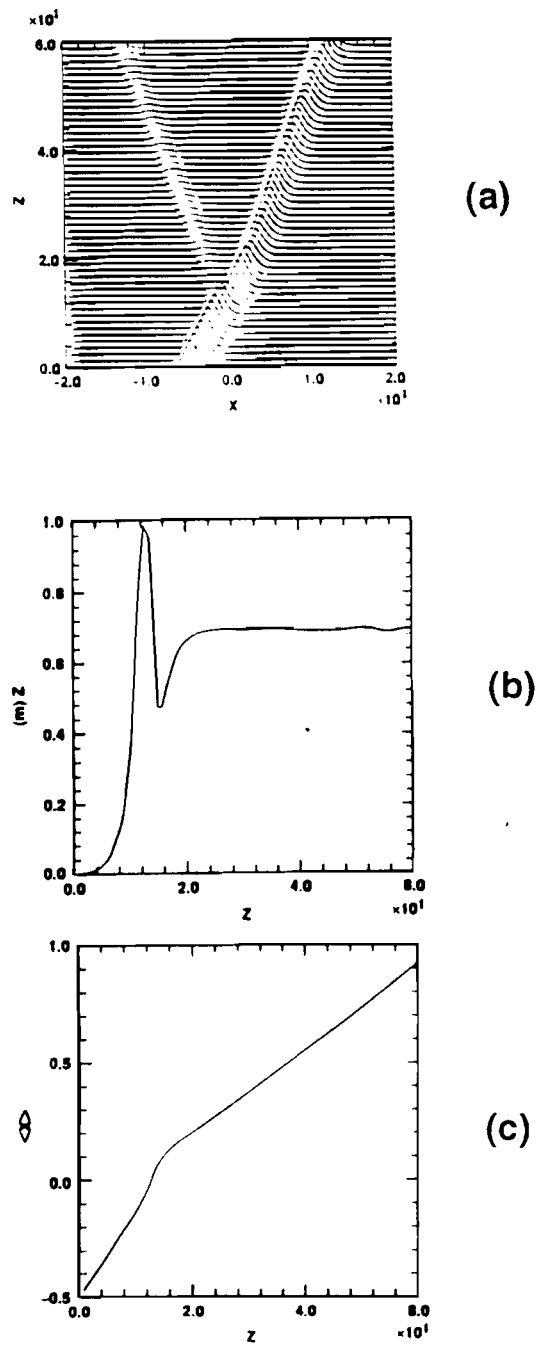


Fig. 4.12 Dynamic behavior of a soliton collision in the third regime with $\theta = 0.35$, $A_0 = 1$. (a) Propagation of the intensity profile of component A_1 . (b) Variation of $m(z)$ versus propagation distance Z . (c) Variation of center of mass of one soliton versus propagation distance Z .

The fact that soliton collisions are inelastic is very important for many potential applications in all-optical switching and optical logic gates. The inelasticity of soliton collision manifests itself by changing the propagation direction and the polarization state. Here the propagation direction is free to change as long as the momentum of the system is conserved. Fig. 4.5(a) shows the dependence of deflection angle $\Delta\theta = \theta_{\text{in}} - \theta_{\text{out}}$ on θ_{in} .

It is easy to see from Fig. 4.5 that the change in angle $\Delta\theta(\Delta\delta)$ can be either larger and smaller than the incident angle $\theta_{\text{in}}(\delta)$. This means that the center of mass can move toward the right and left with respect to the z-axis. This can be seen more clearly if we focus on the propagation of one of the colliding solitons—for example, the one that initially propagates from the left to the right. The propagation of the other component is symmetric due to the initial conditions. Figure 4.11(a) shows the propagation of the component A_1 in the second regime with $\theta = 0.301$, $A_0 = 1$. Before the collision, it moves as a soliton. After collision it has been split into two sub-beams that propagate as solitary waves along opposite directions because of the mutual guiding of A_1 and A_2 . It is obvious that the two sub-beams have nearly the same amplitude. Since A_2 is spatially overlapped with A_1 to form solitary waves, the polarization along each sub-beam is elliptical. On the other hand, the two sub-beams propagate along very different directions from the incident ones. Figure 4.11(b) shows the dynamic change of the overlapping or mixing parameter $m(z)$. Initially, the two colliding solitons are well separated, $m(z) = 0$; $m(z)$ approaches 1 during collision; and M is constant after collision. In fact, $M = 0.87$ means that the mixing of two polarization is very large; in other words, the energy carried by each polarization is comparable to the other. The ratio of energies carried by each sub-beam is measured to be 2:3 in Fig. 4.11(a). Figure 4.12 shows the propagation in the third regime with $\theta = 0.35$, $A_0 = 1$ —the mixing is smaller but there is still a large beam deflection. Figure

4.12(a) shows the propagation of the beam profile. There is a small amount of energy carried away by the soliton with perpendicular polarization. In fact, the sub-beam moving toward the left carries 14% of the input energy. Figure 4.12(b) shows the change of the mixing parameter $m(z)$. Figure 4.12(c) shows the trajectory of the center of mass, which is close to that of the sub-beam moving toward the right. It is clear from both Figs. 4.12(a) and 4.12(c) that the incident beam is significantly deflected. Figure 4.13 shows that the beam can even be completely switched into another channel. The parameters of Fig. 4.13 are $\theta = 0.3002$, $A_0 = 1$, that is, in the second regime. Initially, the beam propagates from the left to right and is totally reflected after collision. Both incident soliton beams experience total internal reflection because of the nonlinear refraction. The mixing is small; in other words, the beam is still linearly polarized. Physically, the soliton interactions can be understood based on the refractive index changes caused by light beams. Usually, any disturbance in the refractive index will split an incoming beam into two parts, reflected and transmitted. However, this is not true for the case when the refractive index change has a hyperbolic secant profile. It is well known that there is no reflection in this case. For soliton collisions with larger incident angle, the intensity profiles of both beams do not change much, therefore the refractive index changes seen by each beam are still of the form of a hyperbolic secant, thus the reflection is very small. However, there are large distortions in intensity profiles of both beams when the incident angle is small, which causes large reflection of each beam. Under some conditions, the reflectivity of each beam can be as large as 100% (Fig. 4.13). The largest deflection corresponds to this total reflection, which depends on detailed resonant conditions.

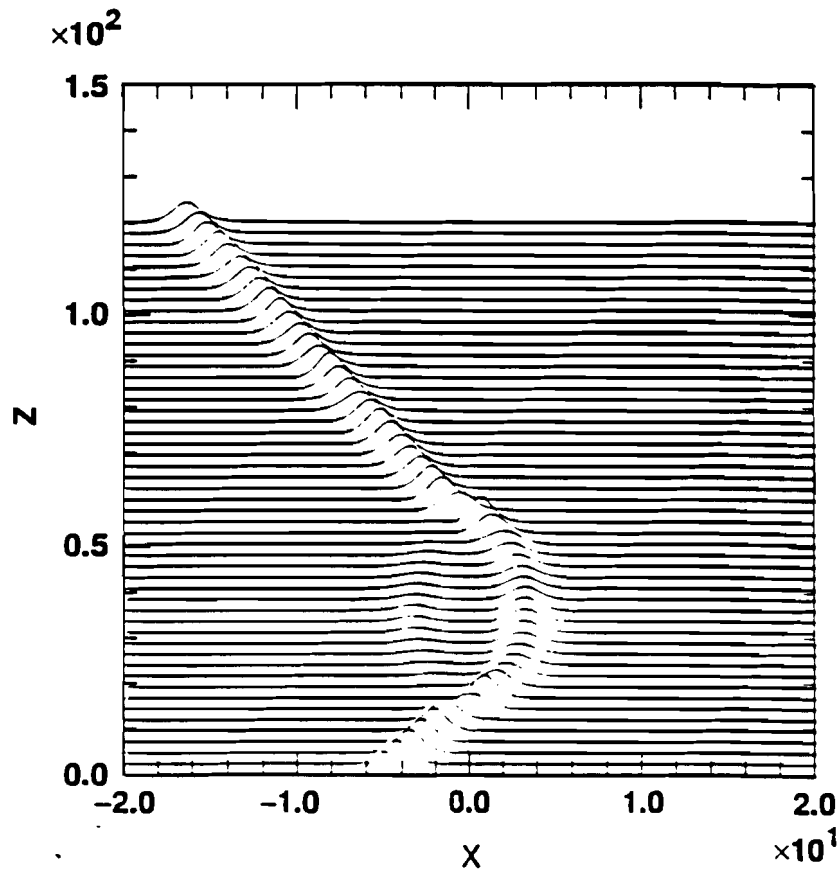


Fig. 4.13 Dynamic behavior of soliton collision in the second regime with $\theta = 0.3002$, $A_0 = 1$. Each soliton is totally reflected by the other because of the nonlinear refraction.

4.5 Conclusions

In this chapter, we studied the interaction of two orthogonally-polarized laser pulses in a birefringent optical fiber. The spatio-temporal evolution of the two partial pulses is governed by a pair of coupled NSE's. Several conservation laws associated with these equations were found and used to determine a one-parameter family of solitary-wave solutions in which the partial pulses have identical profiles. Among them is the conservation of momentum, which implies that each partial pulse shifts its frequency in such a way that the total shift is zero, since the total frequency shift is proportional to the total momentum change. This frequency shift is crucial to a physical

understanding of soliton collisions involving the walk-off effect. For these solitary-waves, the walk-off effect is negated by frequency and wave-number shifts, which modify the group velocities of the partial pulses so that they propagate at a common velocity. A similar physical mechanism underlines the attraction and entrainment of two partial pulses whose centers are offset. The Kerr nonlinearity allows each partial pulse to first alter the other's average frequency and wave number. GVD then modifies the velocity of the pulses so that they attract each other. The entrainment of two partial pulses was discussed quantitatively using a virial theorem. By analyzing the virial theorem, we obtained the relation between the threshold amplitude for soliton formation and the linear birefringence. Our analytic result agrees well with numerical simulations. We were able to study the oscillating pulse interactions, and found that they can be described by a nonlinear oscillator with gain or loss depending on the sign of a constant, when the partial pulses do not change their shape during the interaction. This assumption is not a good one when there is loss, since no collapse can occur in one spatial dimension. Thus each partial pulse has to change its shape in such a way that loss is saturated, or loss becomes gain to make the whole system oscillate nonlinearly. We estimated the oscillation frequency and found that it is proportional to the pulse intensity.

The effects of linear birefringence on soliton propagation in optical fibers can be controlled by choosing the input power correctly. As long as the input power is greater than a certain threshold value, but is less than the power required to generate higher-order solitons, the fundamental soliton will not suffer from walk-off or pulse-splitting due to the presence of birefringence, and can be used as an information bit in soliton-based communication systems. In practice, even polarization-preserved fibers suffer from temperature, stress and other inhomogeneities, and the linear birefringence may not be constant. Although some attention has been paid to this problem,²⁸ the

issue of how randomly changing birefringence affects soliton propagation in optical fibers is not yet understood completely.

Since the same coupled NSE's can be used to describe obliquely interacting waves,²¹ this soliton solution is also valid for spatial solitons in one perpendicular direction with the linear birefringence replaced by the perpendicular velocities. We showed in section 4.4 that there exists such an analogy between the temporal and spatial solitons, and all the results of temporal solitons found in this section carry over to the spatial solitons. The collisions of spatial vector solitons have also been investigated numerically. It is found that there are three regimes of interaction in the parameter space of the normalized incident angle θ . The first regime is the a trapping regime, in which the nonlinear refraction is strong enough to negate the divergence of the two colliding solitons. From the point of view of optical switching, this region can be used as Y-junctions. The second regime is called the resonant region, in which solitons interact strongly with each other. Two colliding solitons separate from each other after collision. Because of the inelasticity of the collision, each beam is split into two sub-beams that propagate as solitary waves due to the effect of XPM. Both the polarization and propagation directions are changed after collision, which could be useful in the applications of all-optical switching. The third regime is the weak interaction region. Both the polarization mixing and the beam deflection become exponentially smaller as θ increases. It should be pointed out that there are several advantages to using vector solitons over scalar solitons as switching devices. First, using different polarization allows one to obtain high switching contrast. Secondly, since there is no interference between two perpendicularly polarized light waves, the switching will be phase insensitive, while scalar solitons have strict requirements for the phases of the colliding solitons. Finally, it should be mentioned that the behavior of

soliton collisions depends sensitively on the angle of incidence, which may be a drawback of this method.

REFERENCES

1. Optical solitons, J. R. Taylor ed. (Cambridge University Press, Cambridge, 1992).
2. G. P. Agrawal, Nonlinear Fiber Optics (Academic Press, Boston, 1989).
3. D. N. Christoulides and R. I. Joseph, *Opt. Lett.* **13**, 53 (1988).
4. A. Hasagawa and F. Tappert, *Appl. Phys. Lett.* **23**, 142 (1973).
5. L. F. Mollenauer, R. H. Stolen, and J. P. Gordon, *Phys. Rev. Lett.* **45**, 1095 (1980).
6. L. F. Mollenauer, R. H. Stolen, J. P. Gordon, and V. J. Tomlinson, *Opt. Lett.* **8**, 289 (1983).
7. L. F. Mollenauer, M. J. Nevbel, S. G. Evangelides, J. P. Gordon, J. R. Simpson, and L. G. Cohen, *Opt. Lett.* **15**, 1203 (1990).
8. C. R. Menyuk, *IEEE J. Quantum Electron.* **QE-23**, 174 (1987).
9. C. R. Menyuk, *J. Opt. Soc. Am. B* **5**, 392 (1988).
10. G. Gregori and S. Wabnitz, *Phys. Rev. Lett.* **56**, 600 (1986).
11. E. Caglioti, B. Crosignani, and P. Di Porto, *Phys. Rev. A* **38**, 4036 (1988).
12. Y. S. Kivshar, *J. Opt. Soc. Am. B* **7**, 2204 (1990).
13. A. Bondeson, D. Anderson, and M. Lisak, *Phys. Scr.* **20**, 479 (1979).
14. D. Anderson and M. Lisak, *Phys. Rev. A* **32**, 2270 (1985); D. Anderson and M. Lisak, *Opt. Lett.* **11**, 174 (1986).
15. M. Lisak, A. Hook, and D. Anderson, *J. Opt. Soc. Am. B* **7**, 810 (1990).
16. V. E. Zakharov, V. V. Sobolev, and V. S. Synakh, *JETP Lett.* **14**, 390 (1971).

17. S. N. Vlasov, V. A. Petrishchev, and V. I. Talanov, *Izv. Vyssh. Uchebn. Zaved. Radiofiz.* **14**, 1062 (1971). *Radiophys. and Quantum Electron.* **14**, 1062(1971).
18. F. H. Berkshire and J. D. Gibbon, *Stud. Appl. Math.* **69**, 229 (1983).
19. C. J. McKinstrie and D. A. Russell, *Phys. Rev. Lett.* **61**, 2929 (1988).
20. C. R. Menyuk, *IEEE J. Quantum Electron.* **25**, 2674 (1989).
21. X. D. Cao, C. J. McKinstrie, and D. A. Russell, *Bull. Am. Phys. Soc.* **36**, 2273 (1991).
22. H. Goldstein, *Classical Mechanics*, 2nd ed. (Addison-Wesley, Reading, Massachusetts, 1980), Chap. 12.
23. W. B. Mori, T. Katsouleas, C. B. Decker, and J. J. Su, *Bull. Am. Phys. Soc.* **36**, 2305 (1991).
24. K. Murawski (private communication, 1989).
25. M. V. Trantnik and J. E. Sipe, *Phys. Rev. Lett.* **58**, 1104 (1987); *Phys. Rev. A* **38**, 2011 (1988).
26. A. Hasagava, *Opt. Lett.* **5**, 416 (1980).
27. C. J. McKinstrie and G. G. Luther, *Phys. Scri.* **T-30**, 31 (1990).
28. P. K. Wai, C. R. Menyuk, and H. H. Chen, *Opt. Lett.* **16**, 1231 (1991).
29. K. J. Blow, N. J. Doran, and D. Wood, *Opt. Lett.* **12**, 202 (1987).
30. S. Trillo, S. Wabnitz, E. M. Wright, and G. I. Stegeman, *Opt. Lett.* **13**, 871 (1988).
31. M. V. Trantnik and J. E. Sipe, *Phys. Rev. A* **38**, 2011 (1988).
32. B. A. Malomed, *Phys. Rev. A* **43**, 410 (1991).
33. M. N. Islam, C. E. Socolich, and D. A. B. Miller, *Opt. Lett.* **15**, 909 (1990).
34. M. N. Islam, C. R. Menyuk, C.-J. Chen, and C. E. Socolich, *Opt. Lett.* **16**, 214 (1991).

35. Y. S. Kivshar and B. A. Malomed, *Rev. Mod. Phys.* **61**, 763 (1989).
36. Y. Kodama, *Phys. Lett. A* **123**, 276 (1987).
37. X. D. Cao and C. J. McKinstrie, *J. Opt. Soc. Am. B* **10**, 1202 (1993).
38. L. M. Kovachev, *Opt. Quantum Electron.* **23**, 1091 (1991).
39. Q. Wang, P. K. A. Wai, C.-J. Chen, and C. R. Menyuk, *Opt. Lett.* **17**, 1265 (1992).
40. B. A. Malomed and S. Wabnitz, *Opt. Lett.* **16**, 1388 (1991).
41. X. D. Cao and D. D. Meyerhofer, *J. Opt. Soc. Am. B* **11**, 380 (1994).
42. E. Caglioti, B. Crosignani and P. Di Porto, *Phys. Rev. A* **38**, 4036 (1988).
43. M. Shalaby and A. Barthelemy, *Opt. Lett.* **16**, 1472 (1991).
44. R. de la Fuente and A. Barthelemy, *IEEE J. Quantum Electron.* **28**, 547 (1992).
45. A. W. Snyder and A. P. Sheppard, *Opt. Lett.* **18**, 482 (1993).
46. M. Shalaby and A. Barthelemy, *Opt. Commun.* **94**, 341 (1992).
47. M. Shalaby, F. Reynaud, and A. Barthelemy, *Opt. Lett.* **17**, 778 (1992).
48. A. P. Sheppard, *Opt. Commun.* **102**, 317 (1993).
49. C. De Angelis and G. F. Nalesso, *J. Opt. Soc. Am. B* **10**, 55 (1993).
50. G. E. Torres-Cisneros, J. J. Sánchez-Mondragón, and V. A. Vysloukh, *Opt. Lett.* **18**, 1299 (1993).
51. X. D. Cao and D. D. Meyerhofer, to be published in *Opt. Lett.*
52. V. L. Ginzberg, *Propagation of Electromagnetic Waves in Plasma*, (Gordan and Breach, New York, 1962).

Chapter 5

Self-defocusing of ultraintense laser pulses in a low pressure gas target

In this chapter, we study ionization-induced defocusing of laser beam in a thin gas target. It is found that the self-defocusing can be significant at a pressure as low as 2 torr. By developing a simple thin lens approximation, we are able to understand this experimental finding. The reason that self-defocusing can be important at such low pressure is due to the $f^\#$ -dependence of self-defocusing. The experimental results at different focal geometry, or $f^\#$ agree with the thin lens approximation. It is also found that the thin lens approximation can't explain all of the experimental data, especially the formation of ring structures in the intensity distribution. The experimental data showed that there are two foci in the image plane, which corresponds to an intensity distribution of a cone with a central spot. Based on the thin lens approximation, we have developed an improved computer model to explain the cone formation. The computer simulation shows that the cone formation is caused by the saturation of the electron density at the beam center. Good agreement was obtained between computer simulation and experiment.

5.1 Introduction

Nonlinear propagation of short pulses in an ionized gas or plasma has become a new research area for nonlinear optics dealing with high intensity laser-matter interaction since highly ionized plasmas represents the only practical optical material at intensities above 10^{13} W/cm². One of the important phenomenon is the self-defocusing due to the nonlinear refraction generated by the ionized electrons. This self-defocusing limits the maximum intensity and has a significant effect on multiphoton ionization, high harmonic generation, relativistic self-focusing and coherent x-ray generation, as we have discussed in Ch. 1. It can also strongly distort the beam characteristics. Recently new interest has been stimulated by the potential applications of ultrashort intense laser pulses in underdense plasmas, both experimental investigations¹⁻⁵ and computer simulation^{3,4,6,7} have been done. All these studies have been performed at relatively high pressure, for example, > 10 torr for high harmonic generation, > 1 bar for x-ray recombination lasers and plasma-based accelerators. It was found recently that self-defocusing could be important at a pressure as low as 3 torr with an intensity of the order of 10^{14} W/cm² and $f^\# = 70$.⁸ The focal spot increased three times compared with case in vacuum.⁸ The significance of this finding is that it shows that self-defocusing may play a more important role than previously expected. For example, both works of Auguste et al² and Rae⁷ were performed in a situation that a backfilled gas tank at pressure larger than 15 torr were used. Rae found that the tighter the focus, or the smaller the f-number or, $f^\#$ of the focusing system, the larger the maximum electron density. Intuitively, more severe self-defocusing is expected for smaller $f^\#$, since the change in refractive index is proportional to N_p . However, both the effective interaction length and ionized volume will be smaller for a beam with tighter focus, which results in a less accumulated phase distortion. Therefore, the self-defocusing will be less significant for smaller $f^\#$. Although Rae's result is consistent with Ref.(8), it is still

surprising to see self-defocusing at a pressure as low as one torr in a thin target. In order to understand this, we developed a thin lens approximation. It is found that the significant self-defocusing at pressure as low as a few torr can be explained by the $f^{\#}$ dependence of self-defocusing. We also found that the saturation of focal shifts can be explained by this model. On the other hand, the experimental data clearly shows the cone formation in the laser intensity distribution, which is beyond the thin lens approximation. However, an improved model based on thin lens approximation can be used to explain the cone formation. Since this improved model is more complicated than the thin lens approximation, we can only obtain results by computer simulation, instead of analytic results.

Since most experiments on high order harmonics generation are performed at low pressure, the phase front distortion due to the self-defocusing may have an important effect on the phase matching of HHG.⁸ All the previous experimental observations of focal shifts were done by looking at the fluorescence generated by the plasma.¹⁻⁵ The observed focal shifts don't have to be the same as those of laser beam, since the plasmas don't contain all the information of the laser beam, and the fluorescence usually last much longer than the laser duration. In this work, we measure the laser beam directly using an equivalent target plane(ETP) measurement. Starting from a thin lens approximation, we can study the dependence of self-defocusing on different focal geometry, or more explicitly, the f-number($f^{\#}$) of the laser system. It is found that this model can explain the recent finding that self-defocusing could be important at a pressure as low as a few torr.⁸ Our simulation results confirm the existence of cone formation found in our experiments. Both our experimental method and theoretical models have the advantage of separating the self-defocusing from the complicated processes of ionization, therefore detailed understanding of self-defocusing becomes possible.

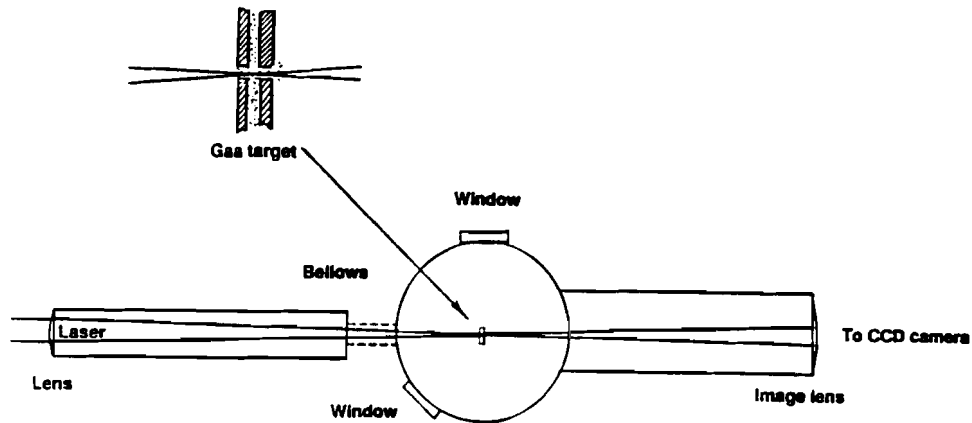


Fig. 5.1 A top-view schematic of the vacuum chamber. The distance from the lens to the focus is approximately 1.5 m.⁸

The organization of this chapter is as follows. After the Introduction, we discuss the experimental setup in Sec. 5.2. In Sec. 5.3, we show our experimental results. We discuss the theory and computer simulations in Sec.5.4. We also make detailed comparison between theory and experiment in this section. Finally, the results are summarized in Sec. 5.5

5.2 Experimental setup

Fig. 5.1 shows a top-view schematic of the vacuum chamber.⁸ The laser beam enters the system through a 153cm lens which is mounted on the end of a long tube. The laser focuses to the middle of the central tank where the gas target is positioned. The chamber is evacuated by a diffusion pump. The background pressure is below 10^{-6}

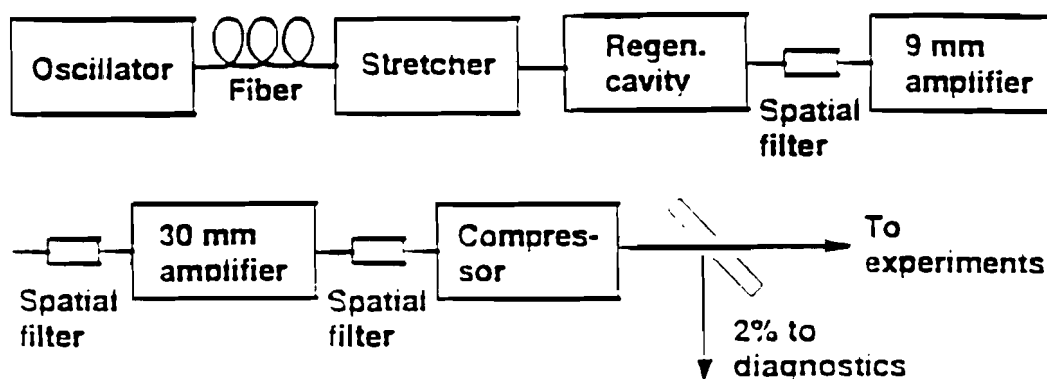


Fig. 5.2 Schematic of the chirped-pulse-amplification laser system.⁸

Torr. Near the focus, the laser beam intersects a thin gas target which provides a low-density gas distribution. A magnified figure of the cross-section of the target is also shown in Fig. (5.1). More detailed information about the target design and properties of the gas target can be found in Ref.(9).

The laser which has been described in details elsewhere is a neodymium glass system which operates on the principle of chirped-pulse amplification.^{10,11} Fig. 5.2 shows a schematic experimental setup of the whole laser system. The oscillator is an actively mode-locked Nd:YLF laser working at wavelength of $1.053 \mu\text{m}$. The oscillator produces a train of pulses with 100 MHz repetition rate, each pulse is 50 ps in duration with about 1 nJ energy. The average output power of the oscillator is about

0.5 W. The bandwidth of each pulse is increased from 0.03nm to 3.5nm due to the presence of self-phase modulation. Due to the group velocity dispersion(GVD) of the optical fiber, the pulse width is broadened from 50 ps to 120 ps at the output of the fiber. The stretcher consists of a pair of grating and a telescope sitting between the two gratings. The spectral-broadened pulses can be stretched to 300ps by the stretcher. A Pockel cell is used to switch a single pulse to seed a Q-switched regenerative amplifier. Another Pockel cell is used to switch out the amplified pulse with an energy about 0.3 mJ. Gain narrowing of the glass amplifier causes a reduction of the bandwidth from 3.5nm to 1.6nm. A spatial filter located between the regenerative amplifier and the 9-mm-amplifier is used to improve the beam quality. This 200cm air spatial filter has a magnification of 3, which increases the beam diameter from 2.0mm to 6.0mm. The beam is then coupled into the 9-mm-amplifier with a total gain of 150. The schematic setup of the 9-mm-amplifier system is shown in Fig. (5.3). The diffraction caused by the hard aperture of the amplifier rod is removed by the 90cm vacuum spatial filter with a magnification of 1. The pulse coming out of the 9-mm-amplifier has an energy of 50mJ and a duration about 300ps. After passing through a 160cm vacuum spatial filter with a magnification of 3, the laser pulse is aligned to the 30-mm-amplifier with a gain up to 60. The 30-mm-amplifier is followed by another vacuum spatial filter with a length of 275cm, magnification of 1.2. At this point, the laser beam has a diameter of 22mm, it can be either up-collimated to 58mm using a Galilean up-collimator with magnification $8/3$, or kept the same size before coupled into the optical pulse compressor which can compress the pulse to 1ps. The compressor consists of a pair of gold holographic gratings (1740 lines/mm) sitting parallel to each other. A 1cm glass plate is used to split 2% of the energy for diagnostics, such as pulse duration and pulse energy. The pulse energy is measured by a PIN diode which is connected to a digitizer and a PC. A background free single-shot autocorrelator is used to measure the pulse

width. The autocorrelator is based on the second harmonic generation (SHG) in a 1mm-thick nonlinear crystal (LiIO_3). The autocorrelator has different calibrations for beams with different sizes.

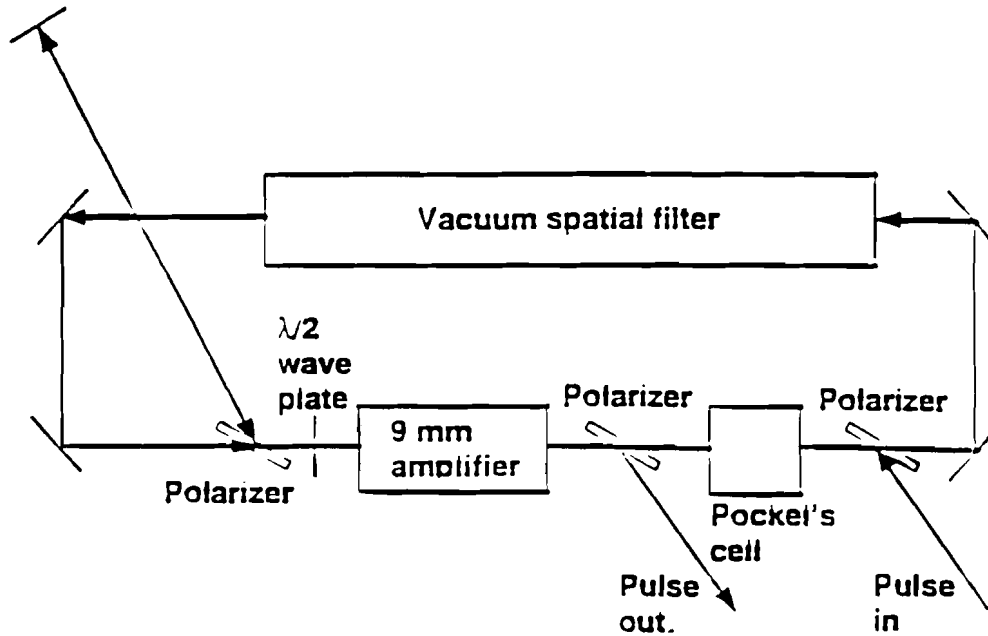


Fig. 5.3 A schematic setup of 9mm amplifier system.⁸

A schematic experimental setup for measuring the self-defocusing is shown in Fig.(5.4), it is similar to that of equivalent target plane (ETP) experiments. In order to understand why this setup can be used to measure the effect of self-defocusing, we need to understand the effect of self-defocusing. As we discussed in the Introduction, the self-defocusing is induced by ionization. The presence of the ionized electrons reduce the refractive index. Since the electron density is expected to be higher on axis than at edges, the refractive index is lower at the center of the beam. As a consequence

of this, the gas target becomes a negative lens, which causes the beam to diverge faster than it would in vacuum. Therefore the beam size will be larger than the beam size when the beam propagates in vacuum. The ionization-generated negative lens

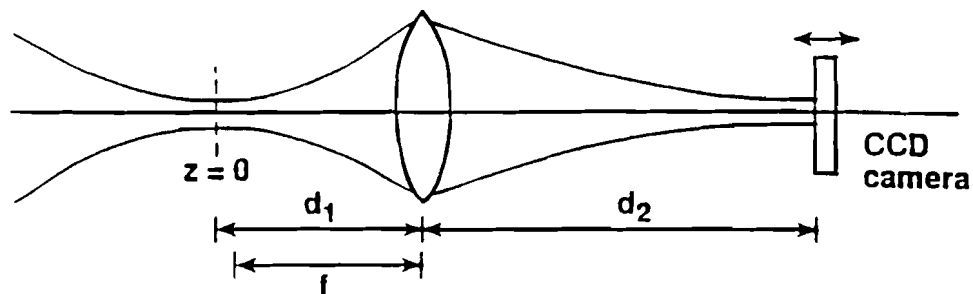


Fig. 5.4 A schematic experimental setup for measuring the self-defocusing effect.

makes the beam to be equivalent to a beam focused before the actual geometric focal point. If we use an image lens to image the focus, this virtual focus becomes a real focal point in the sense that the intensity is largest, or the beam size is the smallest. Hence, in the image space, we will find that the focus is shifted from the original geometric focal point to a new position that corresponds to the virtual focal point inside

the tank. Since the virtual focus is located at a point before the actual geometric focal point, the virtual focal spot is smaller than that if the beam propagates in vacuum. In the image plane, we will see (a) a shift of focus, (b) a smaller focal spot. These two related effects can be equally understood from the point of view of geometric optics. A more divergent beam will be focused tighter and nearer. The self-defocusing causes the image beam to 'self-focus' instead of defocus in the image plane.

Measuring the focal shifts or the magnification gives us information about the phase front distortion, or electron density profile induced by ionization. An imaging lens with a magnification of 4 is used to image the focus onto a CCD camera. A single frame of intensity distribution is captured by the CCD camera, which is connected to an IBM PC. The picture taken from the CCD camera can be stored and analyzed on the computer. By scanning the CCD camera along the direction of beam propagation, we can obtain a serial of intensity distributions at different positions. The available computer software enables us to calculate the radius (to the $1/e^2$ intensity level) assuming a Gaussian distribution. In this way, we can determine the position of the focal point and the beam divergence. Comparing the results of scans with different gas(Xenon) pressures, we can measure the focal shifts caused by the self-defocusing.

The peak intensity of a spatially and temporally Gaussian laser pulse is given very nearly by $I_0 = E / (A_{1/e} T_{fwhm})$ where E is the pulse energy, $A_{1/e}$ is the focal spot area inside the $1/e$ intensity contour, and T_{fwhm} is the full-width-at-half-maximum of the pulse duration. The relative uncertainty in the energy measurements is about 10%, and the absolute uncertainty is about 20%. The pulse duration is monitored also on each shot using an autocorrelator. For most of the experiments, the pulse duration was about 1.6ps with a fluctuation of about 25%. The focal-spot area is not measured every shot. However, when the area was measured, it was observed that it fluctuated very little from shot to shot ($\leq 4\%$). The focal area depends on the f-number of the optical

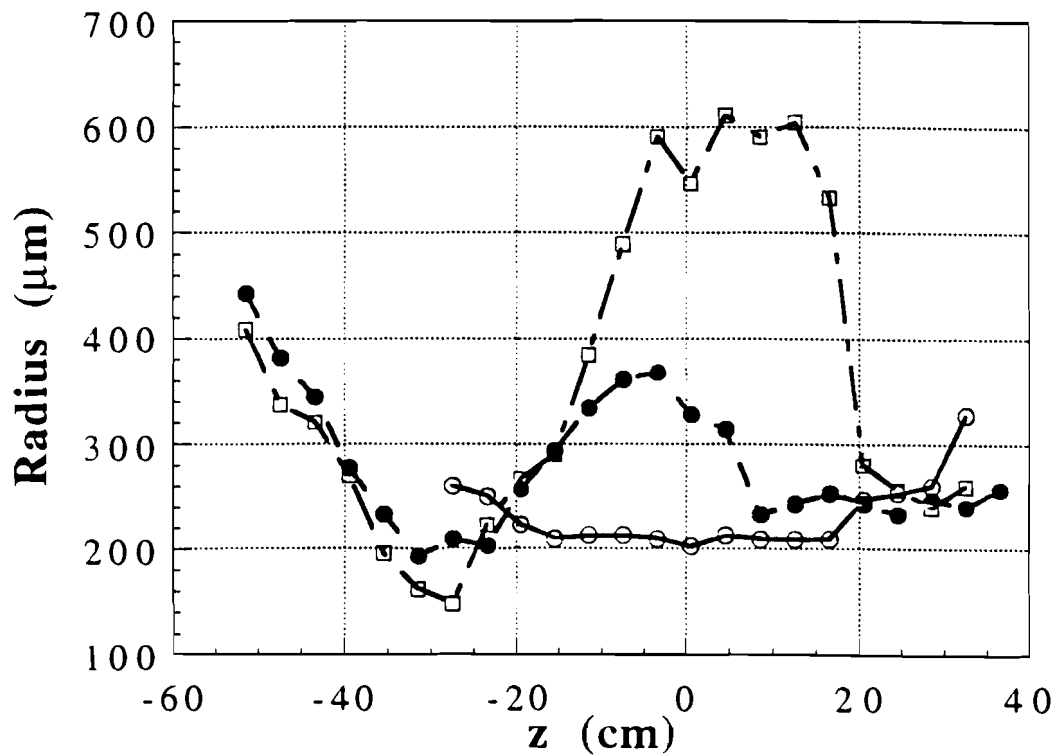


Fig. 5.5 Focal shifts at different pressure due to the effect of self-defocusing. The vertical axis represents the radius of the beam, while the horizontal axis is the relative position along the beam propagating direction. The solid curve corresponds to the case of $p = 0$ torr, the dashed curve represents $p = 2$ torr, and the dashed and dot curve corresponds to $p = 5$ torr.

system. In the experiment the f-number can be adjusted to be either 70 or 25 by changing the beam diameter. For $f/70$ system, the measured focal area for the beam used in the experiments was about $5500\mu\text{m}^2$ with an uncertainty of about 10%. The focal area for $f/25$ is measured to be $3200\mu\text{m}^2$. The $f/70$ beam is 1.2 times diffraction limited. Together, the different uncertainties give an absolute uncertainty for the laser intensity of about 35% and a relative uncertainty of about 25%.

5.3 Experimental results

In the experiment, the laser intensity was controlled to be within 10% accuracy by selecting pulses with appropriate pulse width and energy. By scanning the CCD camera along the beam propagation direction, we obtained magnified images of the focus inside the vacuum tank. Each image was stored and analyzed on an IBM PC. In the image space, one expects that the self-defocusing causes the beam size and the focal position to be different than those when there is no self-defocusing. In order to measure the changes in the focal spot and the focal position due to the effect of self-defocusing, we measured the intensity distribution as a function of the positions along the beam axis, as shown schematically in Fig. (5.4). For simplicity, the image point of the geometric focus in vacuum is denoted by $z = 0$. First, we measured the beam size ($1/e$ radius) at different positions with no gas, and obtained the image of the geometric focal point $z = 0$. Then we did the same measurements with different gas pressures. Fig. (5.5) shows the variations of beam radius as a function of position or z at pressure $p = 0, 2, \text{ and } 5$ torr. The vertical axis represents the radius of the beam in units of μm , while the horizontal axis is the distance from the geometric focal point (in image space) in units of cm. The solid curve with filled circles corresponds to the case of $p = 0$ torr, the dashed curve with squares represents $p = 2$ torr, and the dashed and dot curve with

filled triangles corresponds to $p = 5$ torr. The peak intensity in vacuum was 2.5×10^{14} W/cm², the pulse width was measured to be 1.6 ps using a single shot autocorrelator. In the experiment of Fig. (5.5), the beam size was 22mm, which gives rise to $f^\# = 70$. The thickness of the target was 2 mm, much less than the confocal parameter 12.5 mm.

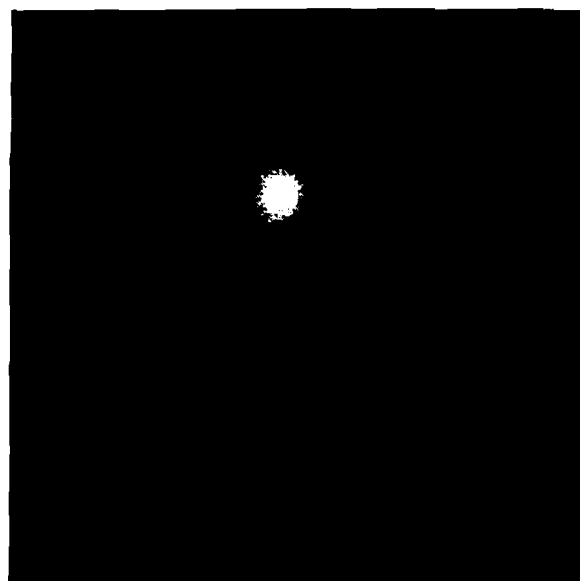
Fig. (5.5) appears to consist of two parts. At $z < 0$, the beam radius of both $p = 2$ and 5 torr are very different from that of $p = 0$ torr, while at $z > 20$, the differences in beam radius for different pressures are small. The region $0 < z < 20$ is a transitional region. At $z < 0$, both curves with $p = 2$ and 5 torr are very similar to a Gaussian beam with confocal parameters smaller than that of $p = 0$ torr. If the phase distortion generated by the effect of self-defocusing is exactly the phase distortion of a negative lens, then we will only expect to observe the region of $z < 0$. Hence this part of the data shows the characteristics of the effect of self-defocusing. It is easy to see from Fig. (5.5) that the radius for $p = 2$ and 5 torr are smaller than that of $p = 0$ torr, and the focal points are shifted to $z = -27$. The beam will continue to diverge after $z > 35$, although the experimental data is limited to $z < 35$. It is evident in Fig. (5.5) that all three beams are diverging at $z > 35$. Therefore, the defocused beams ($p = 2$ and 5 torr) have two minimum radius or beam sizes, one experiences self-defocusing and has its focal point shifted towards the lens, the other experiences virtually no self-defocusing. Since the self-defocusing results from non-uniform electron density distribution in the transverse plane, the double-foci means that there are two different electron density scale lengths. Hence, the electron density profile does not follow that of laser intensity distribution, which is well known in previous experiments.¹⁻⁵

The laser intensity distributions of $p = 0$ and 5 torr at distance $z = 36$ cm are shown in Fig. (5.6). When propagating in vacuum ($p = 0$ torr), the laser beam remains close to a Gaussian beam, no extra structure was observed, as shown in Fig. (5.6a). When $p = 5$ torr, as shown in Fig. (5.6b), a ring structure was observed. This cone

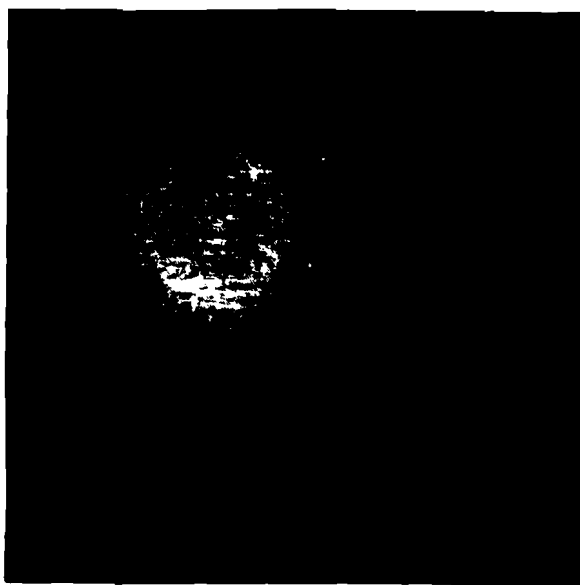
formation in Fig. (5.6b) is consistent with the double-foci in Fig. (5.5). Since the double-foci implies the existence of double scale length in the electron density distribution, and each scale length corresponds to an effective focal length, the cone formation can be understood as a result of two negative lenses with different radii. It should be mentioned that the effective focal shifts in the image space at $p = 2$ and 5 torr are very close to each other. From Fig. (5.5), we can see that the focal shifts of $P = 2$ and 5 torr are almost the same, but the beam sizes are very different from each other. In other words, the beam divergence caused by self-defocusing are different at $p = 2$ and 5 torr. It is expected that the larger the pressure, the more divergent the beam becomes. However, it is not intuitively clear why the focal shifts are saturated at a pressure as low as 2 torr.

Previous experiments and simulations showed that self-defocusing become significant at pressures much higher than 2 torr.³⁻⁷ The most important difference between our experiment and previous experiments and simulations is the focal geometry of the optical system. In our experiment, the $f/70$ system was used, while previous experiments and simulations used beams focused much tighter, typically, $f^\# < 20$. In order to confirm the effect of focal geometry on self-defocusing, we also performed the same experiment as that of Fig. (5.5), except the beam size was changed to 58mm using the Galilean up-collimator. The $f^\#$ is correspondingly changed to 25. Fig. (5.7) shows the experimental results at pressure $p = 0, 2,$ and 5 torr. No self-defocusing was observed, which is consistent with previous investigations.

Our experimental results can be summarized as follows: (a) the self-defocusing strongly depends on the focal geometry or the $f^\#$ of the focal system. (b) the self-defocusing becomes significant at a pressure as low as 2 torr for an $f/70$ system. (c) the focal shifts in the image space is saturated at pressure $p = 2$ torr. (d) the focal



(a)



(b)

Fig. 5.6 The intensity distribution of $p = 0$ and 5 torr at normalized distance $z = 1.2$ are shown. When propagating in vacuum, the laser beam remains close to a Gaussian beam, no extra structure was observed, as shown in Fig. (5.6a). When $p = 5$ torr, as shown in Fig. (5.6b), the cone formation is evident.

spots in the image space, or the divergence in real space without the presence of the image lens are very different for different pressures. (e) the double-foci, or the cone formation is related to the electron density distribution in the transverse plane. In order to understand the experimental results, we need to compare these results with theoretical predictions. The full dynamics of ionization-induced self-defocusing is a very complicated process. In the next section, we are going to develop two simplified model to explain our experimental results.

5.4 Theoretical model and computer simulations

The governing equation of self-defocusing of laser pulses can be derived from Maxwell's equations. Here we apply the formal theory of self-focusing of Shen¹² to describe the nonlinear propagation of intense laser pulses in a gas target. The electric field is described by the nonlinear wave equation

$$\nabla^2 \mathbf{E} - \frac{1}{c^2} \frac{\partial^2}{\partial t^2} \left[(n_0 + \Delta n)^2 \mathbf{E} \right] = 0 \quad (5.1)$$

where E is the electric field amplitude, c is the speed of light in vacuum, n_0 is the refractive index of gas target, Δn is the nonlinear refractive index change due to the presence of ionized electrons. Introducing a slowly-varying envelope function

$$\mathbf{E} = A(x,y,z,t) \exp[i (kz - \omega t)] \quad (5.2)$$

and making the paraxial approximation, in which the second-order derivatives of A with respect to z and t are neglected, we obtain

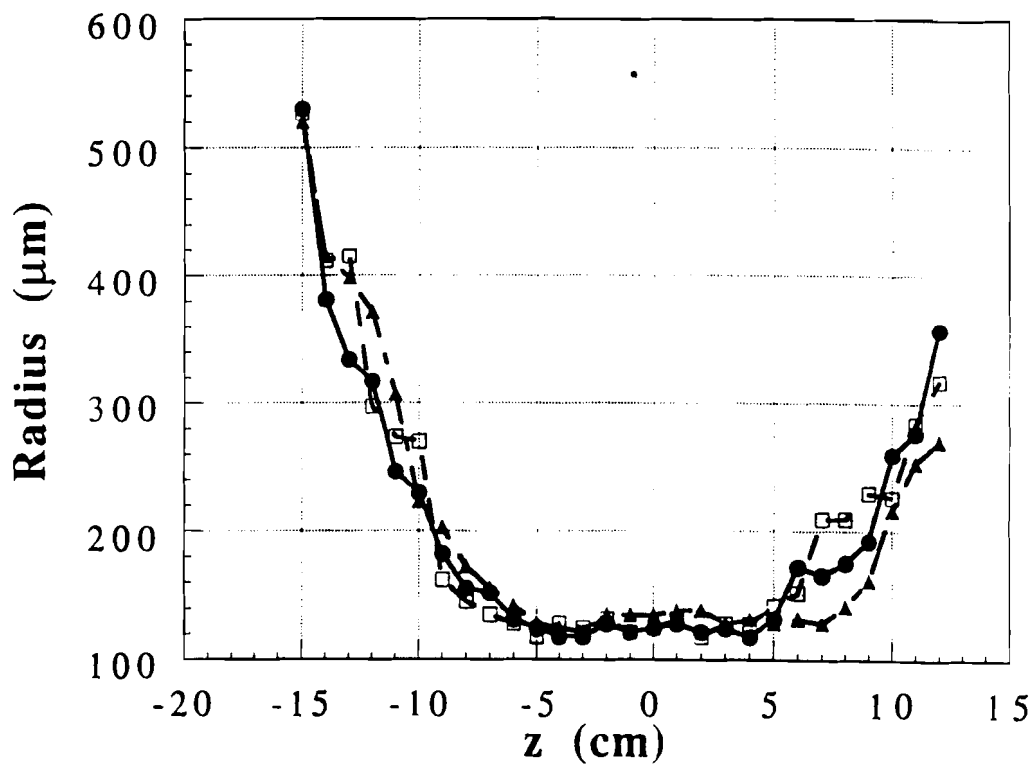


Fig. 5.7 Focal shifts at different pressure due to the effect of self-defocusing. The vertical axis represents the radius of the beam, while the horizontal axis is the relative position along the beam propagating direction. The solid curve corresponds to the case of $p = 0$ torr, the dashed curve represents $p = 2$ torr, and the dashed and dot curve corresponds to $p = 5$ torr. $f^\# = 25$.

$$i\left(\frac{\partial}{\partial z} + \frac{1}{c}\frac{\partial}{\partial t}\right)A + \frac{1}{2k}\nabla_{\perp}^2 A + k\frac{\Delta n}{n_0}A = 0 \quad (5.3)$$

where k is the wavenumber $k = n_0\omega/c$, ω is the laser frequency; z is the propagation direction, x and y are two transverse coordinates, $\nabla_{\perp}^2 = \partial^2/\partial x^2 + \partial^2/\partial y^2$ is the transverse Laplacian operator. From Drude's model,⁶ the refractive index is given by

$$n = \sqrt{1 - \frac{N_e}{N_c}} \cong 1 - \frac{1}{2}\frac{N_e}{N_c} \quad (5.4)$$

where $N_e = N_e(x, y, t)$ is the electron density, and $N_c = m\omega^2/4\pi e^2$ is the critical density. Substitution of Eq. (5.4) into Eq. (5.3) gives

$$i\left(\frac{\partial}{\partial z} + \frac{1}{c}\frac{\partial}{\partial t}\right)A + \frac{1}{2k}\nabla_{\perp}^2 A - \frac{kN_e}{2N_c}A = 0 \quad (5.5)$$

where $n_0 = 1$ has been assumed for low pressure gas medium. The time-dependent electron density $N_e(x, y, t)$ depends on the dynamics of ionization. It can be formally described by⁷

$$\frac{\partial N_e}{\partial t} = R(N_0 - N_e) \quad (5.6)$$

where N_0 is the initial density of neutral gas, R is the cycle-averaged rate of ionization. For hydrogen, the tunneling rate is given by¹³

$$R = 4\omega_0(E_0/E)^{1/2} \exp(-2E_0/3E) \quad (5.7)$$

where $E_0 = 5.14 \times 10^{11}$ V/m is the atomic unit for electric field, $\omega_0 = 4.16 \times 10^{16}$ is the atomic unit of frequency. For intensity of $I = 3 \times 10^{14}$ W/cm², $R = 4 \times 10^{14}$ s⁻¹. The atoms will be ionized in a few optical cycles. In the above derivations, the ionization loss is neglected.

Rae solved Eq. (5.3-5.7) numerically assuming a cylindrical symmetry.⁷ In his simulation, the laser wavelength is 1 μ m, laser pulse width is 1 ps. The laser beam was focused in a backfilled tank with pressure ranging from 7.5 torr to 750 torr. The peak vacuum intensity was 10^{15} W/cm². He found that there was little self-defocusing until the backing pressure was increased to 75 torr with a focusing geometry of $f/10$. He also found that the self-defocusing is more significant for larger f -number of the laser beam. It should be mentioned that the equation for electron generation (Eq. (5.6)) in Rae's simulation⁷ was incorrect. The right-hand-side of Eq. (5.6) should be $R(N_0 - N_e)$, while it was $R(N_e - N_0)$ in Rae's simulation.⁷

Although Eqs. (5.3-5.7) contain all of the physics of the nonlinear propagation of ultraintense optical pulses in gases, they are still too complicated to be helpful in understanding the self-defocusing. Here we are going to develop a simplified model based on our understanding of the physics, and have experimental investigations to check the validity of the theoretical model. According to Eq. (5.4), the higher the electron density, the smaller the refractive density. Since the electron density is expected to maximum on the beam axis, the transverse refractive index will be like a negative lens. $N_e(r)$ is a function of intensity $I(r)$, depending on the ionization model. In the situations when the thickness of the gas target is much smaller than the confocal parameter or, the Rayleigh range of the focused beam, we can ignore diffractive effects during the nonlinear propagation of short pulses in the gas. In other words, there will be no intensity variation during the propagation inside the gas target, only the phase

front of incident beam is distorted. This is just like passing through a thin negative lens. This approximation is called thin lens approximation if the electron density profile is also approximated by a parabolic profile, which will give rise to a phase front identical to the phase front generated by a thin lens. In order to gain the physical insight without complications resulting from exact ionization mechanisms, we simply assume the electron density decreases quadratically off axis. This approximation is referred to as thin lens approximation in this thesis. The ratio of the divergence angle in the cases with and without self-defocusing can be obtained from the Gaussian beam analysis, the result is as following

$$M^{-1} = \theta/\theta_0 = [1+(f_g/z_0)^2]^{1/2} \quad (5.8)$$

$$f_g = -k\rho^2 N_c / L N_p$$

where M is the magnification of the plasma negative lens, it measures the reduction of focal spot in the image plane due to the effect of the self-defocusing. f_g is the effective focal length of the plasma lens generated by ionization, N_p is the peak electron density, while ρ is the scale length of the electron density variation. L is the effective interaction distance within which most phase distortion occurs. $z_0 = 1/2 k w_0^2$ is half the Rayleigh range, k is the wavenumber of laser light in vacuum, and w_0 is the beam waist in vacuum. Therefore, the effective focal length generated by the self-defocusing can be measured by either measuring the magnification M or the shift of the focal position. The electron density $N_e(r)$ is assumed to be $N_e = N_p (1-r^2/\rho^2)$. It is easy to see that M is always smaller than 1, therefore the image spot will be always smaller when there is self-defocusing. It should be mentioned that the effective interaction distance L is approximately equal to the thickness d of the gas target if $z_0 \gg d$, while L can be approximated by z_0 if $d \gg z_0$. A simple estimate of defocusing was given by Auguste

et al,² their result is identical to ours when the second term in the bracket [(Eq.(5.8)] is much larger than 1. Our result is more general in the sense that it is valid for small self-defocusing. ρ is dependent on the ionization mechanisms, the smaller the value of ρ , the smaller the effective focal length f_g , thus the larger the divergence θ/θ_0 .

Using the same thin lens approximation as above, we can also find the relationship between the effective focal lens generated by the ionized gas target and the shifts in the focal position. It is straightforward to obtain this relationship from the theory of Gaussian beams,

$$\frac{\Delta z}{z_0} = \frac{f_g / z_0}{1 + (f_g / z_0)^2} \quad (5.9)$$

Eq. (5.9) shows the effective focal shift inside the gas target due to the self-defocusing induced by ionization. Δz is in fact the virtual focal point defined as the distance at which the beam size is smallest or the intensity is the highest. Since $f_g (= -k\rho^2 N_0 / LN_p)$ is negative, the virtual focus is located at a position nearer towards the focal lens than the original focal point without self-defocusing. The interesting thing is that Δz is different from the effective focal length f_g , which is not expected for most experiments involving optical lenses. However $\Delta z = f_g$ when $z_0 \gg f_g$. In most real experiments, the sizes of optical beams are much larger than the wavelength, so that the Rayleigh range is much larger than the focal lens used, then we have $\Delta z =$ the focal length. In the experiment here, the effective plasma lens is located at the focus, the beam size is comparable to wavelength, z_0 is of the same order of magnitude as f_g , therefore from Eq. (5.9), we can see that Δz can be very different from f_g . Secondly, it is easy to from that the maximum focal shift is $\Delta z/z_0 = 0.5$. This is similar to the following question: Given a plane Gaussian beam of size $D = 2w_0$, and a optical lens with arbitrary focal

length, what is the maximum distance one can focus the beam? The answer is that the maximum focal distance one can obtain with any lens is half the Rayleigh range of the incident beam. The consequence of this result on our experiment is that the focal shift can be saturated.

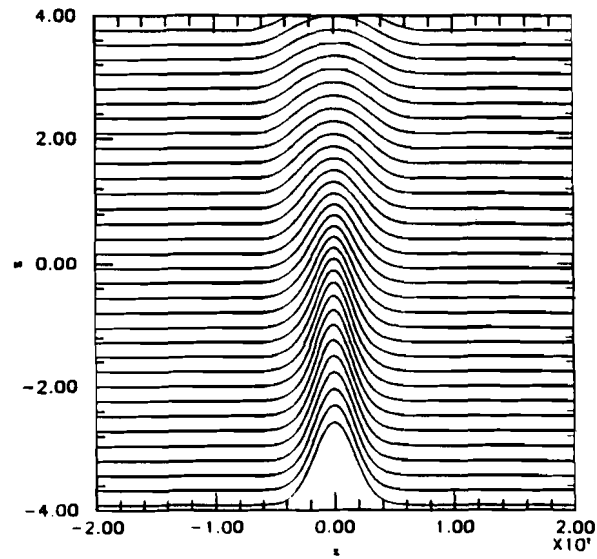
Let's assume that $f_g \gg z_0$, then the plasma lens is just like a transparent planar plate, the beam is basically unaffected by it, resulting in a null result in focal shift. On the other hand, if $f_g \ll z_0$, the divergence of the beam becomes so large that the imaginary focus approaches the original beam waist as the divergence angle becomes larger and larger. Hence, there exists a value of f_g such that the effective focal shift is the largest. Finally, Eq. (5.9) also tells us the $f^\#$ -dependence of the focal shift. For Gaussian beams, the relationship between $f^\#$ and z_0 is given by $z_0 = (8/k)(f^\#)^2$. Since $(\Delta z)_{\max} = 0.5z_0 = (2f^\#)^2/k$, the focal shift increases quadratically with $f^\#$. For example, the maximum focal shift of a $f/70$ system will be 8 times larger than that of a $f/25$ system. Aside from the purely geometric effect of the $f^\#$ -dependence discussed above, the focal shift also depends on the $f^\#$ since the value of f_g depends on both the ionization processes and the focal geometry. For small values of the $f^\#$, z_0 can be smaller than the thickness of the gas target, such that the effective interaction distance $L < d$, which results in a larger value of f_g . Hence the focal shifts can decrease faster than quadratically with decreasing $f^\#$, resulting in a even less noticeable self-defocusing. It should be kept in mind that the model is correct in the thin lens approximation. In reality, the electron density profile might be very different from a parabolic distribution. The width of the electron density distribution can be much smaller than that of the laser beam, especially when multiple ionization occurs. If this is the case, multiple focal points are possible. An improved model should take this into consideration, and hopefully provides information about the dynamics of the ionization.

We found experimentally that the focal shift of the primary focus can be

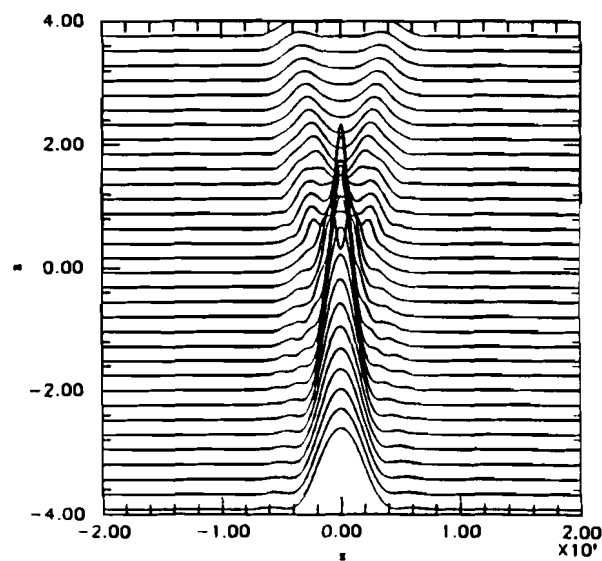
explained by the theory of thin lens approximation, while the phenomenon of cone formation and double foci are beyond of prediction of the theory. Hence, an improved model is needed to fully explain the data. We argue that the dynamics of ionization can be ignored since the majority of the laser pulse is propagating in a plasma generated by the pulse front. For instance, from Eq. (5.7), the ionization rate R is about $4 \times 10^{14} \text{ s}^{-1}$ for an intensity $I = 3.0 \times 10^{14} \text{ W/cm}^2$, wavelength $\lambda = 1.053 \text{ }\mu\text{m}$. In other words, an atom will be ionized in less than a few optical cycles. The problem of self-defocusing can be investigated in a pre-formed plasma with some specific electron density profile determined by the ionization processes. Mathematically, this means that we can separate the coupled equations Eq. (5.5) and Eq. (5.6), the information of ionization is implied in $N_e(x,y)$. By doing so, we can study the self-defocusing without complicating ourselves with detailed ionization processes. On the other hand, this assumption has solid foundations since the ionization rate R is so large that the ionization process saturates very quickly, and the majority of the laser pulse no longer participates in modifying the electron density. As a result of this assumption, we can separate the process of ionization from the self-defocusing. Unlike the thin lens approximation, Eq. (5.5) is by no means simple to solve. Here we extend the 1D split-step method used in Ch. 4 to 2D. The numerical method is given in Appendix. The code has taken into account diffraction, defocusing or refraction generated by N_e , and also the whole image system used in the experiment. First, an Gaussian beam propagates through the pre-formed plasma with given electron density profile, then the beam propagates freely from the exit of the gas target to the image lens, finally the beam is focused by this image lens, and images is obtained in the image space. A grid size of 256×256 in the transverse plane is used in all simulations. All the parameters are the same as those used in experiment if not mentioned explicitly. The program was run at CRAY-YMP at LLE.

5.4.1 Comparison of experimental results with thin lens approximation

It should be mentioned that Fig. (5.5) is obtained by fitting the intensity distribution with a Gaussian profile. The result is accurate only when the intensity distribution is close to a Gaussian profile. Since the intensity distribution is far from a Gaussian at points far away from the two foci, it is difficult to make a quantitative comparison between the experimental results and the prediction of the thin lens approximation, since a perfect Gaussian beam is assumed in the thin lens approximation. However, it is still meaningful to make a qualitative comparison. A qualitative comparison can be made for the first part. Firstly, the saturation of the focal shifts in Fig. (5.5) can be explained by the prediction of thin lens approximation (Eq. (5.9)). From the experimental data of Fig. (5.5), the focal shifts of pressure $p = 2, 5$ torr are very close to $\Delta z/z_0 = 0.6$. If we take into account of the fact that the beam is 1.2 times diffraction limited, and that the laser beam is strongly distorted after passing through the gas target, the agreement between experimental results and the prediction of thin lens approximation is very good. In fact, the experimental results are within 20% of the prediction of thin lens approximation. Secondly, according to Eq. (5.8), the magnification M decreases as the gas pressure increases, there is no saturation. The experimental results in Fig. (5.5) are consistent with Eq. (5.8). Although the focal shifts are almost the same for $p = 2$ and 5 torr, the corresponding focal spots in image plane are different from each other. It is easy to see from Fig. (5.5) that the higher the pressure, the smaller the focal spot, or the smaller the magnification M . Thirdly, as we discussed before, the thin lens approximation predicts that the focal shift decreases at least quadratically with $f^\#$. Therefore, the focal shift of $f/25$ system will be nearly 8 times smaller than that of $f/70$ system. According to Eq. (5.9), the expected focal shift $\Delta z/z_0 = 1/16$, assuming that the focal shift for $f/70$ system is at maximum. This prediction is consistent with experimental results shown in Fig. (5.7), where we did



(a)



(b)

Fig. 5.8 Fig. (5.8a) shows intensity distribution during the propagation assuming a Gaussian distribution in the electron density. Fig. (5.8b) shows the same intensity distribution, but with a super-Gaussian electron density profile. Fig. (5.8a) shows a smooth variation with a single peak distribution, while Fig. (5.8b) clearly shows that there are two peaks corresponding to a ring structure in 2D

not find noticeable self-defocusing with a focal geometry of $f/25$.

5.4.2 Comparison of experimental results with computer simulation

Although the thin lens approximation is helpful in understanding the saturation of focal shifts, the pressure-dependence of magnification, and the $f^\#$ -dependence of self-defocusing, it can not explain the double foci observed in our experiment. The thin lens approximation is based on the assumption that the electron density profile can be approximated by a parabolic distribution. However, in reality the electron density profile is closer to a super-Gaussian, or a square-top profile when laser intensity is above the ionization threshold.^{6,7} The reason is due to the saturation of ionization near the center of the beam. In other words, once all the atoms are ionized at center of beam, the electron density becomes saturated. A more realistic model should take this into account.

In order to understand the physics of the cone formation, we need to study the nonlinear refraction more accurately than the thin lens approximation. Since the laser beam is divided into two parts, refracted and not refracted, it is reasonable to relate these two parts to the transverse locations at the entrance plane of the gas target. A reasonable assumption is that the central part of beam does not experience self-defocusing, while the outside part is refracted due to self-defocusing. Since diffraction or refraction depends not only on the total nonlinear phase distortion in the transverse plane, but also the gradient of this transverse phase distortion, we argue that the gradient of phase distortion must be small at the center, and large near the edge of the beam so that the center part is unaffected, while the rest experiences strong self-defocusing. The phase distortion is proportional to electron density, the electron density should have a transverse profile similar to a super-Gaussian, which is expected when the ionization is saturated at the center of the beam.^{3,4,6,7} In order to explain the cone

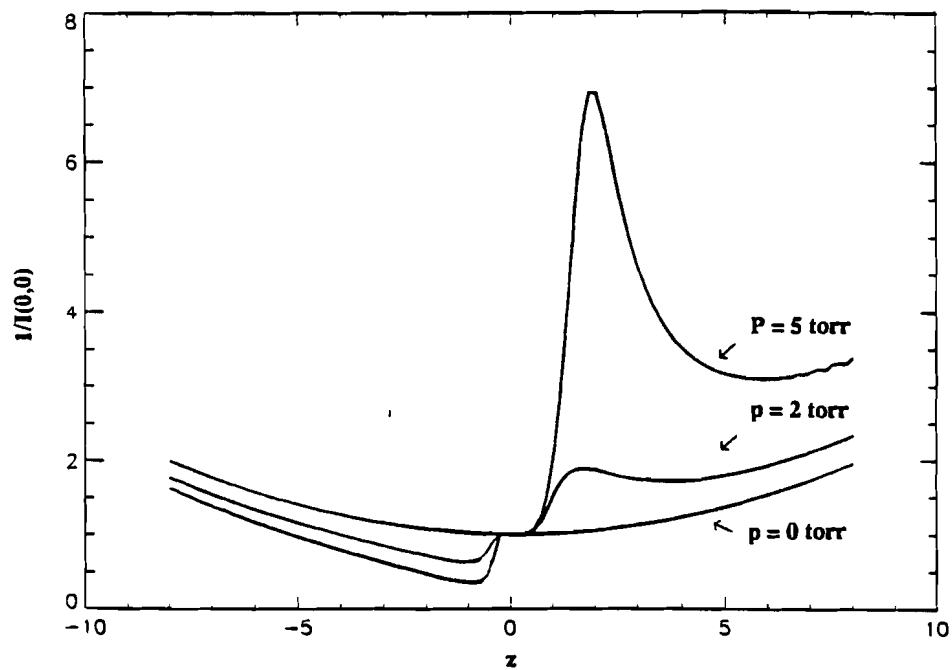


Fig. 5.9 shows the variation of $1/I(0,0)$ during the propagation in the image space, assuming that the electron density profile is a super-Gaussian. At $p = 0$, there is no effect of self-defocusing, the corresponding curve shows a smooth variation. At $p = 2, 5$ torr, we can see strong self-defocusing, as well as the existence of two foci, very similar to Fig. (5.5).

formation found in our experiment, we solve the paraxial equation (5.3) numerically assuming that the laser is propagating in the pre-formed plasma. In the simulation, we also assume that the target is much thinner than the confocal distance. The only difference between the thin lens approximation is that the transverse electron density is arbitrary instead of parabolic.

The simulation was carried out using the same physical parameters as the experiment, the pressure was assumed to be 5 torr. The electron density profile is assumed to be a super-Gaussian,

$$N_e(x,y,z=0) = N_0 \exp[-(r/\rho)^{2m}] \quad (5.12)$$

where $\rho = w_0/2$, $m = 3$. Since the laser intensity is slightly above the ionization threshold of second charge state, it is reasonable to assume that the electron density is saturated till laser intensity is half the maximum. Since the dependence of ionization rate on laser intensity is strongly nonlinear, the electron density fall off much faster than laser intensity. For Xenon, the ionization intensity thresholds is approximately 1×10^{14} , and the intensity in our experiment was 2.5×10^{14} W/cm², just above the ionization threshold of second charge state,¹⁴ therefore the edge-to-edge width of the electron density profile is approximately the laser diameter where the intensity equals to 1/e times of the peak intensity. Hence, it is a good approximation to use $\rho = w_0/2$. We assume that the ionization is dominated by the multiphoton ionization at the edges of electron density profile, then we have, $N_e \rightarrow I^m$, where m is the number of photons needed for an electron to be ionized. In our simulations, we take $m = 3$ in Eq. (5.12) as a demonstration of the effect of saturation of electron density. For pulses of duration of 1.6 ps, the ionized electrons do not have time to move, since their energies are about tens of eV. Therefore, the electron density gradient remains steep during the laser

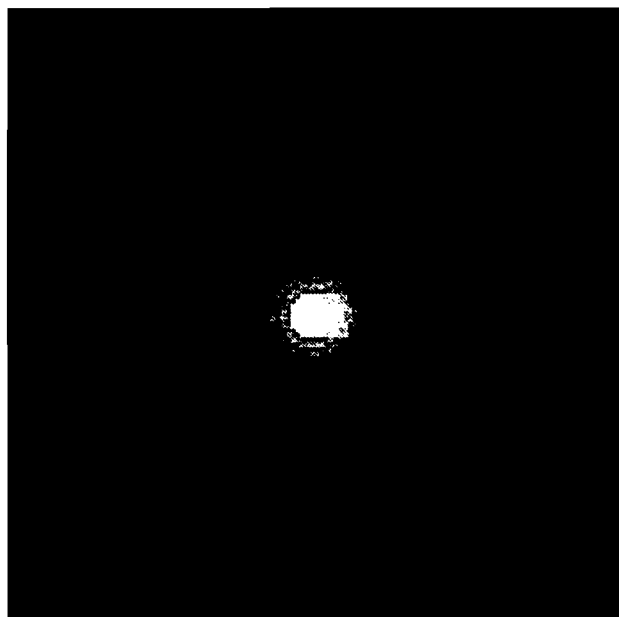
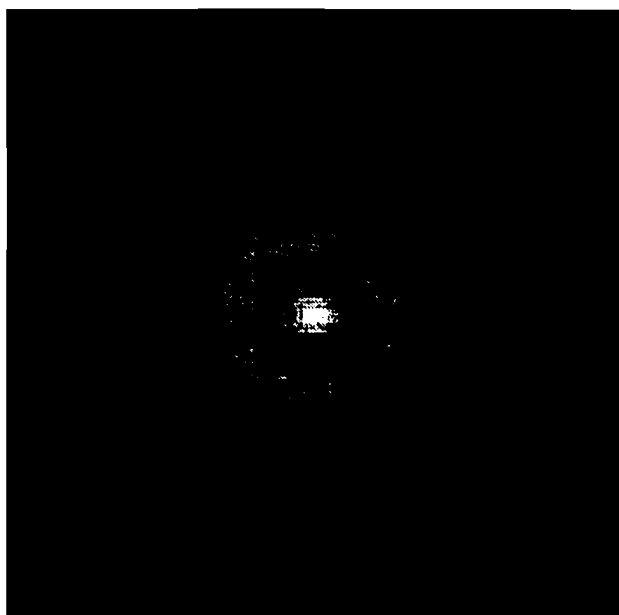
**(a)****(b)**

Fig. 5.10 Computer simulation results of intensity distribution at $z = 0.8$. (a) $p = 0$ torr; (b) $p = 5$ torr.

pulse. The actual gradient could be steeper than $m = 3$, but the refraction will be similar.

If the ionization is not saturated at the center of the beam, the electron density distribution is still Gaussian-like, the scale length is uniform across the density profile, hence the whole beam will experience self-defocusing, there will be no cone formation. In order to confirm this, we performed two simulations at the same conditions except the electron density profiles are different. The parameters used in the simulations are: $p = 5$ torr, gas target thickness $L = 2$ mm, $f^\# = 70$. Fig. (5.8a) shows intensity distribution during the propagation assuming a Gaussian distribution ($m=1$) in the electron density. Fig. (5.8b) shows the same intensity distribution, but with a super-Gaussian ($m=3$) electron density profile. Fig. (5.8a) shows a smooth variation with a single peak distribution, while Fig. (5.8b) clearly shows that there are two peaks corresponding to a ring structure in 2D. Both Fig. (5.8a,b) show that the focal points are shifted towards the lens. The simulations of Fig. (5.8) were done in 2D, we only showed the intensity distribution along x-axis for the sake of simplicity.

Fig. (5.9) shows the variation of the inverse intensity on axis, $1/I(0,0)$, during the propagation in the image space, assuming that the electron density profile is a super-Gaussian ($m=3$). At $p = 0$, there is no effect of self-defocusing, the corresponding curve shows a smooth variation. At $p = 2, 5$ torr, we can see strong self-defocusing, as well as the existence of two foci, very similar to Fig. (5.5). The result of the simulation agrees very well with that of experimental data, as can be seen by comparing Fig. (5.5) and Fig. (5.9). Both of them show the saturation of the focal shifts, both show the existence of double foci. In order to see the cone formation more clearly, we show the transverse intensity in Fig. (5.10). The cone formation can be seen from Fig. (5.10b), while Fig. (5.10a) shows smooth intensity variation. The corresponding distance is $z = 0.8$. Both computer simulation and experimental data show clearly the cone formation.

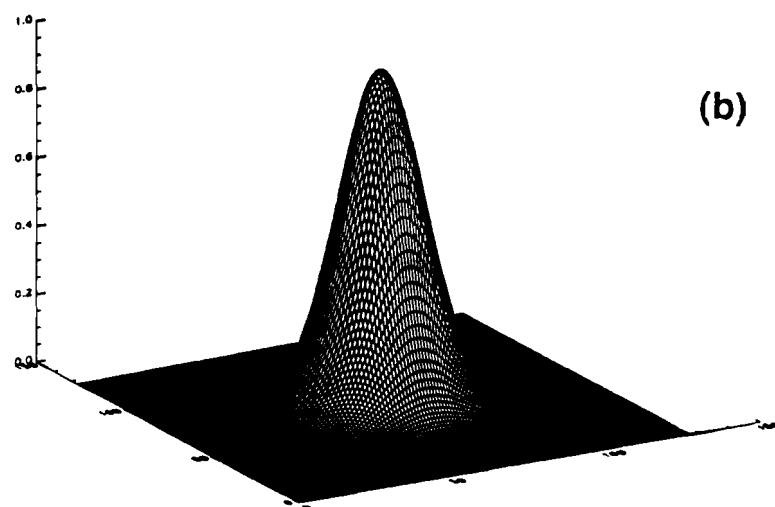
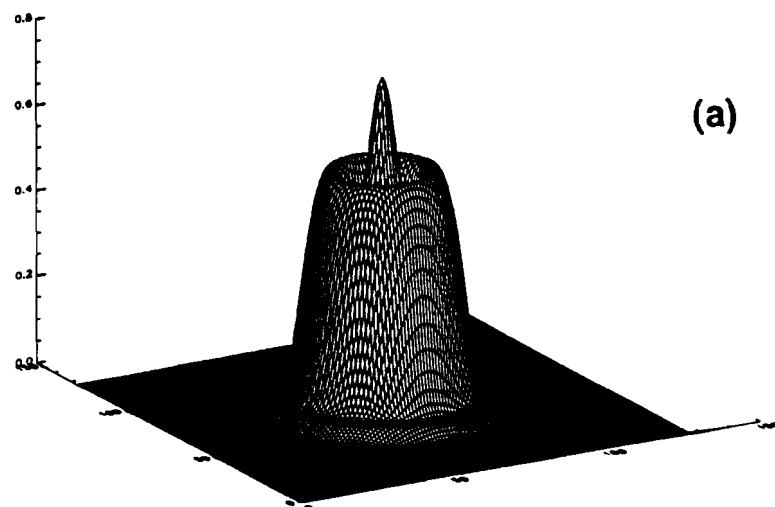


Fig. 11 3D plot of intensity distributions at different pressures. (a) $p = 5$ torr. (b) $p = 0$ torr.

The cone formation of the computer simulation in Fig. (5.10) can be seen more clearly in Fig. (5.11), in which 3D surfaces of intensity distribution are plotted. Fig. (5.11a) corresponds to the case of $p = 5$ torr, while Fig. (5.11b) corresponds to $p = 0$ torr.

According to Eq. (5.8), the self-focusing depends strongly on the focal geometry, or the $f^\#$ of the laser beam. In Fig. (5.12), we show the focal shifts of different $f^\#$ assuming $p = 5$ torr, $\rho = w_0$, $m = 1$ in the numerical simulation. The five curves correspond to $f^\# = 70, 50, 30, 10$. For $f^\# = 10$, there is little focal shift. This result was experimentally confirmed, as shown in Fig. (5.7). There were no focal shifts for both $p = 2$ and 5 torr when the $f^\#$ was 25 . In our experiment, the corresponding Rayleigh range is 1.6 mm, which is smaller than the thickness of the gas target. Since the maximum focal shift is a quarter of the Rayleigh range, the focal shift is expected much smaller than the case of $f^\# = 70$. The simulations are consistent with our experiments.

5.5 Conclusion

In conclusion, we have studied ionization-induced defocusing of laser beam in a thin gas target. It is found that the self-defocusing can be significant at a pressure as low as 2 torr. By developing a simple model (thin lens approximation), we were able to understand this experimental finding. The reason that self-defocusing can be important at such low pressure is due to the $f^\#$ -dependence of self-defocusing. The experimental results at different focal geometry, or $f^\#$ agree with the thin lens approximation. It is also found that the thin lens approximation can't explain all of the experimental data, especially the formation of ring structures in the intensity distribution. The experimental data showed that there are two foci in the image plane, which corresponds to a intensity distribution of a cone with a center spot. Based on the thin lens approximation, we developed an improved model to explain the cone

formation. The computer simulation shows that the cone formation is caused by the saturation of the electron density at the beam center. Good agreement was obtained between computer simulation and experiment.

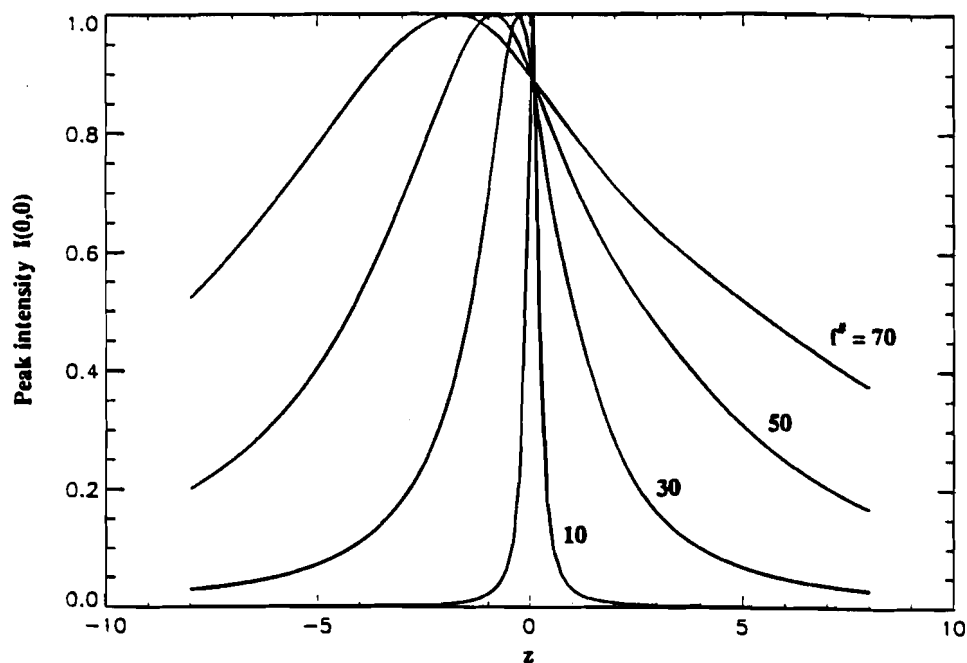


Fig. 5.12 $r^\#$ -dependence of effective focal shifts. The vertical axis is the peak intensity, the horizontal axis is the relative distance from the geometric focal point when $p = 0$ torr.

REFERENCES

1. P. Monot, T. Auguste, L. A. Lompre, G. Mainfray, and C. Mannus, *J. Opt. Soc. Am.* **B9**, 1569(1992).
2. T. Auguste, L. -A. Lompre, G. Mainfray, and C. Mannus, *Opt. Commun.* **89**, 145(1992).
3. W. L. Leemans, C. E. Clayton, W. B. Mori, K. A. Karsh, P. W. Kaw, A. Dyson, and C. Joshi, *Phys. Rev.* **A46**, 1091(1992).
4. X. Liu and D. Umstadter, *OSA Proc. on Shortwavelength V*, vol. 17, PP. 45(1993), P. B. Corkum and M. D. Perry eds.
5. T. Auguste, P. Monot, G. Maingray, and C. Mannus, *Opt. Commun.* **105**, 292(1994).
6. R. Rankin, C. E. Capjack, N. H. Burnett, and P. B. Corkum, *Opt. Lett.* **16**, 835(1991).
7. S. C. Rae, *Opt. Commun.* **97**, 25(1993).
8. J. B. Peatross, "The Far-field Angular Distribution of High-order Harmonics Produced in Light Scattering from a Thin Low-density Gas Target", Ch. 2, Ph.D Dissertation (University of Rochester, Rochester, 1993).
9. J. Peatross and D. D. Meyerhofer, *Rev. Sci. Instrum.* **64**, 3066(1993).
10. P. Maine, D. Strickland, P. Bado, M. Pessot, and G. Mourou, "Generation of Ultrahigh Peak Power Pulses by Chirped Pulse Amplification," *IEEE J. Quantum Electron.* **QE-24**, 398 (1988).
11. Y.-H. Chuang, D.D. Meyerhofer, S. Augst, H. Chen, J. Peatross, and S. Uchida, "Pedestal Suppression in a Chirped Pulse Amplification Laser," *J. Opt. Soc. Am. B* **8**, 1226-1235 (1991).
12. Y. R. Shen, "Principles of Nonlinear Optics", (Wiley, New York, 1984).
13. L. V. Keldish, "Ionization in the field of a strong electromagnetic wave," *Zh.*

Eksp. Teor. Fiz. **41**, 1945(1964).[Sov. Phys. JETP **20**,1307(1965)].

14. S. Augst, D. D. Meyerhofer, D. Strickland, and S. L. Chin, J. Opt. Soc. Am. **B8**, 858(1991).

CHAPTER 6

Summary

In this thesis, the nonlinear propagation of short optical pulses has been investigated both experimentally and theoretically. We have concentrated on two kinds of nonlinearities that have an almost instantaneous nonlinear response, that is, the optical Kerr effect and the dynamic nonlinearity in ionizing gas media. We have studied the nonlinear propagation of short pulses under the effect of the first kind of nonlinearity in Chapters 3 and 4, and the second kind nonlinearity in Chapter 5. Chapter 2 was devoted to a new method for measuring the group velocity walkoff of short pulses in birefringent media. The following results have been obtained in this thesis:

(1). In Chapter 2, we developed a new technique [frequency-domain interferometry(FDI)] for the measurement of the group velocity walkoff (GVW) of short pulses caused by polarization mode dispersion (PMD) in birefringent optical fibers, or linear birefringence in crystals. This technique (FDI) has been successfully used to measure the PMD or GVW and its advantages over other method have been discussed in detail.

(2) In Chapter 3, nonlinear birefringence in optical fibers has been investigated both experimentally and theoretically. Good agreement has been found between experiment and theory. The theoretical dependence of the nonlinear transmission on the incident polarization angle has been experimentally confirmed for the first time. It has been shown that it is possible to optimize the nonlinear transmission of devices based on the nonlinear birefringence. Applications of nonlinear birefringence in ultrafast optical pulse shaping have been discussed. A more efficient scheme of pulse shaping based on nonlinear birefringence has been proposed and analyzed. It is found that the

polarization ellipticity of incident beam can be used to optimize the efficiency of nonlinear transmission.

(3). In Chapter 4, soliton stability and soliton collisions in birefringent optical fibers have been investigated analytically and numerically. The virial theorem has been obtained for the dynamics of temporal vector solitons. The nonlinear dependence of soliton formation threshold on birefringence has been obtained for the first time. This has been confirmed by computer simulation. Collisions of vector temporal and spatial solitons have been studied numerically. It has been found that vector soliton collisions can be classified into three different regimes: (i) soliton fusion; (ii) resonant collision; (c) perturbative regime. The application of collisions of vector solitons in all-optical switching has also been discussed.

(4). In Chapter 5, the self-defocusing of 1 ps laser pulses in a thin gas target has been investigated experimentally. It has been found that self-defocusing depends strongly on the focal geometry of the optical system (or $f^\#$). It was found that the intensity profile of the laser beam was strongly modified, double foci or cone formation have been observed at a pressure of 2 torr. In order to understand our experimental findings, we have developed two theoretical models, a thin lens approximation and a numerical model. Both the saturation of effective focal shifts and the cone formation found in our experiment are in good agreement with theoretical predictions.

APPENDIX

Numerical methods

The propagation equations (4.1-2) and (5.5) are nonlinear partial differential equations. Many methods can be used to solve these equations numerically. One of the most efficient methods is the well-known split-step method (SSM).^{1,2} It has been shown that SSM can be faster than most finite-difference schemes by up to two orders of magnitude.³ The SSM has been applied to a wide variety of optical problems including wave propagation in the atmosphere,^{4,5} graded-index fibers,^{6,7} and semiconductor lasers.⁸⁻¹⁰ It is often referred to as the beam-propagation method^{6,7} when applied to the case of laser beam propagation. We have successfully used this method in many simulations such as, those involving the spatial-temporal self-focusing of chirped optical pulses,¹¹ induced self-focusing of two intersecting laser beams,¹² spatial-temporal optical turbulence,¹³ soliton beam steering,¹⁴ and collisions of vector solitons.¹⁵

Mathematically, the only difference between Eq. (4.1), (4.2) and (5.5) is the dimensionality. Here we concentrate on Eqs. (4.1) and (4.2). It is straightforward to change the program from one dimension to two dimension. Eq. (4.1), (4.2) and (5.5) can be written formally in the form¹⁶

$$\frac{\partial A}{\partial z} = (\hat{L} + \hat{N})A \quad (\text{A.1})$$

where A is the field amplitude, z is the propagation distance, \hat{L} is a linear operator that accounts for dispersion in Eq. (4.1) and (4.2), or diffraction in Eq. (5.5), and \hat{N} is a nonlinear operator that accounts for self-, and cross-phase modulations in Eq. (4.1) and

(4.2), or nonlinear refraction induced by ionization in Eq. (5.5). The explicit expressions for \hat{L} and \hat{N} are given by

(a) for Eq. (4.1) and (4.2)

$$\hat{D}_{1,2} = \mp \delta \partial_x + \frac{i}{2} \partial_{xx}^2, \quad (\text{A.2})$$

$$\hat{N}_{1,2} = i(|A_{1,2}|^2 + \epsilon |A_{2,1}|^2), \quad (\text{A.3})$$

where $A_{1,2}$ are the field amplitudes of the two waves in Eq. (4.1) and (4.2), and $\hat{L}_{1,2}$, $\hat{N}_{1,2}$ are the corresponding linear and nonlinear operators for the two waves.

(b) for Eq. (5.5)

$$\hat{L} = \frac{i}{2k} \nabla^2, \quad (\text{A.4})$$

$$\hat{N} = -i \frac{k N_e(A)}{2N_c}. \quad (\text{A.5})$$

Note that the role of z in Eq. (A.1) is not the same as the z in Eq. (5.5). It is straightforward to write Eq. (5.5) in the form of Eq. (A.1) by changing the coordinate system of z, t in Eq. (5.5) to a new one moving with the speed of light, c .

The solution of Eq. (A.1) can be formally written as

$$A(z+h) = \exp[h(\hat{L} + \hat{N})] A(z). \quad (\text{A.6})$$

where h is a small integration interval. The basic idea of SSM is to approximate the operator $\exp[h(\hat{L} + \hat{N})]$ by $\exp[h\hat{L}]\exp[h\hat{N}]$, or in other words, to obtain an approximate solution by assuming that in propagating the optical field over a small

distance h , the dispersive and nonlinear effects can be treated independently. What the linear propagation (diffraction or dispersion) does is to convert the phase distortion to amplitude distortion, while nonlinear propagation converts amplitude distortion to phase distortion. The SSM divides a propagation step h into two substeps: first the field is propagated linearly with the nonlinear effect frozen, then the field is propagated nonlinearly with linear effect frozen. Mathematically,

$$A(z+h) = \exp[h \hat{L}] \exp[h \hat{N}] A(z). \quad (\text{A.7})$$

Up to this point, there is little improvement or advantage compared to other methods. The heart of SSM is the calculation of the linear propagation using the fast-Fourier transform (FFT) technique. In spectral space, the linear operator $\hat{L}(\omega)$ becomes an algebraic multiplier since $\hat{L}(\omega)$ is obtained by replacing $\partial/\partial x$ by $i\omega$, where ω is the frequency in the Fourier domain. For example, $\hat{L}(\omega) = i\omega\delta - i\omega^2$. Therefore, in the spectral domain, the linear propagation can be calculated simply by multiplying each frequency component $A(z,\omega)$ by a factor of $\exp[h \hat{L}(\omega)]$, or mathematically,

$$A(z+h,\omega) = \exp[h \hat{L}(\omega)] A(z,\omega) \quad (\text{A.8})$$

The pulse shape $A(z,t)$ can be obtained by taking an inverse Fourier transform of $A(z,\omega)$. Since the nonlinear operator is already a simple multiplier in physical space, the nonlinear propagation is performed in physical space. The splitting of Eq. (A.7) is accurate to the second order in the integration step h ; the accuracy can be improved by using better splitting schemes. In our simulations, we used a scheme known as the symmetrized SSM,⁴ which is accurate to the third order in h . Mathematically, it can be written as

$$A(z+h) = \exp\left[\frac{h}{2}\hat{L}\right]\exp\left\{\frac{h}{2}[\hat{N}(z) + \hat{N}(z+h)]\right\}\exp\left[\frac{h}{2}\hat{L}\right]A(z) \quad (\text{A.9})$$

Physically, Eq. (A.9) can be expressed as following: The field $A(z)$ is propagated linearly for a distance of $h/2$. At the midplane $z+h/2$, the field is propagated nonlinearly for the whole length h , and then the field is linearly propagated for a distance of $h/2$ again. This scheme is called the symmetrized SSM because the nonlinear propagation begins at $z+h/2$, while linear propagation begins at z and $z+h$, located symmetrically around the nonlinear propagation.

The implementation of Eq. (A.9) is straightforward. It should be mentioned that there are several things that need to be kept in mind when testing and running the numerical code. The simulation box should be large enough to ensure the periodic boundary conditions required by the FFT, otherwise high frequency noise will cause numerical instability. For bandwidth-limited pulses, it is important to have enough grid points to ensure that all frequency components are sampled accurately, and the spectral resolution is good enough for the practical applications. It is well known that the nonlinear Schrodinger equation (NSE) supports the so-called modulational instability (MI).¹⁶ If the spectrum of numerical noise is located inside the bandwidth of MI, the noise will be amplified, resulting in numerical instability. Usually, this numerical instability can be avoided if the relationship $h < T^2/\pi N^2$ is satisfied, where T is the length of simulation box, and N is the number of grid points.¹⁷

References

1. R. H. Hardin and F. D. Tappert, *SIAM Rev. Chronicle* **15**, 423 (1973).
2. R. A. Fisher and W. K. Bischel, *Apply. Phys. Lett.* **23**, 661(1973).
3. T. R. Taha and M. J. Ablowitz, *J. Comp. Phys.* **55**, 203 (1984).
4. J. A. Fleck, J. R. Morris, and M. D. Feit, *Appl. Phys.* **10**, 129 (1976).
5. M. Lax, J. H. Batteh, and G. P. Agrawal, *J. Appl. Phys.* **52**, 109 (1981).
6. M. D. Feit and J. A. Fleck, *Appl. Opt.* **17**, 3990 (1978).
7. M. D. Feit and J. A. Fleck, *Appl. Opt.* **18**, 2843 (1979).
8. G. P. Agrawal, *J. Appl. Phys.* **56**, 3100 (1984).
9. P. Meissner, E. Patzak, and D. Yevick, *IEEE J. Quantum Electron.* **QE-20**, 899(1984).
10. G. P. Agrawal, *J. Lightwave Technol.* **LT-2**, 537 (1984).
11. X. D. Cao, G. P. Agrawal and C. J. McKinstrie, "Self-focusing of chirped optical pulses in nonlinear dispersive media," *Phy. Rev.* **A49**, 1085 (1994).
12. X. D. Cao, C. J. McKinstrie, and D. A. Russell "Novel aspects of the nonlinear focusing of light waves," 33rd Annual Meeting of the American Physical Society Division of Plasma Physics, Tampa, Florida, Nov. 4-8, 1991.
13. L. W. Liou, X. D. Cao, C. J. McKinstrie, and G. P. Agrawal "Spatial-temporal instabilities in dispersive nonlinear media," *Phys. Rev.* **A46**, 4202 (1992).
14. X. D. Cao, G. P. Agrawal, and D. D. Meyerhofer, "Optimization of optical beam steering in nonlinear Kerr media via spatial phase modulation", to be published in *J. Opt. Soc. Am.* **B11**.
15. X. D. Cao and D. D. Meyerhofer, "All-optical switching via collisions of spatial vector solitons", to be published in *Opt. Lett.* "Soliton collisions in optical birefringent fibers," *J. Opt. Soc. Am.* **B10**, 380 (1994).

16. G. P. Agrawal, *Nonlinear fiber optics* (Academic Press, New York, 1989).
17. J. A. C. Weideman and B. M. Herbst, *SIAM J. Numer. Anal.* **23**,485 (1986).